Deformation Mechanisms in Nanoscale Brittle Materials

A DISSERTATION
SUBMITTED TO THE FACULTY OF THE GRADUATE SCHOOL
OF THE UNIVERSITY OF MINNESOTA
BY

Douglas Dean Stauffer

IN PARTIAL FULFILLMENT OF THE REQUIREMENTS
FOR THE DEGREE OF
DOCTOR OF PHILOSOPHY

William W. Gerberich

May, 2011

© Douglas D. Stauffer, 2011

Acknowledgements

There have been scores of people who have assisted, collaborated, and instructed me during my time in graduate school. First off, I need to acknowlege Professor Gerberich for his guidance, perseverance, and insight. Working with fellow Gerberich group members, Bill Mook, Megan Cordill, Lucas Hale, and Aaron Beaber helped set the foundation for this work. The *in situ* conductance work would not have been possible without films grown by Prof. Leighton and his group; Jeff Parker, Mike Manno, and Palak Ambwani. These experiments were performed at Hysitron, Inc. with assistance of the David Vodnick, Richard Nay, and Todd Stanley, in collaboration with Ryan Major. In the UMN Characterization facility, training was provided by Robert Hafner and Greg Haugstad, and collaborations with Ozan Ugurlu and John Thomas III. *In situ* TEM work was in collaboration with Ozan Ugurlu, Professor Mkhoyan, and his group, especially Andrew Wagner. In addition I would like to thank Eric Stach for considerable assistance on imaging and analyzing dislocations in the TEM.

Lest I forget, the team in Amundson 151, who made sure that all the t's were crossed, i's dotted, and that paychecks came in on time.

In addition to the people have helped along the way, I would like to acknowledge that I received funding from Hysitron, Inc., the Abu Dhabi-Minnesota Institute for Research Excellence a partnership with the Petroleum Institute, NSF/DMR-0946337, and the Air Force Office of Scientific Research AOARD-08-4134. The authors would also like to thank Palak Ambwani for additional characterization of the Al thin films. Parts of this work were carried out in the Institute of Technology Characterization Facility, University of Minnesota, a member of the NSF-funded Materials Research Facilities Network.

Dedication

I dedicate this thesis to my wife, Cynthia, our son
Adrian, who asks what I want to be when I grow up,
and my Mom, Dad, and Sister, who showed me
hard work can make all the difference.

Abstract

In the past ten years nanotechnology has developed from a buzzword to an integral part of our modern life. The promise of bottom up devices has turned into better, faster, and stronger products utilizing nanoscale materials. Tires designed with carbon nanotubes, touchscreens, reformulated steel, self-cleaning fabrics, drug delivery systems, and semiconductor devices all rely on nanoscale materials. However, the mechanical property relationships are not fully understood, and the cross-roads of mechanical performance and electrical properties is still being explored. For example, the role of electrical contact in mechanical systems is important for reliability in systems that contain interconnect, switches, or relays. MEMS switches in particular can have reliability issues if the conducting area is decreased, or the switch fails due to plasticity. In this thesis, an attempt is made to characterize failure modes of several fundamental nanoscale materials using nanoindentation.

In this thesis, ostensibly brittle materials such as alumina, chromia, and silicon are chosen as being archetypal examples of brittle materials. The use of conductive probe indentation is used here as a measure of plasticity under the indenter in constrained metal films with native oxide layers, as well as to determine the point of oxide fracture. *In situ* transmission electron microscope indentation is used to explore dislocation velocities and strain hardening in compressed silicon pillars. Dislocation velocities, in compression at room temperature, are found that approach that of those at 600°C in bulk tensile specimens. The dislocations, of unknown type, also contribute to strain hardening exponents of approximately 0.4 in pillars, and approach unity in silicon spheres.

Table of Contents

Acknowledgments i

Dedication ii

Abstract iii

Table of Contents iv

List of Tables viii

List of Figures ix

Chapter 1. Introduction and motivation 1

1.1. Motivation 2

1.2. Overview 2

1.3. Material choices, a reduction in dimension 3

1.4. Indentation and contact mechanics 4

1.4.1. Relating hardness to yield strength 4

1.4.2. Indentation hardness 4

1.4.3. Ideal contacts 6

1.4.4. Elasticity simulations 9

1.4.5. Contact: A transition from elastic to elastic-plastic, and fully plastic 10

1.4.6. Analysis for non-ideal geometries 14

1.5. Electrical contacts 16

1.6. Indentation equipment 18

Chapter 2. Plastic response of thin film systems 24

2.1. Overview 25

2.2. A platinum reference sample 26

2.2.1 Relating conductance to contact area 26

2.2.2 Surface roughness effects 30

2.2.3 Tunneling 34

2.2.4 Indentation with carbide tips 36

2.3 Initial films of chromium and aluminum 38
2.3.1 Experimental considerations and structural characterization 38
2.3.2 Damage mechanisms within chromium and aluminum thin films 42
2.3.3 Elastic simulations of chromium and aluminum thin films 50
2.3.4 Radial stresses 54
2.4 Plastically constrained aluminum films 55
2.4.1 Experimental considerations 55
2.4.2 Effects of plastic constraint on fracture in Al thin film system 58
2.5 Summary 61

Chapter 3 – *In situ* Transmission Electron Microscopy Indentation 62
3.1 Introduction to *in situ* TEM indentation 63
3.2 Historical background 64
3.3 Sample constraints 64
3.4 Instrument constraints 68
3.5 Microscope / Indenter operation 69
3.6 Analysis 71
3.7 Advantages over conventional indentation 72
3.8 Summary 74

Chapter 4 – Plastic response of low-dimensional systems: Silicon 75
4.1 Introduction: Dislocation dynamics in high temperature silicon 76
4.1.1 Defining dislocations in silicon 79
4.2 A ductile to brittle size transition? 81
4.3 Silicon nanopillars 82
4.4 Compression of silicon nanopillars 84
4.4.1 Young's modulus for both sets of pillars 86
4.4.2 Bending in pillars 88
4.5 Dislocation velocities, part I 89

4.6 Dislocation imaging 97
4.6.1 Dislocation imaging: Burgers vector identification 102
4.6.2 High-resolution imaging 103
4.7 Dislocation velocities, part II 105
4.8 Summary 108

Chapter 5. Strain-hardening in sub-micrometer silicon systems 109
5.1 Introduction 110
5.2 Experimental procedures 112
5.2.1 Contact approximations 114
5.2.1.1 Right cylinder approximation 114
5.2.1.2 Harmonic mean approximation 116
5.2.2 True stress-true strain 117
5.3 Results on silicon spheres 118
5.4 Results on silicon pillars 121
5.5 Strain-hardening model 124
5.6 Discussion of the results using the proposed model 130
5.7 Phase transformations in silicon 136
5.8 Summary 130

Chapter 6. Future directions 140
6.1. Introduction 141
6.2 Further exploration of fracture in aluminum thin films 141
6.2.1 Grain size effects 141
6.2.2 Elastic constraint 142
6.2.3 Characterizing fracture *ex situ* 142
6.3 Electrical contact for film delamination 145
6.4 Deformation in iron oxides by conductive indentation 147
6.5 Determination of dislocation identity in compressed silicon 148

6.6 Application to geological materials 149
6.7 Combining the two *in situ* techniques 150
6.8 Summary 154

References **155**

List of Tables

Table 1.1. Geometric factors for common tips. Adapted from Fischer-Cripps and Oliver, et al. 15

Table 5.1. Strain hardening exponents for multiply loaded Si spheres. 119

Table 5.2. Strain hardening exponents for singly compressed spheres. 120

Table 5.3. Strain hardening exponents for both VLS and FIB machined silicon pillars. 124

List of Figures

1.1. Contact of (a) spherical indenter and (b) sharp conical indenter for an isotropic half-space. 7

1.2. Comparison of simulations for normal (a) and shear (b) stress. 11

1.3. Plot of von Mises shear stress in same conditions as figure 1.2. 12

1.4. Idealized loading curve for indentation. 14

1.5. Noise floor of the Hysitron TriboIndenter 19

1.6. Schematic of three plate transducer system, as used in the TriboIndenter. 20

1.7. Schematic of two terminal contact resistance measurement, as implemented. 22

2.1. Current – voltage (I-V) sweeps at increasing displacement in (100) single crystal Pt. 27

2.2. Conductance calculated from (a) linear fits to the I-V sweeps of figure . 2.1, (b) current measured at a constant applied bias during loading. 28

2.3. Maxwell theoretical conductance for the system in Pt. 29

2.4. Projected area and surface area of a spherical indenter. 30

2.5. Roughness of 1-D grooves in Cu after indentation. 31

2.6. Fit of the derivative of I-V for Pt using the Brinkman-Dynes-Rowell criteria. 35

2.7. Load – depth (a) for sharp carbide Berkovich tip. I-V sweeps (b) for the same indent. 36

2.8. Conductance – depth relationship for carbide tip. 37

2.9. Grazing incidence (a) Wide angle x-ray diffraction (a inset) and in-plane x-ray diffraction for 28 nm Cr film confirm growth orientation and thickness. 38

2.10. Density profile of the Cr film system using fit from figure 2.9(a). 39

2.11. Depth profiling from x-ray photoemission spectroscopy (XPS) 41

2.12. Displacement controlled indent on Al film system 43

2.13. Load controlled indentation with large displacement on Al system 44

2.14. Oxide fracture for Ni (a) from Pethica, and for Al (b) in this study. 45

2.15. I-V sweeps taken at 20 nm displacement in the Al film system. 46

2.16. Conductance – depth and Load – depth relations for Cr film system. 47

2.17. Conductive scanning on the Cr film system . 48

2.18. Simulation of the von Mises stress in the Cr system. 51

2.19. Simulation of the von Mises stress in the Al system. 52

2.20. Simulation of the von Mises stress for a rough Al system. 53

2.21. Scanning probe microscopy of Al films with plastically constrained substrate. 56

2.22. Conductance – time for three consecutive indents with the carbide tip. 57

2.23. Increasing loads for 43 nm film failure. 59

2.24. Statistics for the depth of oxide failure for Al films of 6 thicknesses. 60

3.1. Schematic of pillar being compressed *in situ*. 63

3.2. Image of tripod polished single crystal olivine sample 66
(a) half-ring sample holder, (b) the sample mount.

3.3. SEM micrographs of (a) silicon wedge plateau for sample deposition, 67
(b) higher magnification of the same wedge plateau. The schematic
(c) of using a wedge shaped specimen to avoid sample shadowing,
(d) SEM micrograph using the wedge for *in situ* deformation of Si pillars.

3.4. Photograph of the Hysitron PicoIndenter, with parts labeled. 69

3.5. *In situ* video capture of tip and sample aligned in the microscope z-direction. 70

3.6. *In situ* video capture of pillar in bending. 72

3.7. Load – displacement of initial contact of *in situ* indentation on Al film. 74

4.1. Peierl's energy barrier. 77

4.2. Dislocation velocities as a function of temperature and applied shear stress. 78

4.3. Ductile to brittle temperature transition for bulk silicon. 79

4.4. Dislocations in the diamond cubic structure. 80

4.5. Bright field TEM micrograph of typical EBE deposited Si pillar. 83

4.6. Bright field TEM micrograph of typical CVD deposited Si pillar. 83

4.7. *In situ* compression (a) load - time (b) load – depth 85
(c) Precompression, and (d) post compression of a 200 nm EBE pillar.

4.8. Three consecutive compression on the 200 nm pillar for modulus. 87

4.9. Diffraction bands moving during the compression of a 89
265 nm diameter EBE pillar over time.

4.10. Lüders bands in (a) polycrystalline aluminum, and (b) schematic of 91
Lüders band dislocation propagation in a single crystal .

4.11. CVD pillar in two beam condition (a) prior to compression with 93

(b) diffraction pattern.
4.12. Schematic of elastic bending with interference pattern in the intensity profile. 93
4.13. Simulated intensity profile for a screw dislocation. 94
4.14. First 0.8 s of compression for a previously damaged CVD pillar. 95
4.15. Diffraction bands from bending in *in situ* video capture. 96
4.16. Movement of diffraction bands towards the indenter during the unloading. 97
4.17. Pre and post compression micrographs of a 120 nm diameter CVD pillar, singly compressed, to 4 GPa, 99
4.18. Pillar from 4.17, after removal half-grid from sample mount and insertion in a double tilt holder, 200keV microscope. 100
4.19. Dark field image of 120 nm pillar of figure 4.17, showing dislocation contrast. 101
4.20. Dark field image of kink in the pillar (figure 4.17). 101
4.21. Dark field image, “near” invisibility criteria. 103
4.22. High resolution TEM of the damaged region. 104
4.23. Method for determination of dislocation velocities. 105
4.24. Comparison of dislocation velocities for Imai at 600°C and room temperature measurements of this study. 107
5.1. Pre (a) and post (b) work hardened silicon pillar, and pre (c) and post (d) work hardened sphere. 111
5.2. Load – depth for repeat loading of a 43.6 nm sphere. 113
5.3. Schematic of right cylinder approximation for compression of spheres. 115
5.4. Schematic of harmonic mean approximation. 116
5.5. True stress – true strain for two spheres under multiple compressions. 118
5.6. True stress – true strain for the first compression for spheres of varying diameter. 120
5.7. True stress – true strain for *in situ* singly compressed spheres. 121
5.8. True stress – true strain for a repeatedly compressed CVD pillar. 122
5.9. True stress – true strain for both VLS grown and FIB machined pillars. 123
5.10. True stress – true strain for MgO pillars. 129
5.11. Strain hardening exponent as a function of pillar dimension and applied strain. 130
5.12. Strain hardening exponents as a function of sphere diameter. 131
5.13. Comparison of strain hardening in load control and displacement control. 132
5.14. Idealized schematic of plasticity in compressed spheres and pillars. 135

5.15. Evidence of reverse phase transformation in a singly compressed Si sphere. 137

6.1. Kelvin force microscopy (a) height and 143

(b) potential difference with respect to the Pt tip on cracked Cr films

6.2. High resolution KFM of area across the crack. 144

6.3. Schematic of single (a) and double (b) buckling in thin films. 145

6.4. Displacement and constant bias current for Cu films, 147

which delaminate on unloading.

6.5. Single crystal olivine indented with a cube corner causes radial cracking, 150

(a) video enhanced light microscopy, and

(b) TEM micrograph of a near crack FIB liftout.

6.6. Micrograph of doped Si pillar prior to *in situ* conductive indentation. 151

6.7. Combining *in situ* TEM and electrical contact measurements for Load a110 nm 153

diameter pillar (a) Load, conductance, and

(b) I-V sweep taken during the hold period

Chapter 1. Motivation and Introduction to Contact Mechanics

1.1. Motivation

In the past ten years nanotechnology has developed from a buzzword to an integral part of our modern life. Fifty years after Feynman's promise of bottom up devices in 1959, better, faster, stronger products utilizing nanoscale materials have been realized. Tires designed with carbon nanotubes, touchscreens, reformulated steel, self-cleaning fabrics, drug delivery systems, and the further miniaturization in semiconductor devices all rely on nanoscale materials. However, the changes in mechanical and electrical behavior the qualities desired in these materials have yet to be adequately described. For example, the role of electrical contact in mechanical systems is important for reliability in systems that contain interconnect, switches, or relays. MEMS switches in particular can have reliability issues if the conducting area is decreased, or the switch fails due to plasticity. Repeated stress, friction and wear, and strain hardening capacity are all very important. However, the difficulty in performing and interpreting these experiments has thus far led to an incomplete evaluation. In this manuscript, an attempt is made to characterize failure modes of several fundamental nanoscale materials.

1.2. Overview

Indentation has become one of the widely used methods for measuring the mechanical properties of low-dimensional materials. In the first chapter, the fundamental principles of mechanical and electrical contacts will be discussed. These fundamentals will then be applied to solve problems in chapters 2 (failure of thin metal films with native oxides) and 4 (silicon nanopillars). The small size of the silicon nanopillars requires the use of *in situ* indentation testing with a transmission electron microscope. The requirements, benefits, and operation of such an instrument are the topics of chapter 3. Using the material from chapters 1, 3, and 4, the demonstration of work hardening in silicon is demonstrated, and strain hardening exponents as a function of feature size is shown. This work could then be applied to other materials, including iron oxides and olivine, in chapter 6 where the two primary *in situ* indentation techniques, electrical

contact and TEM, are combined. An additional variable, temperature, may be also be added.

1.3. Material choices

The first two materials of interest are thin films of aluminum and chromium. Both of these metals have native oxides which are "self-limiting". This results in an oxide layer about 1 to 2 nm in depth prior to becoming diffusion limited.[1, 2] The first oxide, alumina scale, is a commonly used dielectric material, pinhole-free tunnel barrier, and anti-corrosion layer, has a high Young's modulus, and has been well characterized by the community. [3, 4] The second oxide, chromia, is also a high modulus anticorrosive layer, but has very different electrical characteristics, and is not widely employed as a tunnel barrier due to propensity for pinholes.[5, 6] These two films then can be used to show two types of electrical contact behavior. Due to these differences, Al films are then chosen to be examined as a function of metal layer thickness, in this case for oxide fracture.

Silicon was chosen for its ease of manufacturability, and its extensive use in the semiconductor industry. Two collaborations developed for the vapor-liquid-solid growth of (111) oriented silicon pillars. Silicon is a classic "brittle" material, which in addition to a brittle to ductile transition with increasing temperature has recently been shown to have a brittle to ductile length scale transition. The nucleation of dislocations of an unknown type in these silicon pillars is verified, which leads to the first measurements of dislocation velocities in silicon nanopillars. While Si has a native oxide, it is considered only briefly, in the role the oxide layer plays in trapping mobile dislocations in relation to the work hardening demonstrated in chapter 5.

In all cases, the length scales of interest are small. The metal films range from 10 to 300 nm, while the native oxide layers are typically only 2 nm in thickness. The silicon nanopillars range from 100 nm in diameter to 300 nm in diameter. It is the mechanical properties at these reduced length scales that motivates this work.

1.4. Indentation and Contact Mechanics

1.4.1. Hardness in relation to yield strength

Typically, stress-strain curves are taken by tensile testing. Alternatives to tensile testing include three-point bend and compact tension; however all of these methods require specified sample geometry and are destructive tests. Alternative methods were required to test unique sample geometries at the expense of complications in the stress field. When a material yields in a uniaxial tensile test, the three principle stresses p_1, p_2, and p_3, simplify to $p_2 = p_3 = 0$ and $p_1 = Y$, where Y is the yield strength. Indentation experiments put the material under both compressive and shear stresses during indentation testing, increasing the likelihood of flow. The hardness of a material is related by the constraint factor, C, to its strength, as in Eq. 1.1.[7] The constraint factor can be approximated at 3 for metals (with high values of E/Y) and 1.5 for materials with a low E/Y ratio.

$$H \approx CY \qquad \text{Eq. 1.1}$$

1.4.2. Indentation Hardness

Indentation testing has provided a reasonably easy way to measure hardness by using a well-characterized tip of known shape to press into the sample. These instruments are typically cheaper than the corresponding tensile testing apparatus and give fast and reliable results. A progression of the Mohs hardness scale, indentation hardness was originally defined as the pressure required to initiate plasticity, but historically this has been difficult to measure. The American Society of Testing and Materials defines hardness as "the ability of a material to resist permanent indentation or deformation when in contact with an indenter under load."[8] Mohs and other hardness scales have a strong connection to wear properties, fracture toughness, yield strength, and shear modulus.[9, 10] Hardness, H, as a measurable quantity, can be defined as

$$H = \frac{P}{A},$$ Eq. 1.2

where P is the applied load and A is the contact area. It is important to make the distinction between the *actual* contact area, used in early indentation testing, while modern instrumentated indentation testing uses the *projected* contact area.

There are several hardness theories, some of which involve a sharp indenter effectively "cutting" the material and forcing it to the surface. In these cases the constraint factor, C, would be determined by plastic flow and velocity using either the Tresca or von Mises yield criterion in metallic systems.[11, 12] Another proposed theory is the "expanding cavity model", introduced by Johnson, where the core region is surrounding by a plastic cavity, which is in turn surrounded by an elastic continuum.[13] This will be discussed later in this chapter, under elastic-plastic loading. For now, the concern will be the residual plastic effects, independent of elasticity.

The major limitation of the spherical indenter in measuring hardness is pile-up at the edges of the indentation surface, giving rise to errors in the measuring the residual impression. This led to advancements in tip technology, including the development of the four-sided Vickers diamond pyramid. The angle of 136° between faces mimics the stress-strain relationship of the spherical indenter.

Vickers indentation bridges the gap between macro- (1 kgf minimum load [14]) and microindentation. The ease of measurement of the diagonals in Vickers hardness testing, coupled with calibrated microscopes, allowed indentation with forces less than 1 kgf.[14, 15] The advancement of microhardness testing allowed smaller specimens, finer features, and thinner plates to be tested. Some examples of the features that drove these developments were: measurement of wires, carburization and nitriding processes, and testing of layered composites.[14] This reduction in dimension required greater resolution at low depths, and thus more accurately machined tips, such as the rhombohedral Knoop indenter. However, Vickers and Knoop indenters showed opposing effects at low loads, where Knoop hardness increases at lower depths, while Vickers hardness often decreases or holds constant.[14]

This relationship, of decreasing hardness with increasing contact depth, has been termed the indentation size effect (ISE). As indentation loads and depths decreased, the

accurate measurement of hardness became increasingly difficult due to minimum loading requirements to produce plasticity, non-idealities in tip shape, and errors in measuring the residual impression.

By using depth-sensing indentation, which simultaneously tracks both the load and depth of the indenter the trend when examining shallow indents is increasing hardness increases with decreasing penetration depth.[16-18] Theoretically this could occur as a result of work of volume deformation energy balance in the creation of new surface area.[18, 19] This second theory would explain the $R^{-1/2}$ dependence for the hardness in shallow indents as the result of spherical tip rounding.

Other theories suggest that geometrically necessary dislocations result in a strain gradient in depth.[16] This can be modeled for indentations with 200nm or greater in depth, but shallower indentations would require a perfectly sharp tip in order to generate the dislocations necessary for this theory. However, both the geometrically necessary dislocations and work of volume deformation approach continue to generate continued research interest. Thin film effects and ISE are evidenced in the high-stresses seen later in this chapter.

In addition to the issues with the ISE, the length scales under investigation have decreased. With the limitations of macro- and microindentation these features cannot be reliably probed. This requires the development of even more sensitive indentation equipment, with sub-nanometer resolution for depth penetration data, with sub-μN resolution in applied loads.

1.4.3. Ideal Contacts

Nanoindentation instruments give stable control of applied forces while simultaneously extracting depth dependence via computer controlled transducers. This necessitates new analysis methods, with the ability to measure both elastic and plastic properties. As the load is applied to a material, it first deforms elastically, according to Hertz's theory.

While Hertz may be most famous for his contributions in the field of

electromagnetism, his contributions to the field of mechanics are the foundations for elastic contact theory. This work was a side product of Hertz's graduate work in optics, and his concern with fringe effects from bending lenses. Hertz found a series of solutions for both static and quasi-static loading of the elastic contact between two ellipsoid paraboloids with shapes of $z_1 = A_1x^2 + cxy + B_1y^2$ and $z_2 = A_2x^2 + cxy + B_2y^2$, offering a general form for elasticity with only normal displacement, and only for some stress components.[20, 21] By simplifying the results for the ellipsoids, one can find the elastic solution for the contact between two ideally smooth, isotropic, and continuous spheres. Non-spherical geometries will be introduced later in this chapter. If one considers that the mean pressure, p_m, at the contact surface is a continuous function (finite first derivative), then each material must support an equal load, P, as determined by radius, a, and the modulus of elasticity, E, Eq. 1.3, where the system is composed of two materials, the indenter (1), and the material being probed or "substrate" (2).

$$\frac{p_m}{E_1} + \frac{p_m}{E_2} \propto a\left(\frac{1}{R_1} + \frac{1}{R_2}\right) \qquad \text{Eq. 1.3}$$

Knowing that the projected area of a sphere is a circle, the total load is

$$P = p_m \pi a^2. \qquad \text{Eq. 1.4}$$

Rearranging for the radius of contact;

$$a = \left(\frac{3PR}{E^*}\right)^{1/3} \qquad \text{Eq. 1.5}$$

The quantities R and E^* are the effective radius and modulus of the system, or reduced radius and modulus respectively, defined in Eqs. 1.6 and 1.7. Since an indentation results in a "plane-strain" condition, a factor of $(1-\nu^2)$ is introduced, where ν is Poisson's ratio.

$$\frac{1}{E^*} = \frac{(1-\nu_1^2)}{E_1} + \frac{(1-\nu_2^2)}{E_2} \qquad \text{Eq. 1.6}$$

$$\frac{1}{R} = \frac{1}{R_1} + \frac{1}{R_2} \qquad \text{Eq. 1.7}$$

The radius of contact, for a rigid indenter, as found by Eq. 1.5, shows that for a given elastic penetration, δ, into the free surface it can be shown that the radius of contact, a, is located at $\delta/2$, figure 1.1.

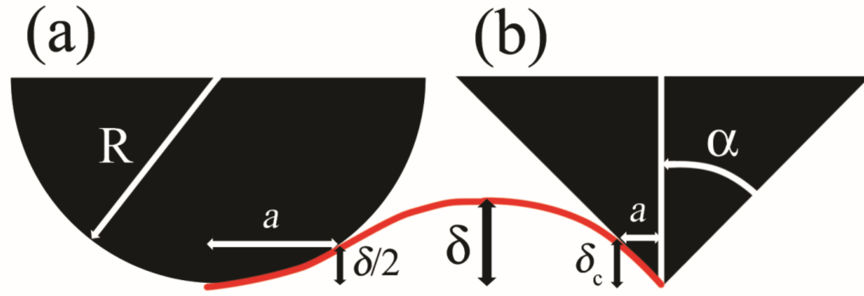

Figure 1.1. Contact of a rigid sphere **(a)** and a perfectly sharp cone **(b)** into an isotropic elastic half-space (shown in red). The contact radius is located at $\delta/2$ for the sphere, but is related to α in the case of the cone, Adapted from Fischer-Cripps.[22]

The total approach is $\delta = \delta_1 + \delta_2$, when deformation occurs in both indenter and substrate. In this case caution must be taken that the overall shape of the indenter remains spherical. The approach can be calculated as:

$$\delta = a^2/R = \left\{\left(\frac{3P}{4E^*}\right)^2 \frac{1}{R}\right\}^{1/3} \qquad \text{Eq. 1.8}$$

For most cases, the diamond indenter radius remains constant, (due to its high E), and δ_2 is ignored, thus equating δ_1 and the total penetration distance δ.

By using Eqs. 1.4 and 1.5, an expression for the mean contact pressure can be used to derive a stress-strain relationship.

$$p_m = \frac{P}{\pi a^2} = \left(\frac{4E^*}{3\pi}\right)\frac{a}{R} \qquad \text{Eq. 1.9}$$

This relates the indentation stress, represented by p_m, to the ratio of a/R, signifying the indentation strain. This relationship provides a means to the correlate the Tabor relationship, using hardness, to Hall-Petch, which uses the yield strength.[23] The pressure distribution, with r as the radial distance from the center of contact is given in Eq. 2.10. The maximum pressure, p_0, will be 1.5 times the mean contact pressure.[13]

$$p = \frac{3}{2} p_m \left\{1 - \left(r/a\right)^2\right\} \qquad \text{Eq. 1.10}$$

The above equations can only be applied for spherical indenters loading curved or ideally flat isotropic substrates. Application of these results to complex non-spherical indenters as well as generalizing the stress fields is an area of ongoing research.[21] Utilizing Boussinesq's problem for elastic contact, Sneddon found solutions for both the flat punch and a conical indenter.[24-27] The total load-depth relationship found for axially symmetric indenters, such as a cone (figure 1.1b), is that of Eq. 2.11, where A is a function of the depth, δ.

$$P = \int 2E^{*}\sqrt{\frac{A}{\pi}}d\delta \qquad \text{Eq. 1.11}$$

Upon integrating, for the axially-symmetric spherical indenter with tip radius R;

$$P = \frac{4}{3}\sqrt{R}E^{*}\delta_{c}^{3/2} \qquad \text{Eq. 1.12}$$

This then recovers the Hertzian relation for total displacement, δ, to the load, P for spherical indenters.

In nanoindentation, the surface of the material is often found by slowly stepping the tip down to the substrate until a reactive force is sensed. This acts as a zero-point depth, similar to the pre-load used in Rockwell testing. This loading is assumed to be 100% Hertzian in nature, causing no permanent change in the material. This will be shown not to be the case for some materials in chapter 3.

1.4.4. Ideal Contacts: Elasticity simulations

The elasticity simulations in this thesis are performed using the commercial FilmDoctor™ software.[28] This software has the flexibility to perform multilayer thin film elasticity calculations under both normal and transverse modes of indentation with a non-ideal tip shape. The model used is that of the effectively shaped indenter,[29, 30] described more fully in §1.46. However, this model uses an idealized isotropic elastic-half for the indentation substrate, while this software calculates the elastic stress in multilayer systems.[31]

However, roughness can only be simulated as the contact between the tip and a single asperity. Additionally, the model used in the simulations does not normally

include frictional effects between the indenter and the surface, which will underestimate the amount of strain in tension at the surface. To calculate the upper bound strain in these calculations, an ideal spherical tip shape will be used with a "no-slip" condition for indentation radius, *r*, in the region $0 \le r \le a$.[13] However, despite these limitations, the ability to simulate the stress distribution in single and complex multilayer systems is essential to the understanding of film fracture.

1.4.5. Contact: A transition from elastic to elastic-plastic, and fully plastic

As the load is applied, the initial loading is Hertzian with mean pressures, $p_m < 1.1Y$ (as calculated by Eq. 1.9). From Eq. 1.9, it can be seen that in the case of an elastic indent for a spherical indenter, that a simple relationship exists between the contact radius and the displacement

$$a = \sqrt{\delta R} \qquad \text{Eq. 1.13}$$

The elastic loading is followed by the development of a small amount of plasticity. This is the elastic-plastic loading region and the defining mean pressure is $1.1Y < p_m < CY$, with *C* defined in Eq. 1.1, but is typically ~3 for metals.

This coexistence of both elastic and plastic regions is a result of Eq. 1.10, where the magnitude of the pressure near the center of the indenter is larger than that near the edges. Due to frictional effects, the stress becomes tensile rather than compressive at the edge of the contact. This results in regions of high stress undergoing plastic deformation surrounded by an elastically deforming region of low stress, figure 1.2a. However, it is well known that metals deform primarily in shear, figure 1.2b,

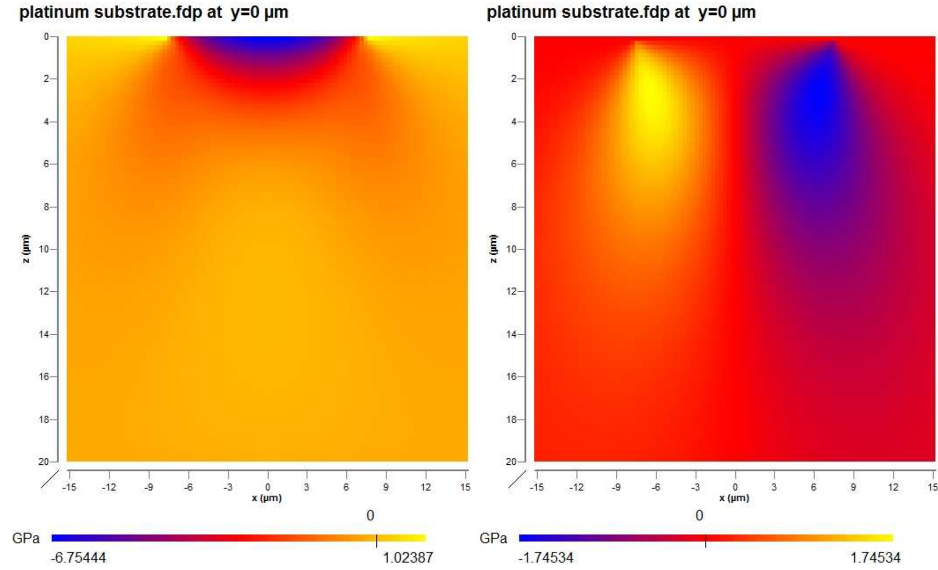

Figure 1.2. **(a)** Simulation of a normal stress distribution for a 20μm radius spherical tip at 1N load into (100) single crystal platinum. **(b)** Simulation of the shear stress under the same conditions as **(a)**.

therefore the regions of primary deformation do not always occur at the region of maximum pressure magnitude. The maximum shear stress is defined as

$$\tau_{\max} = \frac{1}{2}\left(\sigma_z - \sigma_x\right), \qquad \text{Eq. 1.14}$$

where +z is the axis of indentation, and x and y are equivalent for an axis-symmetric indenter. The Tresca yield criterion states that failure in all conditions will occur at

$$\tau_{\max} = \frac{Y}{2}. \qquad \text{Eq. 1.15}$$

However, the failure criteria used extensively in chapter 2 is slightly more complex, and requires the use of stress invariants, a derivation of which can be found in [32]. The von Mises yield criterion, figure 1.3, which more adequately correlates with experimental

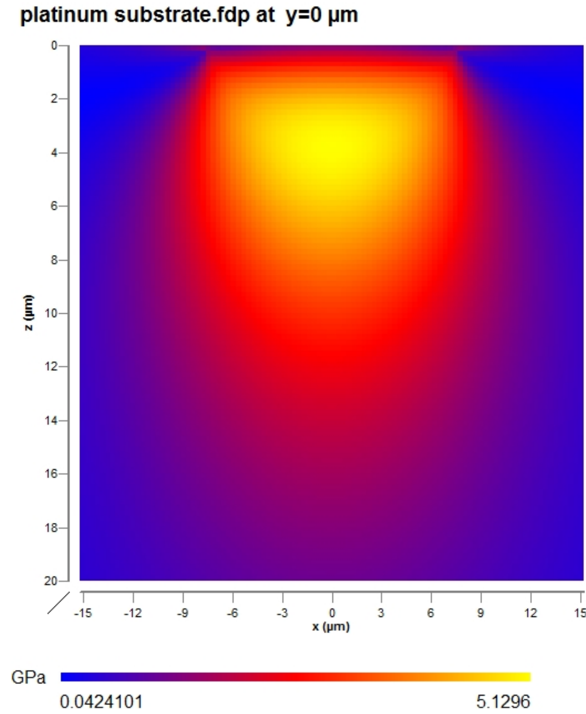

Figure 1.3. Simulation of the von Mises stress distribution for a 20µm radius spherical tip at 1N load into (100) single crystal platinum.

data, states that yield will occur when the second stress invariant, J_2, exceeds a fraction of the yield stress, where the fraction is directionally dependant,[33] such that yield will occur when the following is met;[34]

$$Y = \frac{\sqrt{2}}{2}\left[\left(\sigma_x - \sigma_y\right)^2 + \left(\sigma_y - \sigma_z\right)^2 + \left(\sigma_z - \sigma_x\right)^2 + 6\left(\tau_{xy}^2 + \tau_{yz}^2 + \tau_{xz}^2\right)\right]^{1/2}.$$

Eq. 1.16

In the case of uniaxial tension, this reduces to $\sigma_x = Y$, as does the Tresca criterion. Whereas the von Mises yield criterion is applicable primarily to metals and other ductile materials, a more appropriate criterion for yielding in ceramic materials is the Mohr-Coulomb criterion.[35] However, calculation of failure in this criterion requires the use of materials constants that can only be determined by analysis of a plot of shear strength versus failure. However, as the yield strength of ceramics in compression is greater than that of tension, a simple maximum principle strain criterion can be used.

$$\sigma_1 - \nu(\sigma_2 + \sigma_3) \le Y \qquad \text{Eq. 1.17}$$

Yielding under complex loading, such as indentation, is slightly more difficult. A simplified view of an incompressible material under a wedge indenter can be found in Johnson's cavity model [13] where the hydrostatic pressure, $\bar{p}$, can be given as

$$\frac{\bar{p}}{Y} = \frac{2}{3}\left[1 + \ln\left(\frac{E^* \tan(1-\alpha)}{3Y}\right)\right]. \qquad \text{Eq. 1.18}$$

It is understood that the stress is not hydrostatic, but that this pressure function allows us to approximate the normal, σ_z, and radial stresses, σ_r, as

$$\sigma_z \approx -\left(\bar{p} + \frac{2Y}{3}\right), \qquad \text{Eq. 1.19}$$

and

$$\sigma_r \approx -\left(\bar{p} - \frac{2Y}{3}\right) \qquad \text{Eq. 1.20}$$

respectively.

For values of $p_m \ge 3Y$, we find that the material at the edges of the indenter has started to deform plastically, with either pile-up or sink in of material at the surface being possible. Post-yield characterization of metals in the literature shows pile-up is likely when indented with a spherical indenter, and can cause more than a 60% change in contact diameter.[36] Furthermore, materials with plastic flow may strain harden, causing small deviations in the hardness that can be accounted for by using a strain function that contains a correction factor.

For spherical indenters, the geometric relationship

$$a = \sqrt{2R\delta_c - \delta_c^2} \qquad \text{Eq. 1.21}$$

holds for any contact, where δ_c is the contact depth, as opposed to δ, the total depth of penetration. For thin films, where after the commencement of plasticity that contact, due to some pile-up gives

$$\delta_c = \delta \ . \qquad \text{Eq. 1.22}$$

This gives an idealized method to calculate the change in contact radius during indentation, which does not require calculation of that contact from the unloading segment, as described in the following section.

1.4.6. Analysis for non-ideal geometries

Early experiments in instrumentated indentation showed that there was considerable information regarding all three regimes on loading, but that the difficulty lay in interpreting the information. Using the foundation laid by Sneddon regarding the rigid indenter and smooth, elastic half-space, Doerner and Nix reworked the equations for use in nanoindentation. They, along with many others, also recognized that just as the initial portion of the loading slope is elastic, so should be the initial unloading slope, figure 1.4.[25]

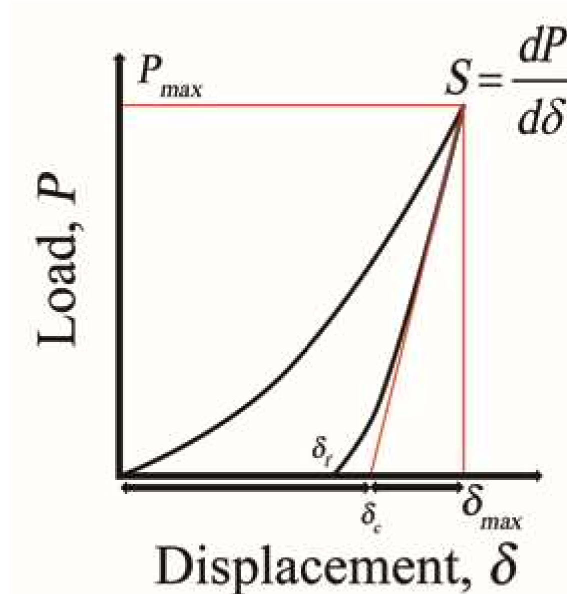

Figure 1.4. Idealized loading curve showing the elastic response on unloading. The stiffness is the slope of the unloading curve, and intersects the x-axis at the contact depth, δ_c, as was indicated in figure 1.1. Adapted from Oliver and Pharr.[25]

Utilizing the elastic response of unloading, Nix et al. found that the contact stiffness, S, on the initial portion of the unloading curve could be defined as Eq. 1.23,

where A is, the projected area of contact. A is assumed to remain constant in the initial stage of unloading.

$$S = \frac{\partial P}{\partial \delta} = \frac{2}{\sqrt{\pi}} E^{*} \sqrt{A} \qquad \text{Eq. 1.23}$$

Thus far we have neglected to mention that the most commonly used tip for nanoindentation is the Berkovich, a three-sided pyramid, with the parameters in table 1.1. The tip angle is designed match the strain relation of a Vickers indenter.[37] The cube corner, also in Table 1.1, is another three-sided pyramid, but with a smaller included angle. Care must be used as to what approximations are made with this tip. Schematics of these geometries are found in Fischer-Cripps.[22]

Indenter	**Ideal A_p**	**θ(°)**	**α (°)**	**β**	**f**	**m**
Spherical	$\approx 2\pi R h_p$	n/a	n/a	1	0.75	2.0
Berkovich	$= 3\sqrt{3} h_p^2 \tan^2 \theta$	65.27	70.3	1.04	0.75	1.5
Cube Corner	$= 3\sqrt{3} h_p^2 \tan^2 \theta$	35.26	42.28	1.03	0.75	1.5

Table 1.1. Ideal projected area, semi-angle θ, effective cone angle α, intercept factor f, power law exponent m, and correction factor β for the most common tip geometries. Adapted from Fischer-Cripps and Oliver et al. [22, 24].

Oliver & Pharr advanced the work of Nix et al, when they recognized that in many materials the initial unloading slope was actually a power law,

$$P = A(h - h_r)^m \qquad \text{Eq. 1.24}$$

where the exponent, m, is typically taken to be 2, but can also be fit to multiple data curves with a least squares fit. Referring to table 1.1, we can see that both the exponent, m, and the representative strain, ε, are dependent on tip geometry [24, 25]. Here the strain, ε, is related to radius of the spherical indenter, R, by

$$\varepsilon = 0.2 \frac{a}{R}. \qquad \text{Eq. 1.25}$$

Hardness in this analysis is calculated by using the projected area at a given contact depth, δ_c, for a given tip geometry, Table 1.1, at maximum load, $P_{\max}$.

The correction factor, β, in Table 1.1 must also be introduced to explain the difference between indented and zero pressure modulus of materials. It is related to tip shape factors and frictional effects. To take this into account we must correct the value of the stiffness [25, 38]

$$S = \frac{\partial P}{\partial h} = \frac{1}{\beta}\frac{\partial P}{\partial h}_{measured}. \qquad \text{Eq. 1.26}$$

Recent work by Mook, et al. [39] suggests that β may not in fact be a correction factor for indenter geometry alone. In this case the increase in β from expected geometric conditions may actually be a correction factor for the pressure effects on the bulk modulus, κ; as found in the geomechanics literature.[40]

Additional methods of analysis focus on the plastic work done by the indenter on the substrate, and dynamic indentations that oscillate the tip on loading, effectively creating many small load-unload curves.[22] The use of methods that describe the contact in terms of energy are uncommon, but useful in some cases, while the method of dynamic oscillation is commonly used on soft materials and viscoelastic materials.

1.5. Electrical contacts

The Maxwell model relates contact area to changes in conductance caused by a constriction in the electronic transport in the diffusive regime, where the contact diameter, *d,* is much larger than the mean free path of the electron, λ. The Maxwell conductance, G_M, has a linear relation with the contact diameter, *d*, and is inversely proportional to ρ_e, the average resistivity of the indenter and substrate. This gives

$$G_M = \frac{d}{\rho_e}. \qquad \text{Eq. 1.27}$$

This model assumes a circular contact between two identical, isotropic, and semi-infinite materials with no thermoelectric effects. However, it has been shown [12] that this model can also be derived for a circular constriction for a “ball and flat” model.

For contacts where the mean free path is greater than the contact diameter, $(d < \lambda)$, electrons behave in a ballistic manner, that is, without scattering.[41, 42] This

occurs with contacts areas on the order of a few nm^2. The Sharvin limit is a geometric limit imposed on current flow. Here, the conductance is found to be proportional to the square of the contact diameter,

$$G_S = \frac{3\pi d^2}{16\rho_e \lambda}. \qquad \text{Eq. 1.28}$$

The transition between ballistic and diffusive contacts is described by the Wexler correction, which provides a smooth function connecting the Sharvin limit to the Maxwell limit. [43, 44] Calculating the Wexler conductance for $d \sim \lambda$, gives a value of approximately $2G_S$.

Combining equations 1.25 and 1.21, results in a conductance – depth relationship for a spherical indenter for thin films of

$$G_M = \frac{2\sqrt{2R\delta_c - \delta_c^2}}{\rho_e} \quad . \qquad \text{Eq. 1.29}$$

Similarly, the Sharvin limit conductance - depth can be defined as

$$G_S = \frac{3\pi\left(2\sqrt{2R\delta_c - \delta_c^2}\right)^2}{16\rho_e \lambda} \quad . \qquad \text{Eq. 1.30}$$

It is also known that, as a metal undergoes plastic deformation, changes in dislocation density cause a local decrease in the electrical conductance at the contact. This can be seen from the total resistivity, ρ_e, written as , [45, 46]

$$\rho_e = \rho_{impurities} + \rho_{phonons} + \rho_{dislocations} + \rho_{defects} + \ldots + DMR\,, \qquad \text{Eq. 1.31}$$

where $\rho_{impurities}$, $\rho_{phonons}$, $\rho_{defects}$ and $\rho_{dislocations}$ are impurity, phonon, defects, and dislocation contributions to the resistivity. Here we are employing Matthiessen's rule to write the total resistivity as a sum of individual contributions. Important for extremely large strains, an additional term for "deviations from Matthiessen's rule" (DMR), has been added. It is important to note that Matthiessen's rule has been used successfully by experimentalists for the measurement of dislocation density and point defect concentrations in metals and superconductors. [47, 48]

These limits pertain only to contacts between two metals. In the case of contact between nonmetals, single step elastic tunneling, inelastic tunneling, hopping transport

via defect states in the oxide, and metallic transport through pinholes are all possibilities and must be considered. Surface roughness effects can also play a large role in the actual contact area,[12, 49, 50] therefore the ideal projected contact area from §1.4 will likely not hold true for the electrical contact area.

1.6. Indentation equipment

The TriboIndenter® is a standalone mechanical testing instrument with a variety of add-on options, two of which are used extensively in this thesis; the nanoECR™ discussed in §2.2 and *in situ* scanning probe microscopy. Additionally, the *in situ* indentation unit uses a similar transducer and control unit. The TriboIndenter® consists of three main components, vibration control, probe operation, and a computer control and data acquisition interface. This instrument is the primary means of mechanical probing throughout this thesis.

A combination of path active and passive vibration control allows the isolation of the probe and sample from outside mechanical interference. The passive control consists of an engineered enclosure that isolates the instrument from acoustic noise and some thermal protection, while an electronic feedback system provides an isolation platform from mechanical coupling. The noise floor provided by this isolation is on the order of 0.2 nm for displacement resolution, and 100 nN for load resolution. Indentation with a 700 nm radius indenter, in displacement control held for 5 s at 70 nm into single crystal platinum, figure 1.5, has a standard deviation of 0.06 nm in displacement, with a maximum point to point variation of 0.24 nm.

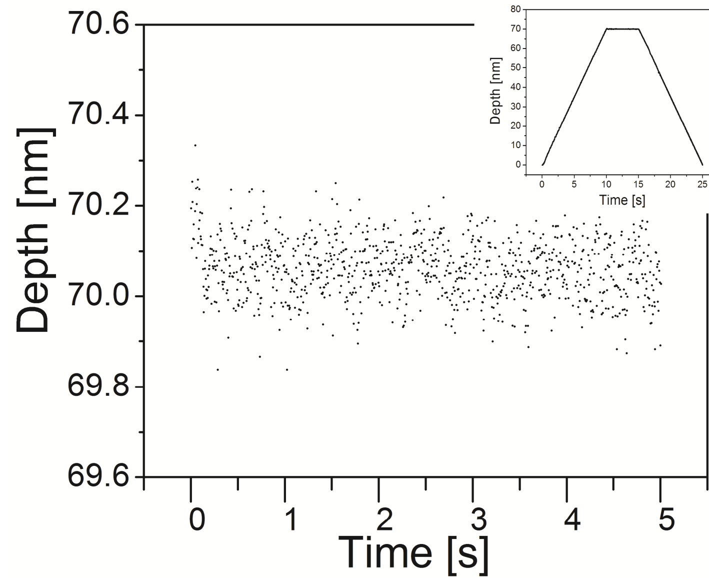

Figure 1.5. Indentation with a 700 nm radius indenter, in displacement control, held for 5 s at 70 nm into single crystal platinum. The varation in depth has a standard deviation of 0.06 nm, with a maximum point to point variation of 0.24 nm. Inset shows the entire displacement versus time curve for the indent. System was properly set up with the active vibration unit on a concrete slab away from railroads and large highways.

The probe operation consists of three main mechanisms; a stepper motor and drive system for accessing large distances between samples, a piezoelectric for x,y, and z adjustments at a smaller scale, and a capacitive transducer for the precise control. The tip is screwed into a plate in the center of the transducer structure suspended by four metal springs. The electronic schematic of the transducer is shown in figure 1.6, where the top and bottom electrodes are operated in AC with a 180° phase difference.

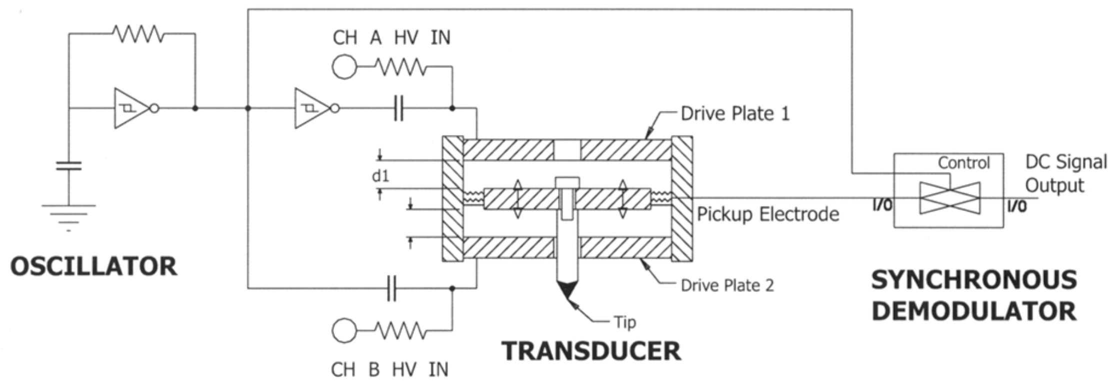

Figure 1.6. Schematic of the three-plate capacitive transducer as used in the Hysitron, Inc. TriboIndenter®. Additional systems on the left and right can be used to control the displacement in the x and y directions. Image courtesy of Hysitron, Inc.

The electric field at the center plate is zero when the center plate is in electro-mechanical equilibrium. By application of a direct current field at the top or bottom plate, the tip can be driven up or down by electrostatic interaction at the capacitive plate. The voltage, V, and distance, d_x, are related to the electric field, $\overline{E}$, by

$$\overline{E} = \frac{V}{d_x} \quad . \qquad \text{Eq. 1.32}$$

Where the voltage is the work done by the charge, q,

$$V = \frac{Fd_x}{q} \qquad \text{Eq. 1.33}$$

The transducer system is calibrated through extension in air, giving it an effective spring constant, and determining the voltage – displacement relationship in a known medium. This can now be used to apply a force while simultaneously measuring the displacement in the same transducer system.

The transducer has a maximum force and extension of ~12 mN and 3 μm respectively. The piezoelectric tube allows for rastering of the tip across the sample in x and y, recording z with loads (as measured in z) as small as 1.1 μN. In this mode the system can be used as a scanning probe microscope with the indenter tip used as a scanning probe. Additional side-mounted three-plate transducers allows “scratch testing,” or indentation followed by x-translation, and “wear mode” where the tip is rastered across

the surface using forces larger than in imaging mode. Wear mode can show relative amounts of material worn away as a function of load and number of passes.[51] The lateral force can be measured to find the coefficient of friction.

A computer interface between the instrument and the user allows the adjustment of loading rate, feedback mechanisms, scanning, and other parameters. The simplest control mechanism is "open loop," OL, where no feedback is applied, but a maximum load and target loading rate are set for the indent. The loading rate and maximum load are only targets, and are not guaranteed with this control. Load control, LC, indentation applies the feedback to both the loading rate and the maximum load. For some materials this feedback mechanism may become unstable, and adjustment of the PID must be made. The third control mechanism is displacement control, DC, and applies feedback to achieve target depth and displacement rate. This is the least stable control mechanism as penetration depth is not directly controlled, with the feedback from the depth measured and then applied to the indenter load. Fine adjustments to the PID are essential for reliable data with DC. However, DC mode has the ability to register the finest features.[52] The computer interface also serves as data storage.

The nanoECR™ option is an add-on for the TriboIndenter® testing system. It combines a conductive probe, a Keithley source and multimeter, and a data acquisition card. The circuit, shown in figure 1.7, measures tip-sample interaction as well as series resistances of the boron doped diamond (BDD) tip, 366Ω, the oxide film, R_{film}, the instrument wiring, <1Ω, the Au wire from sample to to stage, , <1Ω, and the copper mounting surface, ~1Ω, and the film of interest, typically several hundred ohms.

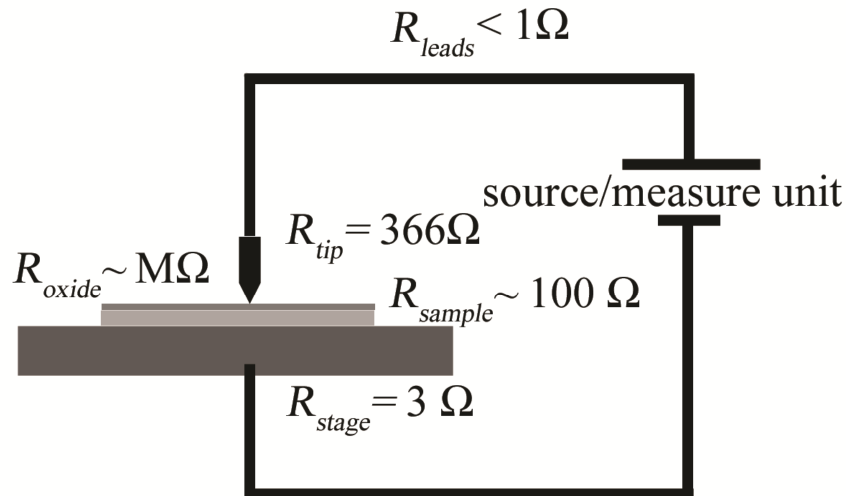

Figure 1.7. Schematic of the two terminal nanoECR™ test set-up. Some of the resistive elements contribute very little to the overall resistance, but must be included for completeness. Although resistance along the length of the tip is 366 Ω, the contact, with 11kΩ of resistance taken at 300nm displacement into Pt, dominates the measurement.

Either current or voltage bias can be supplied via the Keithley 2602 source-meter, and is read by the same device. This data is then transmitted via a 100MHz data acquisition card, is averaged over a user variable time period, and is stored with a one to one correlation with time, load, and displacement. The user interface is via an additional window with the computer software package. The current noise floor of the nanoECR™ has been shown to be in the 15 pA range, with a resolution of 5 pA, with the corresponding voltage values of 10 μV and 5 μV. The conductance, *G*, is calculated from the measured current, *I*, divided by the applied voltage, *V*, i.e. we display conductance as opposed to differential conductance. In addition to the DC measurements of resistance, the system can also perform current-voltage (I-V) sweeps to probe contact behavior.

Diamond is a wide band-gap (5.5eV) indirect semiconductor with high mobility and break down voltage [53]. Furthermore, it can be doped as a p-type semiconductor with a resistivity range of 18 orders of magnitude by using boron as an acceptor. Grain

boundary resistance plays a negligible role in the overall resistivity [53, 54]. The BDD tips used in this research project have a nominal resistivity of 3.3 Ω-cm. The BDD tips used in this study have been machined from single crystal boron doped diamond that is available through commercial laboratories.

The modulus of BDD was measured to be between 825 and 890 GPa by a beam bending method.[55] This was confirmed by the use of resonant frequency experiments performed on the beam, and did not appear to be a function of the B concentration. This is only about 80% of the modulus of pure diamond. This change in indenter modulus must be included when using BDD for calculation of the reduced modulus of the system, using methods described in §1.45. The change in the Poisson's ratio has been assumed to be small. Small changes in the Poisson's ratio do not have a large effect on the value in the reduced modulus assuming the E of the film is low compared to that of diamond.

Doping diamond with boron tends to increase the lattice parameter, and may be the cause of the reduction in modulus. The lattice parameter change may be due to interstitial boron, but this is uncertain. Measuring the change of the lattice parameter in compression testing shows that for pressures less than 25 GPa, and doping concentrations of less than 3 atomic percent that there appears to be no change in the compressibility of BDD as compared to diamond.

Initial doping concentration, as measured by preliminary wavelength dispersive spectroscopy, WDS, was 0.8±0.3 atomic percent, but the error results from an uneven indenter surface. The dopant concentration is assumed to be uniform.

The effect of using a semiconductor probe in a two–probe measurement is that behavior is non-Ohmic. The measurements of this will be discussed in detail in the next chapter. Therefore, in addition to the BDD tips used in the initial phases of this study, a conductive carbide tip was also used for conductive indentation. This tip showed linear I-V behavior, and was more conductive. However, due to the delicate nature of these tips a lower bias voltage was required. These carbide tips also have a lower modulus and hardness than the BDD used, and will therefore require different parameters for the calculation the area function.

Chapter 2. Plastic Response of Thin Film Systems

2.1. Overview

Conductive indentation has previously been used *in situ* to investigate phase transformations in Si[56] and GaAs,[57] for measuring dielectric breakdown,[58] to estimate the contact area under nanoindenter tips,[59] to evaluate wear of ionic thin films, [60] to probe the fracture of an oxide layer and subsequent pull off forces[61], and to investigate the presence of organic contamination layers.[62] These electrical contact resistance (ECR) experiments have shown that it is possible to extract qualitatively useful information regarding the deformation of the material under the indenter, above and beyond that of a simple load-depth profile. Additionally, such experiments have demonstrated that the theoretical and experimental contact areas of a spherical tip and flat surface could be correlated to, but not completely quantified with, the Maxwell conductance model as described in §1.5.[12, 63]

A key feature of many indentation load-displacement curves are discrete events occurring as changes in displacement with no change in load for load-controlled (LC) feedback, or changes mostly in load, in the case of displacement controlled (DC) feedback. In metallic systems, these loading curves suggest either nucleation or rapid multiplication of dislocations in the metal, or a fracture of the native or grown oxide surface layer.[64-70] While these deformation processes in the metal oxide overlayer system are physically quite different, the resulting indentation load-depth profile is similar. In this chapter, electrical contact resistance (ECR) measurements are taken *in situ* with depth-sensing nanoindentation in order to deconvolute these two processes. To determine the system behavior of conductive indentation, a platinum reference sample is used. The films under study are then characterized and tested, establishing a link between the measured conductance and plasticity within the sample. In addition to the investigation of overlayer failure on metal films, a preliminary investigation on the delamination of copper thin films is covered.

Regarding the specific metal films studied, it should be noted that both chromium and aluminum metals rapidly oxidize in air, but the oxide growth is "self-limiting." This results in an oxide layer about 1 to 2 nm in depth prior to becoming diffusion limited.[1, 2]

Note that native Al_2O_3 layers have been widely used as pinhole-free tunnel barriers,[3] whereas native Cr_xO_y layers are not so widely employed for tunnel barrier formation.[5] In sharp contrast to both of these cases, single crystal platinum does not form a native oxide, making it an ideal choice for use as a reference material in this study.

2.2. Platinum reference material

A laboratory grade (100) single crystal platinum specimen, with a surface roughness of 11 nm, is used as a reference material. The platinum was mechanically polished using 20 nm colloidal silica, and then subsequently cleaned by ultrasonication for 15 minutes in deionized water, isoproponol, and methanol.

2.2.1. Relating conductance to contact area

For conductive indentation using a boron doped diamond (BDD) indenter tip on platinum, figure 2.1, the current- voltage sweeps (I-V sweeps) show non-Ohmic behavior as a function of depth. The conductance can be calculated from the I-V sweeps as the slope of the curve in the nearly linear portion of the curve, from -300mV to +300mV, as plotted in figure 2.2 (a). The state of creep during the I-V sweep, where the applied load is held constant, would also affect the measured conductance.

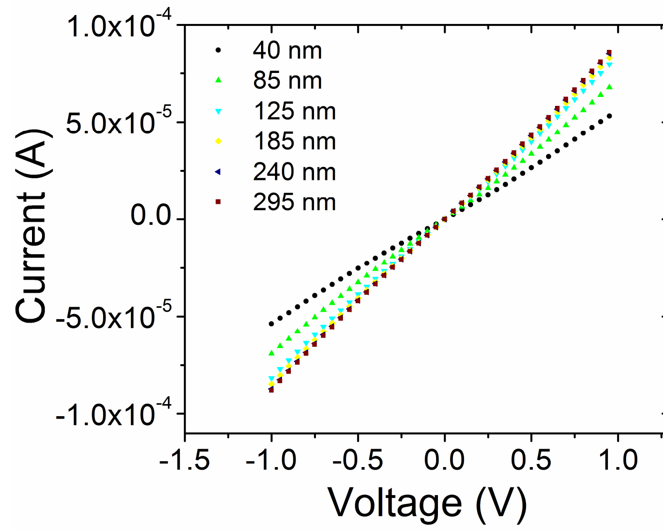

Figure 2.1. Current voltage sweeps taken during the constant load periods. The BDD indenter is a semiconductor, resulting in a nonlinear / non-Ohmic contact, even at large displacement.

The data from figure 2.2(a) can then be combined with the data taken during the loading segment of the indentation, calculated using

$$G = I/V \,, \qquad \text{Eq. 2.1}$$

at a bias voltage of 300mV, it can be seen that the continuously measured conductance slightly underestimates the conductance as measured by the I-V sweep, figure 2.2(b), which might be expected from creep considerations.

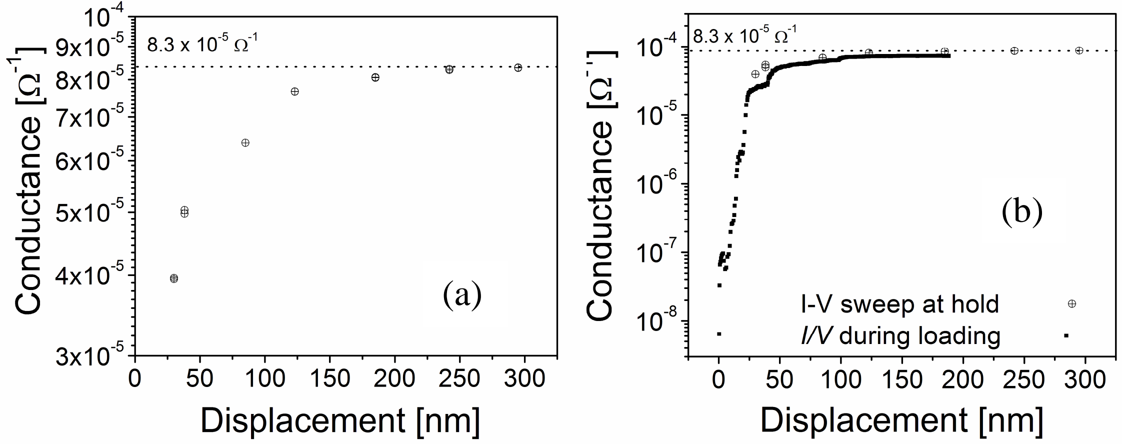

Figure 2.2.(a) A linear fit of the low voltage (±300mV) I-V sweeps from 2.1(b) gives for conductance versus depth on the Pt reference sample. **(b)** Conductance versus depth calculated during continuous loading of the sample by applying a DC bias slightly underestimates the conductance calculated from I-V sweeps. However, creep, figure 2.1(a), occurring during the I-V sweep causes an increase in contact area, increasing *G.* The dotted line represents the maximum conductance measured on the reference sample. The conductance is limited by contact area and the instrument resistances, as indicated in figure 1.7.

Using equations 1.29 and 1.30, shown here again for reference,

$$G_M = \frac{2\sqrt{2R\delta_c - \delta_c^2}}{\rho_e} \quad , \qquad \textit{Eq. 1.29}$$

and

$$G_S = \frac{3\pi\left(2\sqrt{2R\delta_c - \delta_c^2}\right)^2}{16\rho_e\lambda} \quad , \qquad \textit{Eq. 1.30}$$

the G –δ data in figure 2.2(b) can then be compared to the theoretical approach documented in §1.5, figure 2.3. Here however, $\delta = \delta_c$, cannot be assumed, as very little pile-up is observed on this sample. Instead, a series of indents were performed and the Olive-Pharr unloading curve analysis, §1.4.6, was used to calibrate the ratio δ_c / δ, which had a range of 0.82 to 0.93. The average resistivity was calculated to be 1.65Ωcm, half that of the boron doped diamond (BDD) tip, as the resistivity, on the order of μΩcm, of

the Pt was so low as to be negligible. The result, seen in figure 2.3, is that the measured conductance is an order of magnitude lower than that predicted by the Maxwell model.

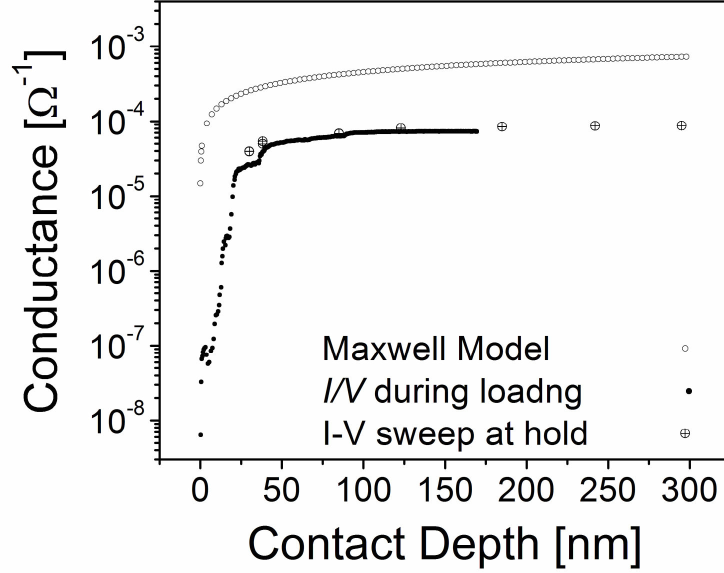

Figure 2.3. Conductance – contact depth for the Maxwell model of a 700 nm radius tip (open circles) compared to the results of figure 2.2(a). The measured conductance is an order of magnitude less than predicted, likely due to topographical features, where the actual area of contact is less than the predicted area of contact.

It should be noted that here the projected area of contact has been used. Comparing the projected area of contact to the surface area of the contact at a given depth, calculated by

$$A_{surface} = \pi 2R\left(2R - \sqrt{(2R)^2 - d^2}\right) \quad , \qquad \text{Eq. 2.2}$$

it can be seen, figure 2.4, that there is a maximum of 10% error at large displacements.

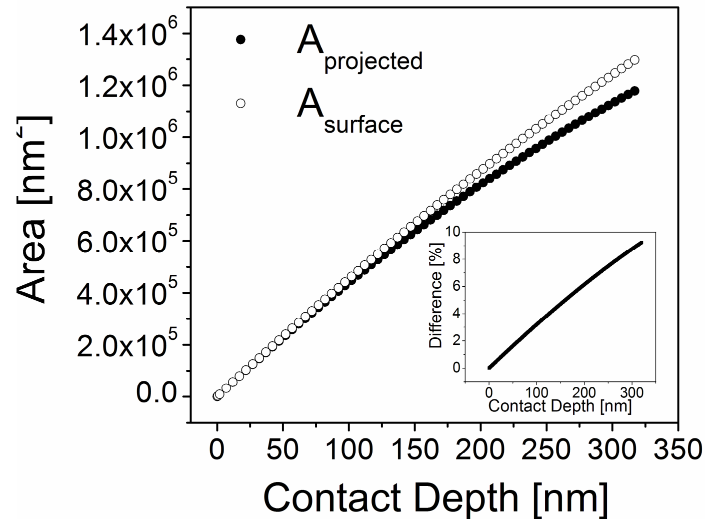

Figure 2.4. Comparison of projected contact area and surface area versus contact depth for a 700 nm radius tip. The percent difference – contact depth (insert) shows that at low depths (sub 50nm) the difference is on the order of 1 percent, growing to 10% at 300 nm.

2.2.2. Surface roughness effects

This large variation in theoretical contact area and actual contact area follows the findings of several other researchers, where the actual contact area is significantly less than the theoretical surface area.[12, 13, 49, 59, 71] The expected ratio of conducting to expected area can be lower than 1% in some cases, and is often less than 10%.[72] In figure 2.5, it can be seen that 1-D ridges of Cu can retain their original shape, even after considerable plastic deformation under load. The ridges shown have undergone some degree of plastic deformation, with their total strain having a similar value to the residual strain of the bulk material,[12, 73] but would still prevent the complete contact between the bulk surface and the indenter.

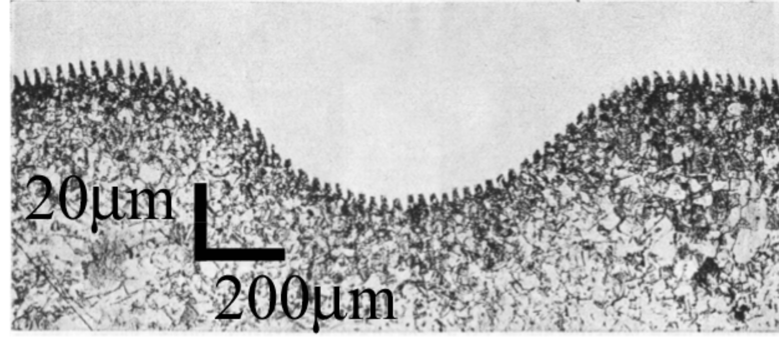

Figure 2.5. One-dimensional grooves cut into annealed copper show that the load from a spherical indenter does not flatten the asperities. The residual plastic strain of the asperities is only a few percent greater than the plastic strain of the bulk material. Adapted from A.J. Moore, et al.[74]

These ridges strain harden, developing greater hardness than in the bulk. Indentation hardness testing is normally not negatively affected as long as the indent depth is much greater than the surface roughness. However, in the case of shallow indents, the surface roughness can be on the order of the indentation depth, affecting the reliability of indentation testing at low loads.

The simple surface of figure 2.5 can be approximated as one-dimensional waves, with wavelength λ and amplitude Δ. If this surface is brought into contact with an ideally smooth elastic half-space, the apex of the waves will deform first. The height variation between the two materials can be found as[49, 73]

$$h(x) = \Delta\left(1 - \cos\left(\frac{2\pi x}{\lambda}\right)\right) \quad . \qquad \text{Eq. 2.3}$$

The total displacement, for both materials is $\delta - h(x)$, with a pressure distribution of

$$p(x) = \bar{p} + \frac{\pi E^{*}\Delta}{\lambda}\cos\left(\frac{2\pi x}{\lambda}\right). \qquad \text{Eq. 2.4}$$

This means that for uniform pressures, $\bar{p}$, of smaller magnitude than $\frac{\pi E^{*}\Delta}{\lambda}$, the actual contact, A, area will be smaller than the apparent contact area, $A_{apparent}$, e.g. the case of two smooth surfaces.

In this case the ratio of the real and apparent contact area is[13]

$$\xi \equiv \frac{A}{A_{apparent}} = \frac{0.762}{\sqrt{\Delta\kappa_s}}\left(\frac{\bar{p}}{E^*}\right)^{2/3} \quad , \qquad \text{Eq. 2.5}$$

with κ_s being the root mean squared (rms) curvature of the asperities.

By analogy, similar arguments can be made for a surface with random roughness. If the radius of a spherical tip is large enough, as is the case here, it can be approximated as being nominally flat compared to the roughness of the substrate surface. For the compression of a single asperity by a "flat punch," the contact area changes as

$$A_i = \pi a_i^2 \approx \pi\delta/\kappa_s \quad . \qquad \text{Eq. 2.6}$$

Here, a_i, is the circumferential radius of the asperity, and δ the distance it has been compressed. The Hertzian relation for pressure is then used with the asperity curvature replacing the radius of the indenter. The load required for the compression of a single asperity is thus

$$P_i \approx \frac{4}{3}E^*\kappa_s^{-1/2}\delta^{3/2} . \qquad \text{Eq. 2.7}$$

The corresponding "perfectly" plasticity equations are

$$A_i \approx 2\pi\delta/\kappa_s \qquad \text{Eq. 2.8}$$

for the area, and

$$p_i \approx \frac{6\pi Y\delta}{\kappa_s} \qquad \text{Eq. 2.9}$$

for the pressure. Approximating the asperity distribution as exponential rather that Gaussian, we can integrate over a number of asperities having rms roughness, σ_s, to find a relationship between real, A, and apparent, A_0, contact area:

$$\xi = \sqrt{\frac{\pi}{\sigma_s\kappa_s}}\frac{\bar{p}}{E^*} \quad . \qquad \text{Eq. 2.10}$$

The rms roughness of 11.1 nm was calculated for the reference sample using ISO 4287/1-1997, and the rms curvature of $1/112\ \text{nm}^{-1}$ from a line scan. Using the reduced modulus of 138 GPa and hardness of 900 MPa, the ratio of the areas is found to be 0.037, whereas the ratio of conducting and projected contact area calculated by

$$\frac{G_{measured}}{G_{Maxwell}} = \frac{d_{measured}}{d_{Maxwell}} \quad , \qquad \text{Eq. 2.11}$$

and

$$\xi_{elec} = \frac{A_{measured}}{A_{Maxwell}} = \left(\frac{d_{measured}}{d_{Maxwell}}\right)^2 \qquad \text{Eq. 2.12}$$

gives a value of 3×10^{-6} at 10 nm displacement, increasing to .015 at 300 nm displacement. The depth dependence is caused by the yielding of asperities, under the conditions described in §1.4. As the initial asperities yield, the indenter comes into contact with additional asperities. The high reported hardness here is likely due to the damage layer from mechanical polishing, which was neither annealed nor electrochemically polished. The high dislocation density within this damage layer could also cause a rise in resistivity, Eq. 1.31. However, to make up for the order of magnitude difference the Pt resistivity would need to be greater than 100 Ω cm. This is extremely unlikely in any scenario.

Additional analysis using FEM and multi-scale modeling show that the approximations from above scale well with fractal contact mechanics results.[13, 75, 76] Kogut, et al. showed that the general solutions for the elastic and fully plastic case could be worked out for both the Maxwell (bulk) and Sharvin (ballistic) contact limits. The ratio ξ between two rough but nominally flat surfaces was found to be linearly proportional to the dimensionless roughness through this region.[50] It can be seen that using a large radius indenter does little to counteract the effects of small asperities. Values of ξ close to unity could be attained if the radius of the indenter tip was on the order of magnitude of any asperities present, such as the carbide tip presented in §2.2.3.

Comparing the measured results to a Sharvin limit analysis requires the addition of the mean free path, typically no greater than 3 nm. The other bound area could be arbitrarily represented by an array of parallel cylinders of dimension 1 nm in diameter and length, using the measured conductance. Using the Sharvin conductance limit model, the contact area lower bound would be calculated by summing Eq. 1.30 over *N*

cylinders until $G = 2.1\times10^{-6}\Omega^{-1}$. The total contact area available for conductance would be $N \cdot A_{cyl}$, where A_{cyl} is the contact area of a single cylinder.

$$G = \sum_{i=1}^{N} G_S = \sum_{i=1}^{N} \frac{3A_{cyl}}{4\rho_F l} \qquad \text{Eq. 2.13}$$

Using the values listed above, the number of cylinders, N, is found to be 235 for a total contact area of 46 nm^2. This can be compared to the tens of thousands of square nm in the ideal case of Hertzian contact. Therefore, the use of a parallel arrangement of Sharvin contacts gives the lower bound on the actual conducting area, and the Maxwell model the upper bound.

2.2.3. Electron Tunneling

The use of either current versus voltage, I-V, or differential conductance $\left(G = \partial I / \partial V\right)$ versus voltage, G-V, sweeps are one of the methods pioneered by Rowell to verify tunneling in superconductor-insulator-superconductor systems.[77, 78] While this method does not confirm tunneling in metal-insulator-metal systems, it has been shown to be useful in measuring an effective barrier thickness.[79] The method of Brinkman-Dynes-Rowell,[78] where the differential conductance is normalized to 1 at 0 V, involves a fit to a parabolic model derived from the trapezoidal Jeffreys-Wentzel-Kramers-Brillouin (JWKB) approximation.[80-83] The average tunneling barrier height, $\bar{\varphi}$ in eV, and thickness, t in nm, can then be extracted as;

$$\frac{G(V)}{G(0)} = 1 - \left(\frac{A_0 \Delta\varphi}{160\bar{\varphi}^{3/2}}\right) eV + \left(\frac{9}{12800}\frac{A_0^2}{\bar{\varphi}}\right)(eV)^2 \qquad \text{Eq. 2.13}$$

where $A_0 = 4(2m_e)^{1/2} t / 3\hbar$, m_e is the effective electron mass, and $\hbar$ is Planck's constant over 2π. The difference in potential energy, $\Delta\varphi$, is the difference between materials 1 and 2. If the curvature of the I-V sweeps on Pt were, in fact, due to an organic contamination layer as was seen by Kim, et al.,[84] then using the Brinkman-Dynes-Rowell (BDR) fitting criteria would allow us to measure the thickness and barrier height of this junction. The fit of a second order equation to the normalized G at a contact depth of 31

nm, figure 2.6, results in a barrier height of 0.2V with a barrier thickness of 0.4 nm. The BDR criteria clearly state that the thinnest barriers need to be on the order of 1 nm for the fit to be valid. Therefore, a negligible contamination layer must be assumed.

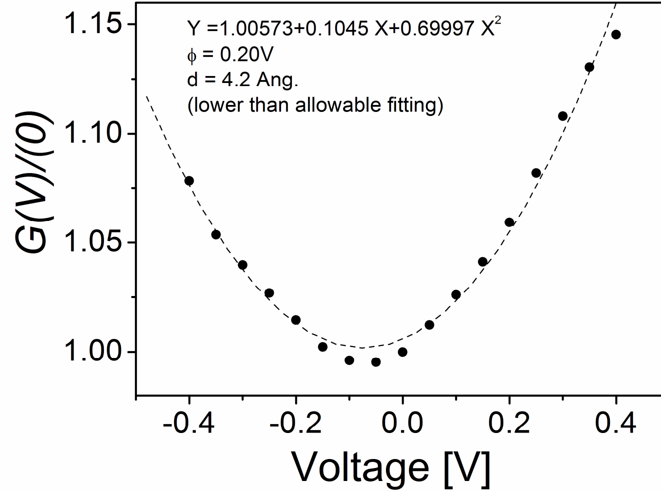

Figure 2.6. Fitting the derivative of the conductance normalized to the conductance at zero bias, and then fitting to a second order equation, following the criteria of Brinkman-Dynes-Rowell,[78] can give the barrier height and thickness for tunneling. The calculated barrier thickness is only half that of the lower bound of the fitting criteria, therefore the I-V curvature is not due to tunneling through a contamination layer.

It can be seen in equation 2.13 that the contact area required to calculate the current density, $J = {}^{I}\!/_{A}$, in the JWKB approximation has been canceled out in the normalization. This suggests that the non-ideal contact between the indenter tip and a rough surface does not need to be estimated, and that there is no asperity effect. However, the contact area must now be assumed constant during the hold period, i.e. no creep should occur. This method could then be used to measure contact area independent properties, such as compression of insulating layers in a metal-insulator-metal contact. Thus far, signal-to-noise ratio has prevented the use of this method for measurements in this thesis.

At least one researcher has claimed a correlation with the absolute value of the integrated I-V sweep and the contact area for indents at Newton loads into copper, but

could find no theoretical reasoning for this claim.[59] Mathematically, this integration of current versus voltage gives the power in the circuit, which, as Fang, et al. found, has no theoretical linkage to contact area. Integrating I-V for the reference sample here indicates that, even with a constant prefactor, no such relationship exists with either the idealized spherical contact, or the contact area determined from Oliver and Pharr.[24]

2.2.4. Indentation with carbide tips

In comparison to the Pt sample indented using the BDD tips, the results using a proprietary single crystal carbide tip, (indentation in figure 2.7 (a)), show linear, Ohmic, behavior, figure 2.7(b), albeit for low bias voltages. Due to the fragile nature of the carbide tip under larger biases, with reported cracking of the tips, the maximum applied bias was only 20mV.

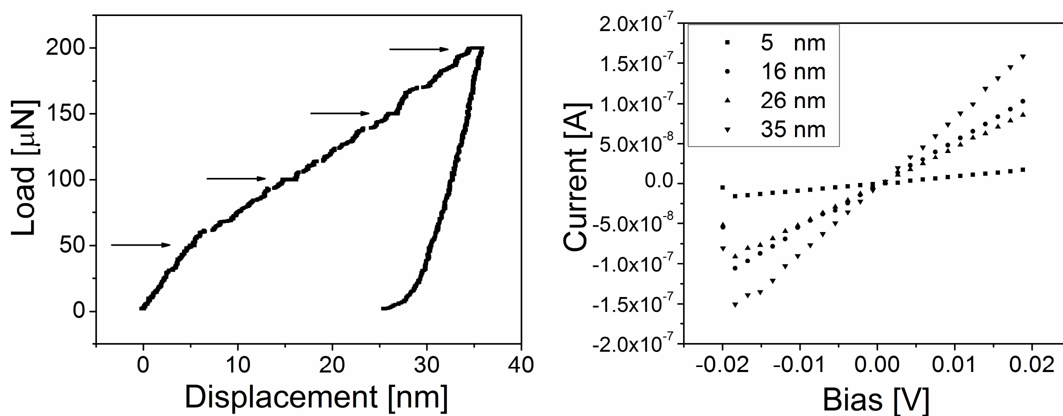

Figure 2.7.(a) The load depth curve of a Berkovich carbide tip with sub 100 nm radius of curvature in the Pt reference sample. Hold periods can be seen as creep, indicated by the arrows. Additional incipient plasticity is also visible in the profile, where jumps in load occur. The sharpness of the tip causes high stress, 1.2 GPa in this indent, resulting in pop-in events. The indenter radius is on the order of the radius of the asperities. **(b)** Current voltage sweeps taken during the hold periods. The carbide indenter is a metal, resulting in an Ohmic contact, as far as can be determined with the limited bias range. The initial points, at -0.02 V show that the sweep did not reach equilibrium during the specified acquisition time of 8.6ms for each point. Longer acquisition times result in more creep for the hold period.

Here, linear fits of the I-V sweeps giving conductance as a function of depth, figure 2.8, are considerably noisier when compared to the BDD data of figure 2.2. This is could be due to the lower bias voltage, smaller contact area, and possibly a contamination issue.

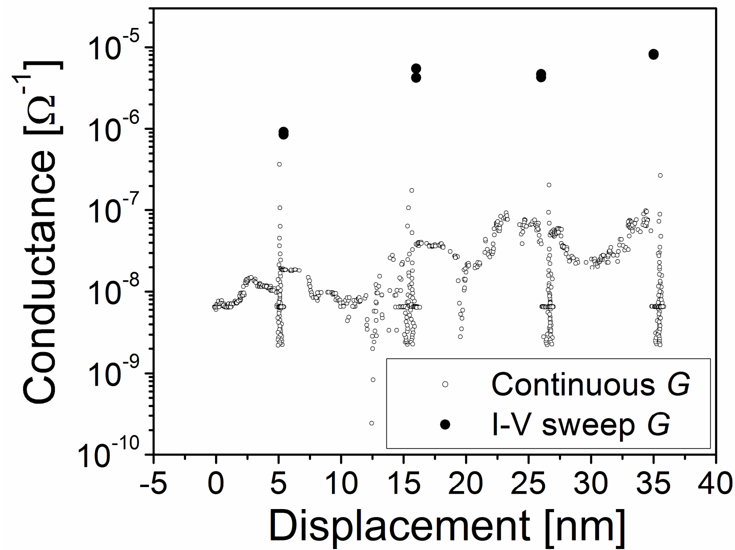

Figure 2.8. Conductance – contact depth for a sub-100 nm radius Berkovich tip (open circles) machined from a metallic carbide. The conductance measured from the I-V sweeps is two orders of magnitude greater than that from continuous indentation. The indent-to-indent variation of continuously measured conductance also varies by orders of magnitude. The use of this tip to measure values of conductance in Al films reveals that it contamination readily adheres to the tip.

Additionally, the continuous conductance is several orders of magnitude less than the conductance calculated from I-V sweeps. The individual sweep data points can also be seen in figure 2.8, and that the value of these individual points only approaches that of the conductance from the fit to I-V sweeps. Included in this graph are the data points used to calculate the I-V conductance, which also fall on this lower curve. This is likely due to the contact potential that develops when these two metals are brought into contact, and is a result of the work function difference between the tip (carbide) and sample (Pt). Additionally, there is an issue of acquisition time, 8.6 ms for each point on the I-V sweep, and 5 ms for each continuously measured point. The mean resistivity of these tips is 69μΩcm, four orders magnitude less than the BDD indenter.

2.3. Initial films of chromium and aluminum

2.3.1. Experimental Considerations and Structural Characterization

Chromium films, with thickness of 28 nm, were grown epitaxially in the (001) orientation on MgO (001) substrates by d.c. magnetron sputtering in a chamber with a base pressure of 10^{-9} Torr. The films were deposited (0.9 Ås^{-1}) at 200ºC in 3 mTorr Ar pressure after a 500°C vacuum anneal of the MgO (001). The deposition, structure and characterization were discussed in more detail in prior work.[85]

Aluminum films were deposited on substrates of Si(001) at ambient temperature by RF Magnetron sputtering with a 2.4 mTorr of Argon pressure at 0.7Å/s. Oxidation for the initial films was done by exposing the films to air.

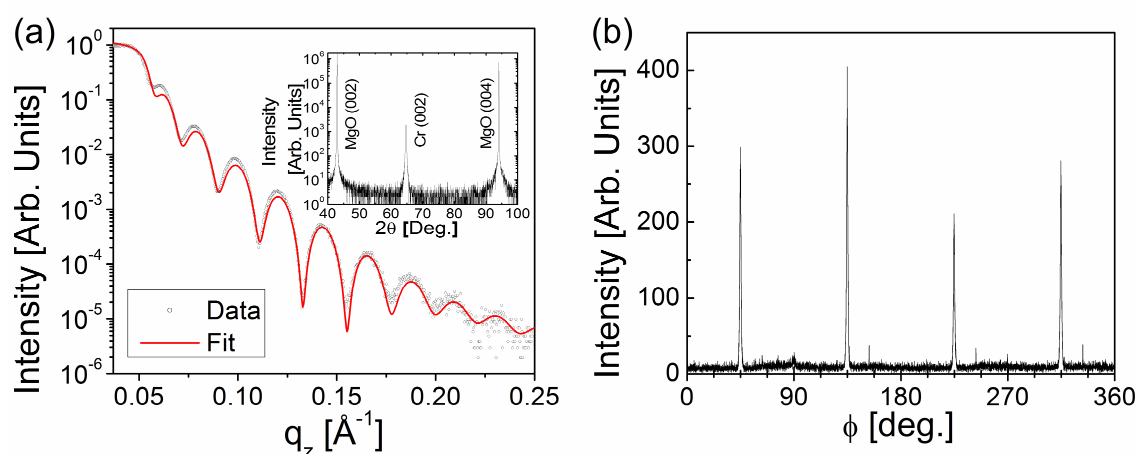

Figure 2.9.(a). Wide angle x-ray diffraction (insert) confirms an out of plane (001) orientation. $\lambda = \text{Cu } K_\alpha$. Grazing incidence x-ray reflectivity (open circles) and the fit (solid line) used for calculation of thickness and roughness for Cr/Cr_2O_3 system. **(b)** In-plane x-ray "ϕ-scan" shows a 45 degree rotated epitaxy expected for growth of Cr on (001) MgO. Scans are courtesy of Dr. Jeff Parker.

The films were then characterized *ex-situ* by high resolution wide-angle x-ray diffraction (figure 2.9(a), inset), rocking curve analysis (not shown), grazing incidence x-ray reflectivity (figure 2.9(a)), and in-plane x-ray diffraction (figure 2.9(b)). The wide-

angle diffraction confirms an out of plane (001) orientation, while the in-plane "ϕ-scan" demonstrates in-plane, "45 degree rotated" epitaxy. The rocking curve full width half maximum of 1.0 degrees confirms a reasonably low degree of mosaic spread. The measured x-ray reflectivity profile (GIXR) was compared to the results of standard simulations [86] (figure 2.9), resulting in extracted rms top surface roughness values (on the long lateral length scale probed in this technique) of 0.9 nm. Figure 2.10 shows the density depth profile, converted from the extracted depth profile of the x-ray scattering length density. The density of the interior of the Cr film from the fit was found to be 6.95 g/cm^3, slightly less than that of bulk Cr (7.19 g/cm^3).

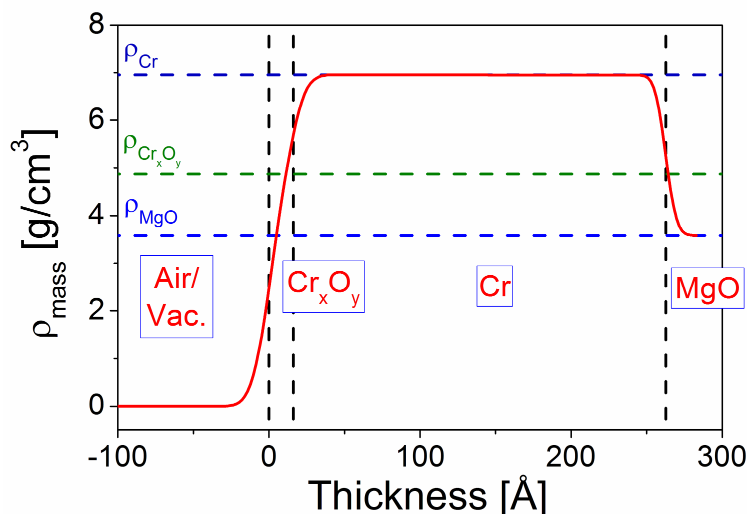

Figure 2.10. Density profile of the MgO/Cr/Cr_2O_3 film, generated from the fit of the grazing incidence x-ray data shown in figure 2.9. The thickness of the oxide film from this measurement was 1.6 nm. Fit courtesy of Dr. Mike Manno.

The Cr_xO_y layer, formed by natural oxidation, had a determined thickness of 1.6 nm, and was found to have a density of 4.87 g/cm^3, less than that of Cr_2O_3 (5.22 g/cm^3), and of CrO_2 (4.89 g/cm^3). Note that the density value for thin films is typically less than the bulk material, as was found in the fit for Cr metal. Thus, this characterization is consistent with formation of a predominantly Cr_2O_3 oxide. The rms roughness from 10 x 10 μm scanning probe microscopy scans was 0.5 nm, using the ISO 4287-1997 roughness standard, in reasonable agreement with that from the GIXR fitting of 0.9 nm.

Wide angle x-ray diffraction of the aluminum films revealed polycrystallinity with no strong texturing. A Williamson-Hall analysis of the peak widths showed little contribution from microstrain, and an average grain size (probing the direction perpendicular to the substrate surface) of 18 nm. The films were found to have lattice parameter around 0.406 nm, i.e. they were essentially relaxed. From GIXR measurements and simulations a surface roughness of 3.2 nm was determined.

X-Ray Photoelectron Spectroscopy (XPS) using a model SSX-100 by Surface Science Instruments, Inc. was carried out to further characterize the thickness and valence of the Cr in the native oxide from the chemically shifted $2p_{3/2}$ components. This instrument consists of a hemispherical sector energy analyzer and monochromated Al K_{α} x-ray source operated at a spot size of ~800 µm. Survey spectra were obtained at a pass energy of 150 eV and high resolution spectra were obtained at 50 eV. The energy scale was calibrated relative to the Au $4f_{7/2}$ (83.95 eV) peak and the Cu $2p_{3/2}$ (932.7 eV). This instrument is equipped with an angle resolved sample stage that can be used to vary the electron take-off angle. The acceptance angle of the energy analysis system is ~30 degrees, limiting the usefulness of variable angle studies; that is, the angular resolution at which data can be obtained limits the resolution of the depth profile. The samples were observed to be carbon contaminated. However, since it is unlikely that the carbon bonds to the surface (in the presence of a surface oxide), studies of the Cr $2p_{3/2}$ peak were performed to determine the oxidation state of Cr at the surface. Elemental cleaned Cr has its $2p_{3/2}$ peak located at 574.4 eV and its oxide occurs at ~576.4 eV.[87] Spectra were curve fit and the oxide peak was observed at 576.4 eV. The elemental peak was observed at ~573.7 eV. The small shift (0.7 eV) is due to the background and curve fitting procedure, which introduces inaccuracies in determining the peak position.[88, 89] The data, within experimental limits, are consistent with a thin oxide of predominantly Cr_2O_3 on Cr.

Nondestructive depth profiling analysis was done by variation of the subtended angle in three angular positions at grazing, 53, and ~70 degrees relative to the sample normal, as shown in figure 2.11, to provide a rough estimate of the oxide thickness. (see, for example ref. [90]) The intensity, I, of electrons escaping from the sample follows the Beer-Lambert law,[91]

$$I = I_0 \exp\left(-\frac{h}{\lambda_{esc} \sin\theta}\right) \quad , \qquad \text{Eq. 2.14}$$

where θ is the photoemission angle subtended relative to the sample surface, I_0 is the infinitely thick and clean substrate intensity, h is the depth, and λ_{esc} is the escape depth.

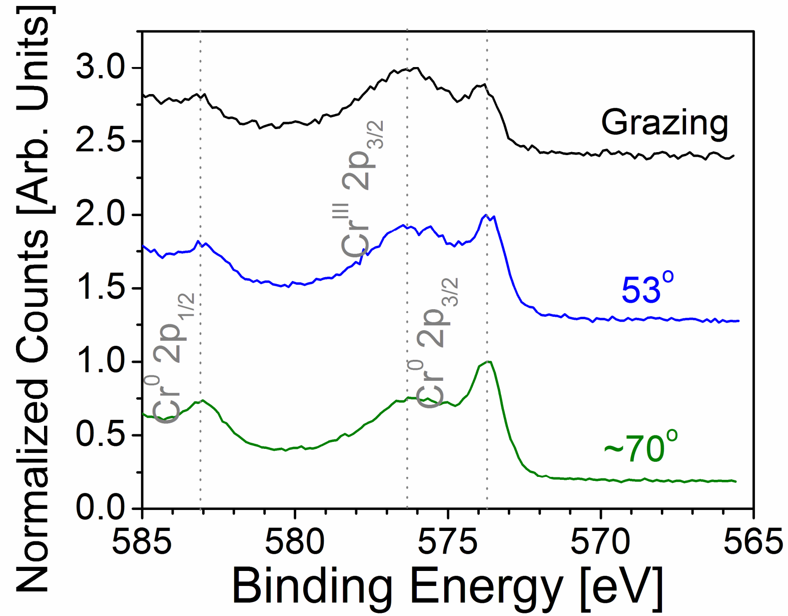

Figure 2.11. The change in the ratio of the $2p_{3/2}$ Cr^0 and Cr^{III} peaks can be used to give oxide film thickness. Grazing angles have the lowest penetration depth, and therefore the largest $2p_{3/2}$ Cr^{III} peak. Inversely, higher angles of incidence probe deeper into the sample. The oxide film thickness, from XPS depth profiling, was estimated at 2.0 nm.

If λ_{esc} is then assumed to be constant in Cr metal (Cr_M) and Cr oxide (Cr_O), the ratio of the intensities I_M/I_O can then be used to estimate the thickness of the oxide film. Analysis of the angle-resolved XPS data, using Eq. 2.14, for the $2p_{3/2}$ chemically shifted Cr, shows that the native oxide layer is approximately 2.2 nm thick. An escape depth of 2.7 nm,[92] and densities of the Cr_M and Cr_O of 7.19 and 5.22 g/cm^3, respectively, were used in the analysis. Deconvolution of the $2p_{3/2}$ chemically shifted Cr peak shows that there is some variation in the valency for the oxide as function of depth from the surface. This confirms the results of others who have investigated oxidized Cr and found that the surface oxide was mainly Cr_2O_3, with some CrO_2 at the metallic Cr interface.[93-95] A

small amount, ~2%, of hydroxyl bound Cr was also found at all takeoff angles. In summary the XPS and GIXR analyses are in reasonable agreement on the existence of an approximately 2 nm thick native oxide overlayer, of mixed Cr valency, but predominantly Cr_2O_3.

Load-controlled indents with maximum loads from 100 to 1000 μN were placed in 5 x 5 arrays with 10μm spacing between indents. Displacement-controlled indents were performed to provide more sensitivity regarding discontinuities for the Al films. An overpressure of N_2 gas was used to reduce the relative humidity from approximately 40% to less than 15% at ambient temperature. Samples were connected to a freshly cleaned copper substrate stage by 99.99% purity Au wire using 99.99 % purity In solder. Periodic cleaning in an ultrasonic bath to remove contaminants and maintain proper electrical contact was performed on the Boron doped Berkovich tip, of nominal 700 nm radius. The indentation depth and film thickness are within the spherical regime of the indenter.

2.3.2. Damage mechanisms within chromium and aluminum thin films

The first sign of contact plasticity in the Al/Al_2O_3 film is seen as a load-drop at 5.2 nm in the time versus load plot, figure 2.12, in a displacement controlled indent. After the commencement of plasticity, the contact diameter can be expressed as a geometric contact, Eq. 1.21. As stated in chapter 1, a geometric contact is chosen as pile-up is likely to occur to some degree in a thin metal film.

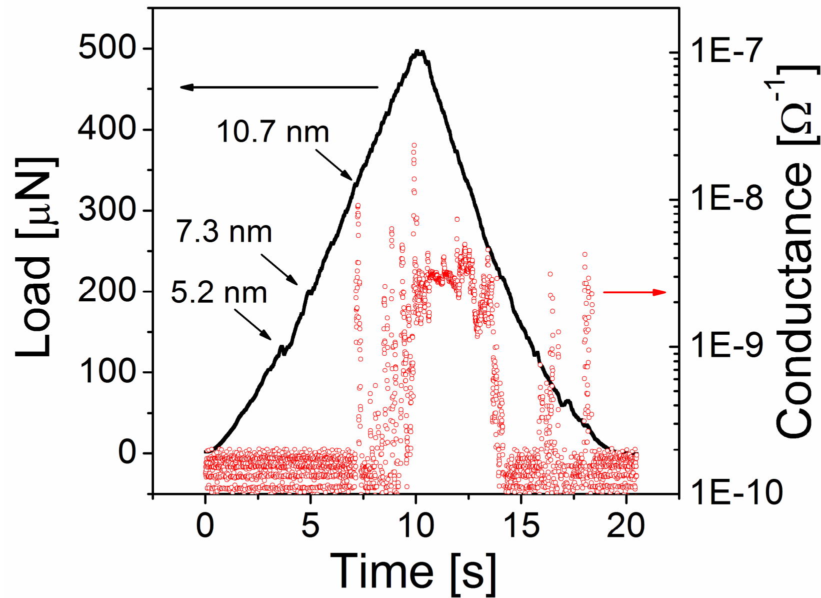

Figure 2.12. Load-time (solid squares) and the corresponding conductance (open circle) measurements for a typical displacement controlled indent to 15nm. Small load drops are seen at 5.2 and 7.3nm prior to oxide fracture at 10.7nm, indicated by the large rise in conductance

Displacement controlled indentation is used here to provide additional sensitivity to discontinuities.[52] Loading continues in an elastic-plastic fashion, with minor load drops at ~7.3 and 10.7 nm. A residual plastic depth of 4 nm remains after unloading. The absolute value of conductance at the initial contact is $G \leq 10^{-11}\Omega^{-1}$ until the load drop occurring at ~10.7 nm. At this point G rapidly rises 2 orders of magnitude reaching a maximum value of $2.3 \times 10^{-8}\Omega^{-1}$. A nominal value of $3 \times 10^{-9}\Omega^{-1}$ is maintained through the initial unloading period, with two sudden increases prior to contact being broken. The initial low value of G is expected, as the native oxide layer on Al is well known to form a good insulating tunneling barrier. For indentation to larger displacements, the conductance is seen to rise exponentially after breakthrough, as seen in the load controlled indent to 600μN/28nm, figure 2.13. Here, the load depth profile, figure 2.13, indicates Hertzian elastic behavior for the first 3 nm before the onset of elastic-plastic behavior.[20]

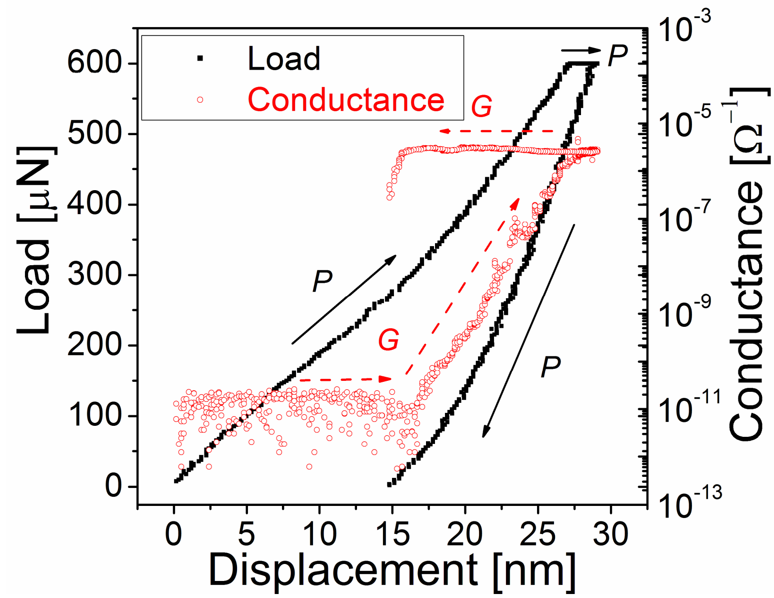

Figure 2.13. Load-depth (solid squares) and the corresponding conductance (open circle) measurements for a typical 600 μN under load-control indent into the Al/Al_2O_3 film. The conductance rise after initial onset is 5 orders of magnitude.

This result is similar to that presented by Pethica, *et al*, for Ni samples with native oxide, figure 2.14[61] where oxide fracture is observed with a large increase in *G*, albeit with one significant difference.

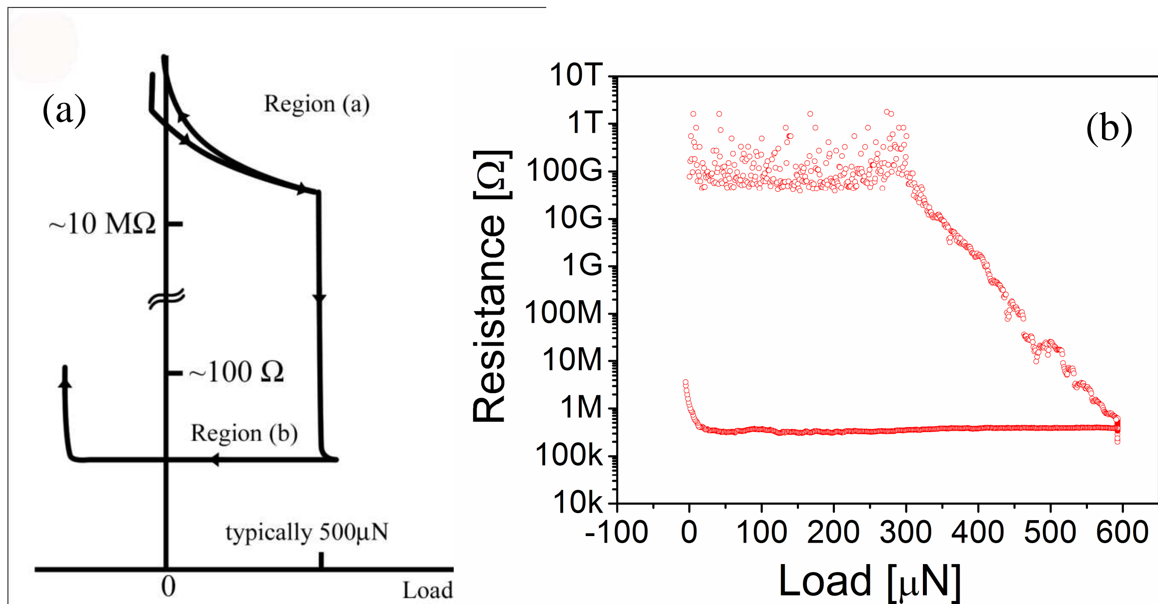

Figure 2.14.(a) *In situ* electrical measurements with a sharp probe on oxidized Ni single crystal showed that no fracture occurred in region a, followed by a sharp onset of current. Region b was characterized as a metal-metal contact, with significant pull-off forces. Adapted from Pethica, et al.[61] **(b)** The data from figure 2.13(b), replotted using resistance, for comparison to the classic Pethica example of 2.14(a).

Whereas Pethica, *et al* observed Hertzian, elastic, contact prior to oxide fracture, the load depth profile shown here on Al/Al_2O_3 indicates a deviation from Hertzian behavior at approximately 3 nm displacement. After that, plasticity ensues, but *G* does not rise, which gives evidence to the integrity of the oxide film. At 10.7 nm displacement, however, *G* rises rapidly. We believe that this onset of *G* is directly due to the fracture of the oxide, occurring simultaneously with a load drop. The thin oxide layer, combined with a constrained thin film can account for this observation of elastic-plastic behavior prior to fracture. The Maxwell conductance can be calculated, Eq. 1.21, using the mean value of resistivity, $1.15\,\Omega\,\text{cm}$, as found from the resistivity of the indenter, $3.3\,\Omega\,\text{cm}$, and that of the Al film, $4.7\,\mu\Omega\,\text{cm}$. At a displacement of 15nm the theoretical value of the measured conductance is $1.3\times10^{-4}\,\Omega^{-1}$. This theoretical value involves the unlikely assumption that the entirety of the tip-sample contact can be described as being metal-metal. This is unlikely, for reasons described previously for the case of Pt, as well as the

introduction of a nonconducting oxide barrier. For a fractured oxide film, the actual contact area would be much smaller. The load-controlled indent, figure 2.13, shows that the G continues to rise exponentially, to a maximum value of $2.5\times10^{-6}\Omega^{-1}$. I-V sweeps, figure 2.15, taken at 30 nm displacement show that the contact is still non-Ohmic, which is as expected for a very small metal-metal contact. However, this could also mean that some barrier exists, for example a very thin gap of air. For example, if this were a ring fracture of 0.1 nm in width and 750 nm in circumference, having a contact area of 75 nm^2, using equation 1.29 to determine the conductance, the result would be a value of $G = 9.8\text{x}10^{-9}\Omega^{-1}$. This is quite close to the measured value at initial turn-on.

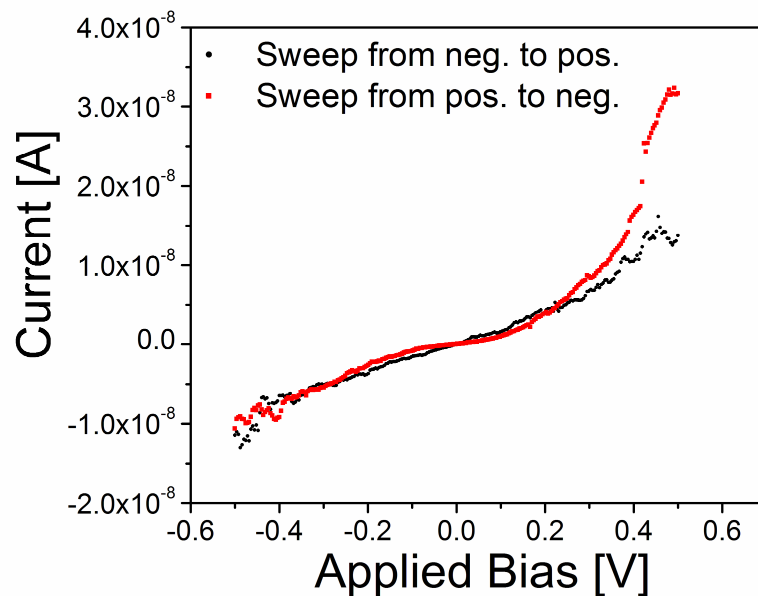

Figure 2.15. I-V sweeps taken after oxide fracture at 20nm displacement in Al thin films show that the contact is not Ohmic. This would be expected if the contact were very small.

Lets us now turn to the Cr system. Similar to Al/Al_2O_3, the load depth profile in the Cr/Cr_2O_3 is Hertzian for the first few nm at which point a deviation of P proportional to $\delta^{3/2}$ is observed, figure 2.16). A large displacement excursion is seen at ~8 nm, of approximately 0.75nm in length. After the excursion is arrested, the sample reloads in an elastic-plastic fashion.

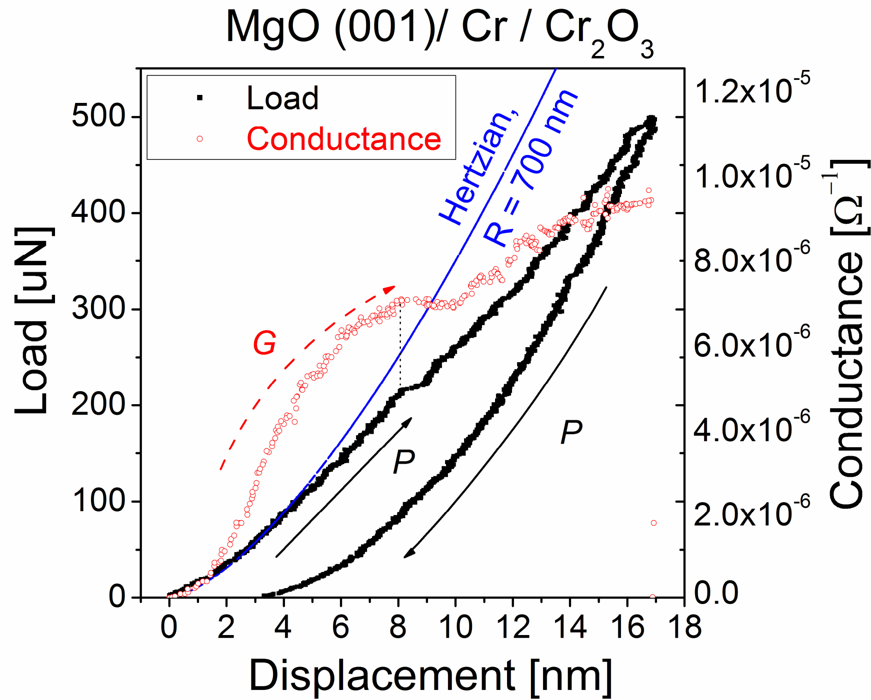

Figure 2.16. Load-depth (solid squares) and the corresponding conductance (open circle) measurements for a typical 500 μN indent into the Cr/Cr_2O_3 film. A deviation from Hertzian behavior can be seen prior to the large excursion at ~8 nm. A corresponding decrease in the conductance is observed coincident with the excursion. The conductance continues to decrease upon the reloading of the sample surface, indicating that dislocation plasticity continues decreasing the conductivity of the sample at this point.

In contrast to Al/Al_2O_3, the initial measured G is immediately greater than $10^{-8}\,\Omega^{-1}$ in the Cr/Cr_2O_3 system, even prior to the onset of plasticity. This native oxide system is known to be more difficult to establish tunneling conduction due to the formation of pinholes. Growth conditions control the pinhole density, but Cr films grown under similar conditions have been found to contain $\sim 4\times10^{5}/\text{mm}^{2}$ pinhole density, or a linear density of 1.5×10^{3} nm as determined by HCl decoration.[5] Conductive scanning at 2μN (figure 2.17(a)) showed almost no apparent evidence of current hotspots; however, as the scanning load was increased to 10μN (figure 2.17(b)) current hotspots were observed.

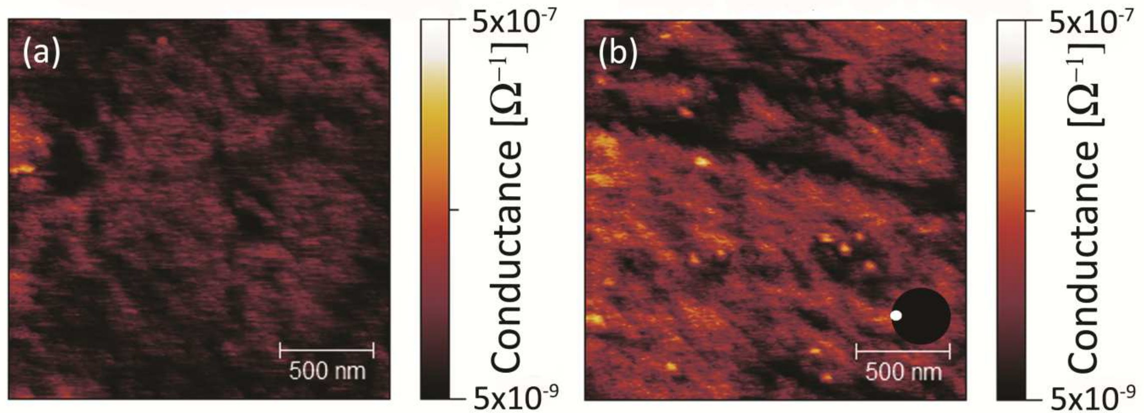

Figure 2.17.(a): A conductive scan of the Cr/Cr_2O_3 film using the indenter tip at 2 μN force shows a single conductivity hotspot. **(b)** As the perpendicular scanning force is increased to 10 μN force, more conductivity hotspots appear. The magnitude of these hotspots is similar to that shown in the first few nm of displacement during indentation. The two concentric circles near the scale bar are aids to the eye, indicating the area of the tip in relation to the figure for scanning at 10 μN (inset white circle) and at 320 μN nm load (larger black circle) for comparison. The load of 320μN (depth of 17 nm) is chosen to match the maximum load of the indent in figure 2.12.

The position of these hotspots did not obviously correspond to surface features, although they may be formed by the result of shearing action. The density of hotspots, 1.2×10^7 /mm^2, as determined from the 10μN scan, was found by using a conductance criteria of $9 \times 10^{-8}\ \Omega^{-1}$. The larger regions are counted as a single hotspot if there is less than a two pixel separation between individual pixels. The larger half-dozen hotspots would be smaller than the image suggests due to tip dilatation effects when imaging small features with a large radius tip.[96]

Due to the nature of the shear force in the creation of hotspots, the actual density underneath the indenter in perpendicular loading is unknown. The conductance criteria of $9 \times 10^{-8}\ \Omega^{-1}$ is quite small compared to the overall value of *G* seen in the indents. Moreover, post indentation conductance scanning at 2 μN shows no hotspots, even at the site of the indent. This is likely due to reformed oxide in the damaged region, in the several minutes that a scan requires.

After the initial Hertzian loading, (blue curve in figure 2.16) the curve transitions to an elastic-plastic behavior. Focusing on the pop-in at $\delta \approx 8$ nm demonstrates a clear correlation between a simultaneous decrease in *G*, and the lateral displacement burst in *P*. At the arrest of the displacement excursion, *G* continues to decrease. Here, $\delta \approx 8.8$ nm, the indenter begins to reload the sample, which means there is a corresponding increase in the contact area. After approximately 1.1 nm of additional indenter displacement, $\delta \approx 9.9$ nm, *G* begins to increase again, but at a reduced rate. The exact state of tip-sample contact is not known during the large pop-in, from $\delta = 8$ to $\delta = 8.8$ nm, as the sample surface deforms. In the past, this excursion likely would have been interpreted as oxide fracture. If this were oxide fracture, an increase in *G* would be expected as the tip begins to reload the surface, seen in the DC example of 2.12, or the LC example of figure 2.13 for the Al/Al_2O_3 film. As the tip-surface contact is loaded, the contact area is increasing, (Eq. 1.21), and with increasing contact diameter, *G* should also be increasing, (Eq. 1.29). The continued decrease in *G* thus requires that some other mechanism be counteracting this increase in contact area. It is proposed here that the mechanism is the multiplication of dislocation loops under the indenter, acting to decrease the conductivity of the sample, as described in Eq. 1.31.

The differences in *G*-δ between Cr films and Al films are evident on initial loading. Where the Al/Al_2O_3 system shows low *G* and then a dramatic turn on coincident with a small displacement excursion, the Cr/Cr_2O_3 system shows a much higher initial *G*, which temporarily decreases, coincident with a displacement excursion. A rise in *G* of orders of magnitude after significant displacement can only indicate that the nature of the contact has changed. In the case of the Al film, the contact has changed from a tunneling contact to that of a contact more indicative of metal-metal, but where the fractional contact area is smaller than that of Pt at the same contact depth. However, the slope of log (*G*) vs displacement in this case is 0.44, in which the contact area is increasing according to the Maxwell model. Any decrease in *G* must be accounted for by other mechanisms. It can be seen that the initial post fracture behavior, between time 7.5 s and 10 s in figure 2.12, in the Al film is quite noisy. This is likely due to intermittent small area contact, whereas in the Cr film (figure 2.16) the contact can only be increasing in

size after the pop-in at 8.8 nm, while *G* decreases. The only variable in equation 1.29 that would decrease *G* in the case of increasing contact area is *an increase in resistivity*. It is proposed that the dramatic turn-on in *G* in Al/Al_2O_3 is evidence of oxide fracture, following the conclusion of Pethica.[61] Moreover, we propose that the downturn in *G* occurring simultaneously with a large displacement excursion in the Cr/Cr_2O_3 system is caused by a high local dislocation density near the contact, enhanced during the excursion, which increases the resistivity of the sample.

2.3.3. Elastic simulations of chromium and aluminum thin films

Theoretical models using parallel springs can be used to model the stresses of thin films on substrates.[97, 98] However, these analytical models can be cumbersome and fail to account for shear stresses. In order to determine the stress, and likelihood of plasticity, in the multilayer films, elastic simulations were used to calculate the von Mises stress in the both sets of films with native oxides.

Elastic simulations were performed using the FilmDoctor program, described in §1.4.4.[28] A load of 215uN, the load of the large pop-in, is chosen for the Cr film, and gives a maximum von Mises stress of 11.0 GPa at a depth of 38.7 nm. This is just below the Cr/MgO interface, figure 2.18.

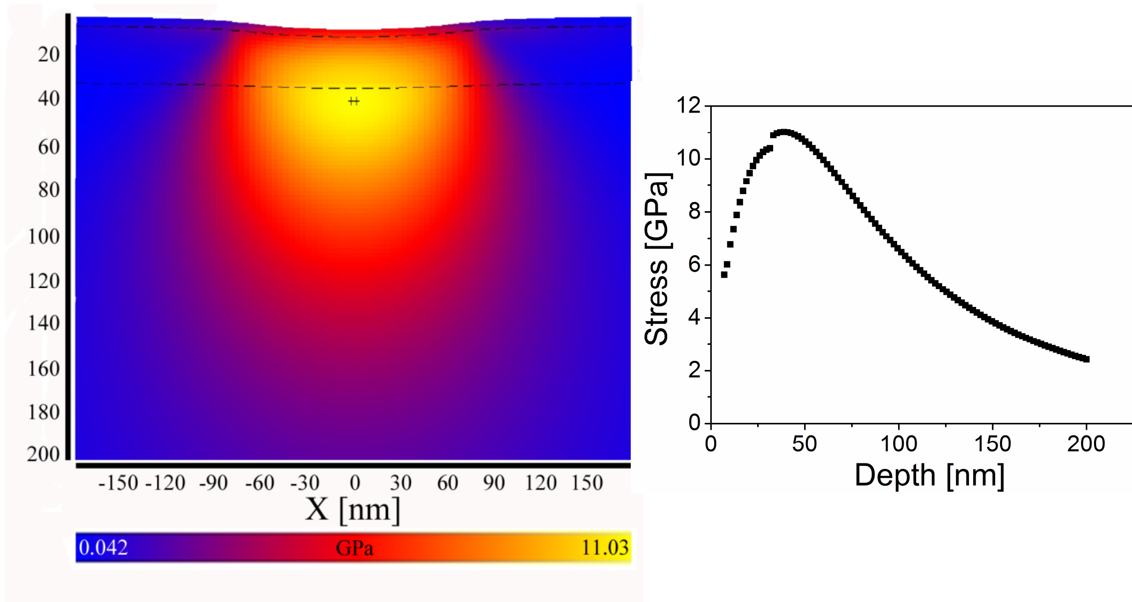

Figure 2.18. Simulation of the von Mises stress via FilmDoctor for the Cr system (color) at a load of 215μN (the load at the time of the large pop-in). Oxide-Metal-Substrate interfaces are indicated by the dashed lines. The The von Mises stress Z cross-section (graph) is indicated in the plot, centered at the left cross-hatch, which indicates the point of maximum von Mises stress as a function of the z direction (bottom)

A value of 10.5 GPa is calculated at the Cr/MgO interface. Literature values for hardness in thin films of Cr are in the 6 to 10 GPa range,[99, 100] quite close to the bulk hardness of MgO at 9.2 GPa. The modulus of Cr, 248 GPa, is less than the indentation modulus of MgO, 295 GPa. In both the film and the substrate, if a Tabor relationship is used, the simulated von Mises stress exceeds the yield stress of the material. However, because of the extremely high electrical resistance in the MgO, the current is flowing only through the metal film. If the substrate were to yield prior to the film, the only electrical change would be an increase in contact area, causing an increase in G. Since the opposite is seen, it is likely that the metal has yielded, and not the MgO substrate.

For the Al system, yield stress in free standing thin films tested in tension have been reported as high as 4 GPa,[36] while indented films ranging from 300 to 500 nm have reported hardness values range from 3 to 6 GPa.[101-104] Here, the hardness of the substrate, 8.8 GPa is higher than the film value. The von Mises stress, figure 2.19,

calculated at 330μN shows a maximum von Mises stress of 5.76 GPa, at the metal film/substrate interface. However, at the edges of the indenter/alumina interface, a value of 5.33 GPa is found. As a ceramic under tensile strains that are not accounted for in the simulation, the alumina is likely to fracture prior to yield.

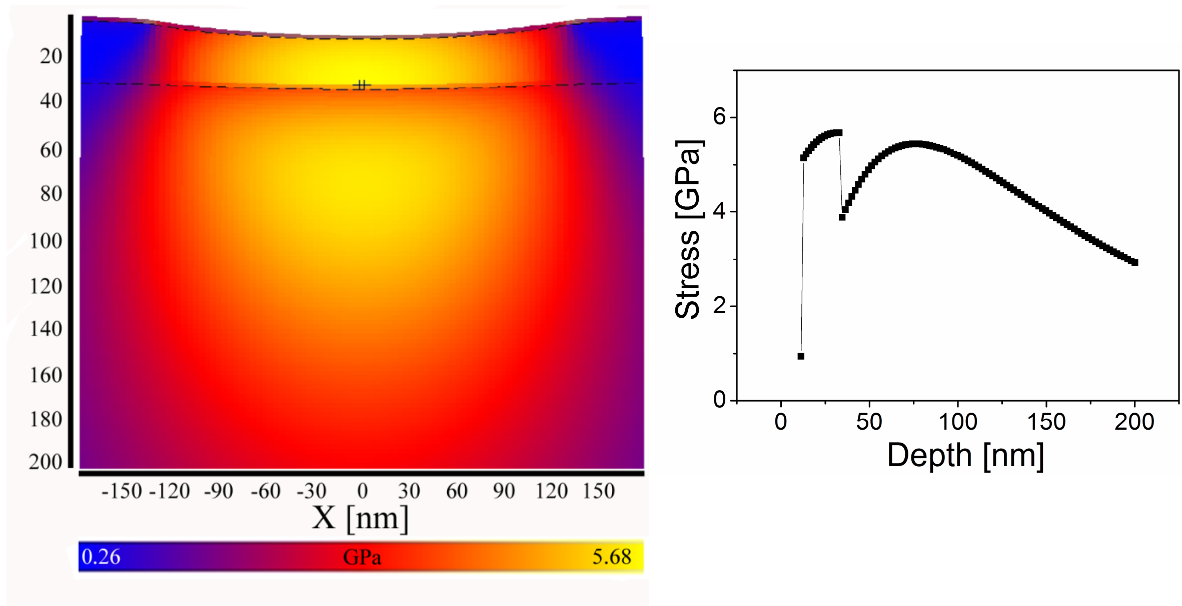

Figure 2.19. Computed von Mises stress via FilmDoctor for the Al system (color) at a load of 330μN (the load at the time failure for figure 2.13). Oxide-Metal-Substrate interfaces are indicated by the dashed lines. The von Mises stress Z cross-section (graph) is indicated in the plot, centered at the left cross-hatch, which indicates the point of maximum von Mises stress as a function of the z direction (bottom)

Additionally, these elasticity simulations assumes that there are no frictional, growth stresses, or surface roughness effects. As Bobji, Gerberich, and Greenwood[49, 105, 106] have all shown, there is considerable stress concentration near the asperities, increasing the likelihood of plasticity in the asperities. Simulating asperity contact with a "large indenter", figure 2.20, with a 2 nm asperity, of wavelength 100 nm, at a load of 130μN, shows a maximum von Mises stress of 11.9 GPa, near the center of the Al film, rapidly decaying in +z.

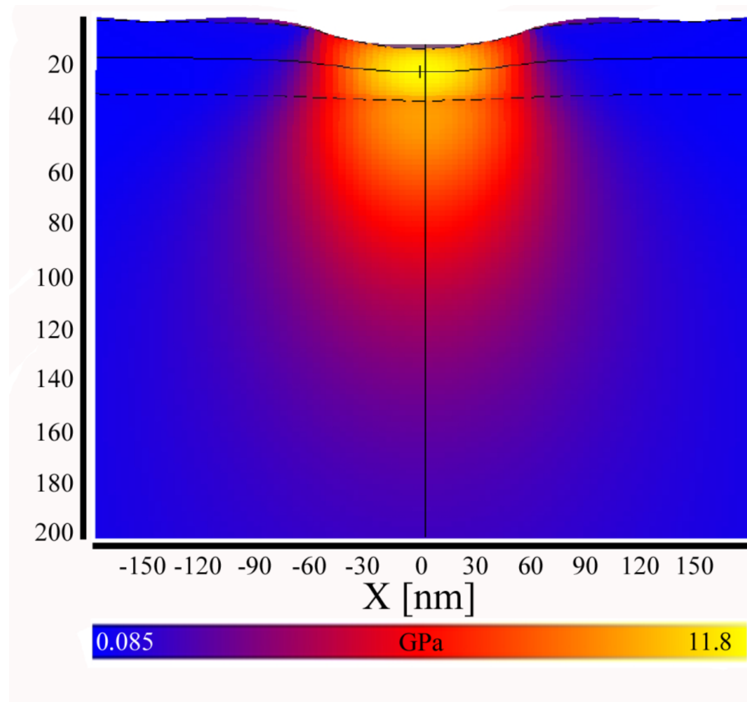

Figure 2.20. Computed von Mises stress via FilmDoctor for a simulated "rough" Al system at a load of 130μN (the load at the first load drop for figure 2.12). Oxide-Metal-Substrate interfaces are indicated by the dashed lines. The maximum von Mises stress is within the metal film, but values of 9.9 GPa are found in the oxide directly under the indenter.

This load was chosen, as it is the load at first load drop, signifying initial yield, for figure 2.12. The von Mises stress is 9.9 GPa directly under the indenter, in the oxide film. From the $G - \delta$ measurements, it can be seen that oxide fracture did not occur at 130μN.

From these simulations, it can be seen that large stresses do occur in the substrates, with the possibility that some of the residual plasticity occurs in the substrate. Importantly, rough surfaces can change the stress distribution, providing possible yield points for the fracture of the oxide in the case of the Al system.

2.3.4. Radial stresses

However, even when taking into account the surface roughness, the lack of frictional effects at the indenter – film interface reduces the tensile stress at the edges of the contact, in turn reducing the shear stress near the surface. Using the "no-slip" condition for indentation radius, *r*, in the region $0 \le r \le a$,[107] Spence has shown that the maximum radial stress can be calculated as

$$\sigma_r(r=a) = 1.515(1-0.16\nu)\eta p_0 \quad , \qquad \text{Eq. 2.15}$$

where μ is the constant coefficient of friction, p_0 is the contact pressure, and η is a factor that characterizes the differences in elastic constants between the indenter and substrate. Here, with a factor of three difference in shear moduli, using table 5.1 from Johnson, η is close to -0.24.[13] Calculating the tensile stress at the edge of the contact for figure 2.19 gives a value of -2.56 GPa. The tensile stress is defined as being negative, keeping the convention of positive compressive stresses in the rest of the thesis. Using a very simple fracture model,

$$K_1 = \left(1.12 - f\left(\frac{a_{crack}}{t_{film}}\right)\right)\|\sigma_r\|\sqrt{\pi a_{crack}} \ , \qquad \text{Eq. 2.16}$$

with an edge crack of length, $a_{crack} = 1$ atomic unit (approximately 0.51 nm), and the function *f* of value 0.44, and a film thickness of 2.2 nm, a fracture toughness greater than $69\ \text{MPa} \cdot \text{m}^{1/2}$ would be required to prevent fracture. This is an order of magnitude greater than the room temperature fracture toughness of single crystal sapphire.[108] It can therefore be concluded that, *i)* the initial estimate of the crack length is likely too large, *ii)* that compressive stresses will prevent crack growth by a crack-closing mechanism under these circumstances, and *iii)* that the fracture of the oxide under strong tensile conditions is likely.

The previous, idealized simulations and calculations do not take into account the stresses which arise during the oxide growth. Oxides typically have an intrinsic stress related to formation by ion diffusion, and by coefficient of thermal expansion mismatch when the oxides are deposited at high temperature. These stresses are maximum at the

metal–metal oxide interface, due to epitaxy, and fall off at the metal oxide – air interface. The simplest means of calculation of these stresses would be the metal to metal volume ratio, (PBR for Pillings – Bedworth Ratio).[109] For Al/Al_2O_3, this ratio is 1.28, and for Cr/Cr_2O_3 is 2.07. Assuming elasticity, the compressive stress in the oxide film can be calculated as;[110]

$$\sigma = \frac{-E_{ox}}{1-\nu_{ox}} \omega \left[\left(\mathrm{PBR} \right)^{1/3} - 1 \right] \quad , \qquad \text{Eq. 2.17}$$

where, E and v, have the usual meanings and ω is the factor for stress reduction mechanisms. Not surprisingly, the factor of ω prohibits rigorous analysis of films. However, typical values of ω are on the order of 0.10. If this value is then used, the compressive stress in the Cr/Cr_2O_3 system would be 4.9 GPa and 1.5 GPa for the Al system. Modifying the metal oxide fracture results of Eq. 2.16 for the Al system, with this stress gives a theoretical fracture toughness of $28\ \mathrm{MPa}\cdot\mathrm{m}^{1/2}$, still not possible to achieve for this system. These stresses, 4.9GPa for the Cr and 1.5GPa for the Al, are likely to exceed the strength of the material, at which point the elasticity model would no longer apply.

2.4. Plastically constrained aluminum films

2.4.1. Experimental considerations

Silicon, with a modulus of ~160 GPa and hardness of approximately 12 GPa, does not provide an ideal substrate for constraining dislocations. To further constrain dislocation plasticity in the aluminum films, an approximately 90 nm layer of primarily amorphous Si_xN_y was deposited on Si (100) substrates by low pressure chemical vapor deposition (LP CVD). Aluminum was then deposited, by RF sputtering, in the conditions given in §2.3.1. Here, the oxide was grown by the presence of pure oxygen at 500 Torr at ambient temperature. Again the films showed a lattice parameter, determined by WAXRD, of 4.05 ± 0.01 Å, essentially relaxed. Films of thickness 13, 43, 70, 110, 210, and 300 nm Al thickness were grown.

To understand the effects of the $Si_xN_y/SiO_2/Si$ substrate system on the mechanical measurements, a hardness and modulus depth profile of the substrate system was performed with a Berkovich tip, and data analyzed with the Oliver and Pharr analysis.[24] Like others,[111] a near surface Young's modulus of approximately 100 GPa was found, rising to 150 GPa for contact depths approaching the film thickness, and the near surface hardness was 21±4 GPa. Therefore, the substrate system should be elastically less constrained than the prior Al on Si sample, but the possibility of plastic deformation in the substrate is significantly reduced, i.e. plastically constrained.

AFM was then used to further characterize the surface roughness and grain size of the films. Grain size, as expected, increased with film thickness, from 63 nm, figure 2.21(a) at a film thickness of 13 nm, to 215 nm for the 300 nm thick film,, figure 2.21(b).

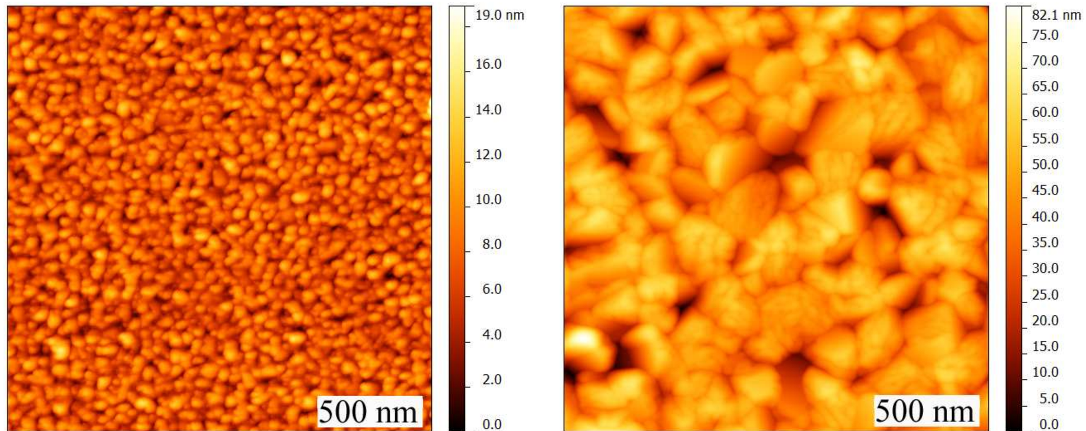

Figure 2.21.(a) A 2μm x 2μm repulsive non-contact SPM scan, of 13 nm $Al2O_3/Al/Si_xN_y/SiO_2/Si$ multilayer film, with rms roughness of 2.08 nm, and grain size of 63 nm. **(b)** Identically sized scan for the 300 nm multilayer film, value for rms roughness and grain size are 10.56 and 215 nm, respectively. Scans courtesy of Palak Ambwani.

Indents were performed with the carbide tips described in §2.2.4, initially using the same technique of spaced indents, with 10 μm spacing. However, for the carbide tips, the indent-to-indent variation was found to be dependent on prior indentation. This indicates that the measurement ability of the instrument degrades with each indent. This is likely an issue with contamination, perhaps a reaction between the fresh Al metal and the carbide tip. For a series of three LC indents to a maximum load of 100μN, with tip

cleaning prior to the first indent, the maximum in G decreases, and δ at fracture increases with each indent, figure 2.22(a,b,c).

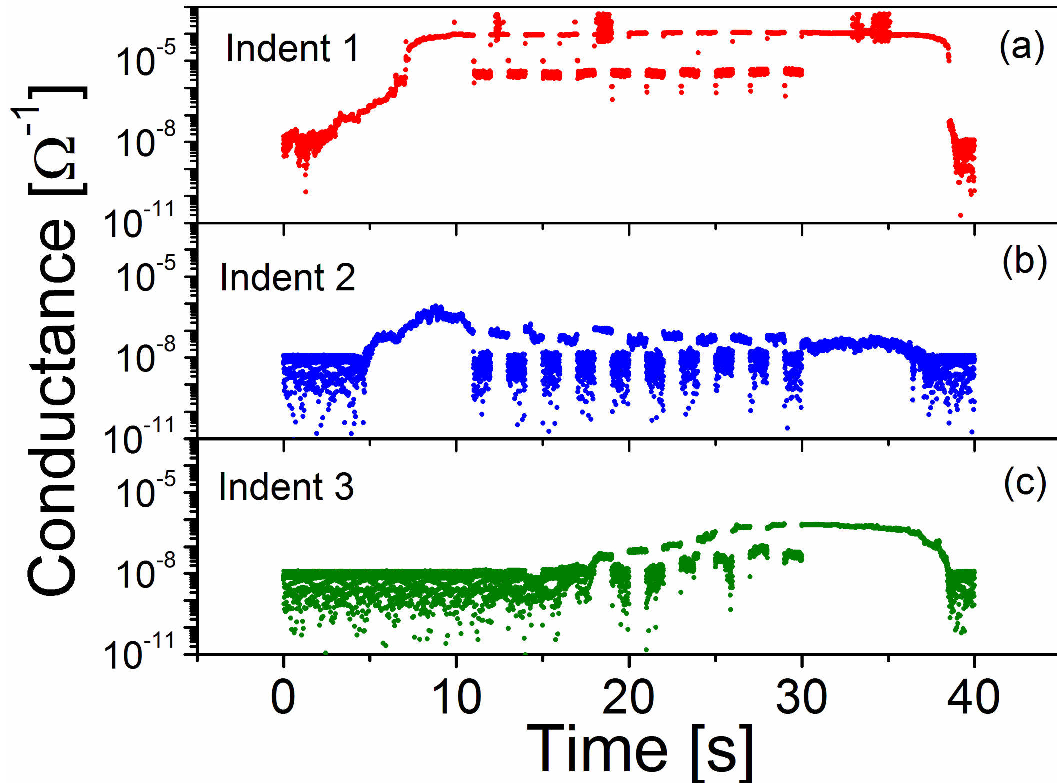

Figure 2.22.(a): G – time for the first 100μN indent into the 70 nm Al2O3/Al/Si_xN_y/SiO_2/Si multilayer film after tip cleaning using a cube corner indenter. Indentation was performed with a 10 s load segment followed by a 20 s hold and 10 s unloading segment. The applied bias was switched off and on during the hold segments to determine quality of the contact. Cleaning was initially done by ultrasonication in deionized water, but was later switched to gentle swiping with a cotton swab wet with acetone. **(b)** second indent, same conditions as (a), but no intermediate cleaning **(c)** third indent, same conditions as (b). Due to the contamination of the tip from previous indents, G decreases for (b) and (c).

Due to this contamination issue, the tip needed to be cleaned after each indent, and then subsequently tested on the Pt reference sample. The bias for these tips was reduced to 10 mV from the 300 mV bias used in the boron doped tips. A sharper tip also means less contact area. Unfortunately, the side effect of continually operating the piezo to come

into contact with the sample is increased thermal drift, making the load – displacement profiles less well developed and possibly affecting the accuracy of the measurement.

2.4.2. Effects of plastic constraint on fracture in Al thin film system

The design of experiments was to vary the Al thickness to observe the relative effect of the plastic constraint on oxide fracture. In the case of the 43 nm thick plastically constrained film, measured as the Al thickness, plasticity is observed at very low load and depths, figure 2.23 (top left), where 3 nm of residual plasticity remains after indentation to less than 8 nm. However, the oxide started to fail only at indentation depths 83% of the film thickness using the zero current crossing as the breakthrough criteria, figure 2.23 (bottom right). The previously mentioned work function difference causes a contact potential in the tip – oxide contact, which results in a negative measured current for low bias voltages. However, when the carbide comes into contact with the Al metal, the current is positive, therefore the zero crossing current is used as the breakthrough criteria. The indentation stress at failure is on the order of 1.2 GPa. The conductance at failure is still quite low, with a maximum conductance of only $4\times10^{-10}\,\Omega^{-1}$, increasing smoothly on loading and decreasing smoothly again on unloading.

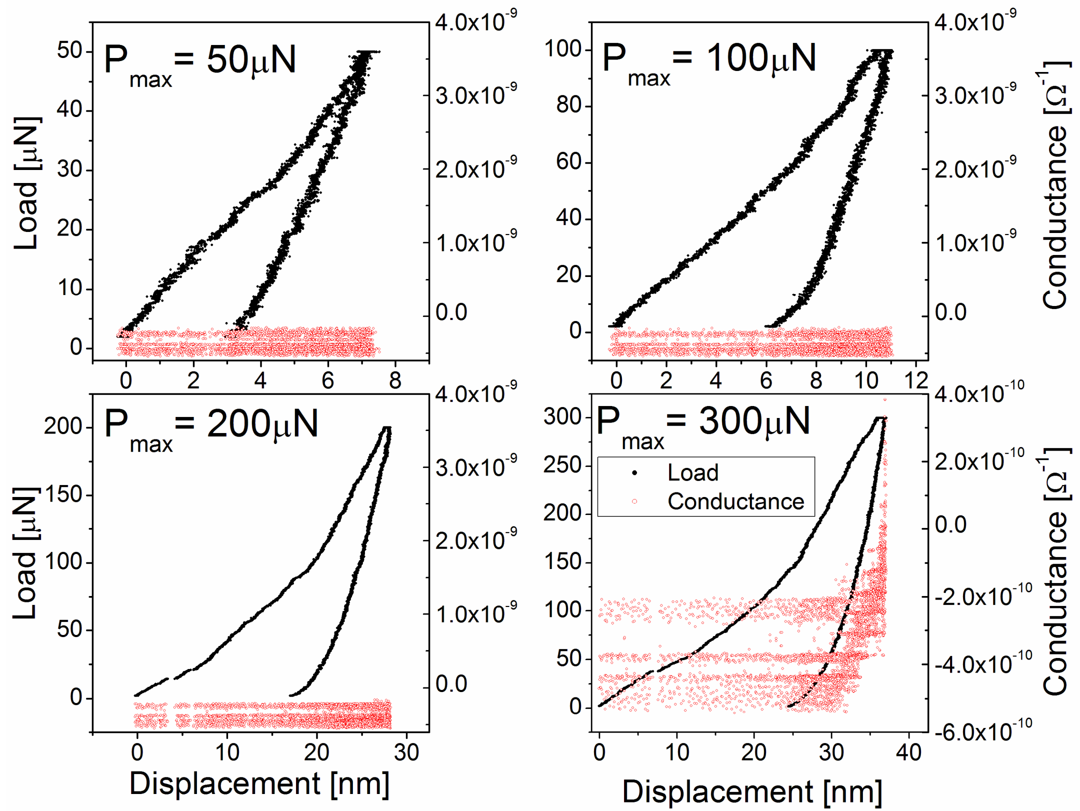

Figure 2.23. A series of indents from 50 to 300 μN on the 43 Al multilayer system. The tip was cleaned and tested on Pt prior to each individual indent. The onset of conductance is seen only in the highest loads, at a depth of 83% of the film thickness. The load-depth variation is due to surface effects on the Berkovich indenter. This variation in topography could possibly play a part in the breakthrough characteristics.

Again, pop-in events are seen, especially evident in the case of the 200μN indent (lower left figure 2.23). Typically, this would be described as fracture of the oxide,[112] but here that is obviously not the case. Similar indentations were performed on films of thickness 13, 70,110, and 300 nm. To determine what affect the film thickness had on constraining oxide fracture, the mean failure depth for a variety of 50, 100, 200, and 300μN indents for all film thicknesses, 13, 43, 70, 110, 210, and 300 nm was plotted, figure 2.24.

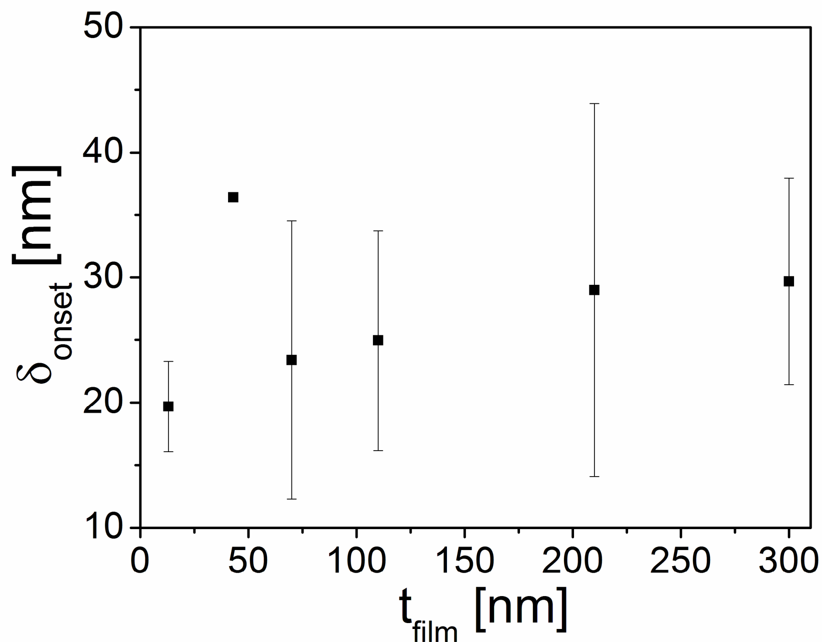

Figure 2.24. The depth of oxide failure, where failure is considered to be the onset of positive conductance, for all six film thicknesses, for LC indents from 50 to 300μN. The large scatter bands may be due to asperity (surface roughness) affects, but occur at all loads.

The failure criterion suggests that, regardless of plastic constraint in the film system, that the failure depth of penetration was approximately constant. There is significant scatter in the data, both in the measured depth at a given load and failure depth, possibly due to surface roughness effects or thermal drift during indentation.

In all likelihood, the athermal stress criteria used for failure here represents only part of the process. Venkataraman found that there was a significant thermal/statistical component in the failure of thicker oxide films.[112] For the thin oxide films under investigation, observation of failure under a variety of conditions, including at pop-in events, during the hold segment, and during the unloading process point to a thermal component in the process. Loading rate experiments were performed, but are inconclusive due to the large scatter in data. See chapter 6, future work, for more information.

Summary

Here, the ECR instrumentation gives insight into the largely elastic deformation of a thin native oxide on thin Cr and Al metal films. This method utilizes *in situ* electrical measurements to determine mechanical changes of metal thin films during nanoindentation. The relatively large current measured at initial loading in the Cr films may indicate an alternate means of electron conduction other than tunneling. This could include pinhole effects, and the presence of metallic CrO_2. The initial thickness was measured by fit to GIXR, and has been verified by angular resolved XPS. From a first-order calculation of elastic compression in multilayers it has been shown that the hardness of the Cr metal is exceeded prior to oxide fracture. Additionally, a transient decrease in conductance is likely due to an increase in dislocation density. This is in contrast to the fracture of the alumina film, showing a dramatic rise in *G* as the oxide fractures. These disparate findings on the responses of natural oxide films under contact are being used to investigate oxide film integrity and subsurface plasticity.

Chapter 3. *In Situ* Indentation Imaging; Transmission Electron Microscopy

3.1. Introduction to *in situ* TEM indentation

As seen in chapters 1 and 2, nanomechanical testing by instrumentated indentation testing (IIT) has become a common technique for the measurement of mechanical properties of nano- and mesoscale volumes. The methods of chapter 2 include the use of *in situ* conductance measurements to determine yielding. Chapter 3 begins a focus on *in situ* transmission electron microscopy indentation; this can be seen in figure 3.1, where a pillar under indentation can be observed by a number of beam methods. This is in contrast to *ex situ* observations of residual indentation impressions, again by an array of available methods. Here, the observations of the sample are made by electrons in the transmission mode.

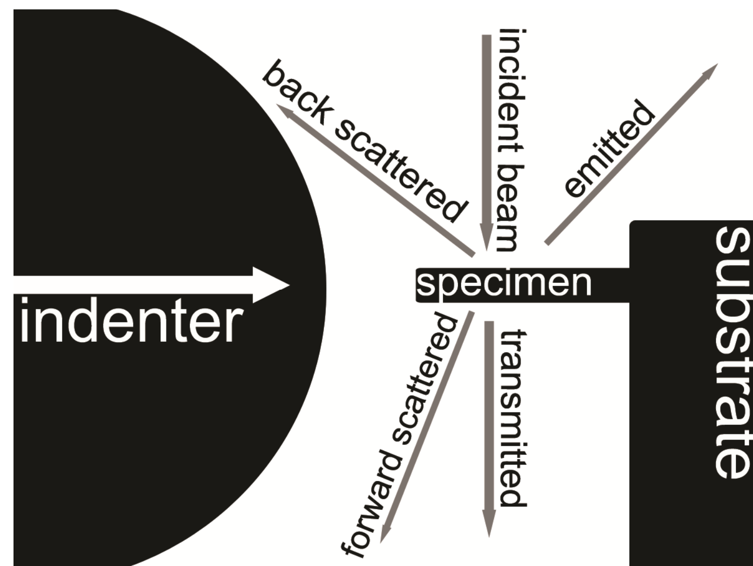

3.1. Schematic of cantilever under observation using a beam of photons, electrons, or neutrons to interact with the specimens, which are then subsequently detected.

The limitations of *in situ* TEM IIT include constraints on instrumentation, sample size, sample preparation, and increased difficulty of analysis. The sample requirements will be discussed in detail, as well as a review of current best practices for sample mounting and preparation. A short section on instrumentation requirements is followed by another on TEM image analysis, with a list of resources, which should be treated only as a very basic introduction to the subject. The limitations on the physical instrumentation

were succinctly summarized in Marks *et al*,[113] and therefore will not be further discussed. The advantages of using *in situ* TEM IIT compared to *ex situ* methods will then be discussed.

3.2. Historical background

In situ instrumentated indentation (IIT) experiments in the scanning electron microscope (SEM) by Gane and Bowden showed that loads as low as 2μN could be applied. Simultaneously, information crucial to understanding the deformation (depth of penetration, and contact radius) can be observed.[114] Follow up work by Gane included the first use of contact probes inside a transmission electron microscope (TEM).[115] Developments in the field of scanning tunneling microscopy (STM) led to *in situ* experiments regarding the role of mechanical contacts in conductance.[116, 117] The use of actuated piezo-driven diamond indenters at the National Center for Electron Microscopy (NCEM) led to the rapid development of the technique.[118-121] Replacing the piezo drive with a depth-sensing transducer and displacement control feedback [52] has increased sensitivity, while the continued device miniaturization and commercialization allows experiments to be run almost routinely in the TEM.

3.3. Sample constraints

The major constraint on samples is size. As the advantage of this technique is to probe mechanics at the nanoscale, this constraint is mentioned only because samples must then be prepared as acceptable TEM specimens. This requires that the samples be electron transparent, that the sample and mount fit within the confines of the microscope pole piece, that the path to the beam is not blocked by specimen mounting or the indenter tip, and that a suitably stiff substrate is used to confine the deformation to the sample.

As the atomic mass of a sample, *Z*, increases, the thickness of the sample must decrease to maintain electron transparency. For aluminum in a 100kV microscope the maximum thickness for transmission is approximately 1μm, while a gold sample in the

same microscope necessitates a sample thickness of less than 100 nm.[122] These thickness maxima are only for electron transparency. For the observation and determination of specific deformation mechanisms, such as slip plane and Burgers vector in the TEM, the best sample is often the thinnest sample.[123] Increasing the accelerating voltage of the microscope will allow for an increase in the specimen thickness, but can also result in the beam damaging the specimen.[123, 124]

The specimen and indenter probe must also be able to drain electrical charge, or a build-up of static charge will cause the beam to drift. For non-conducting specimens, this is remedied by coating the sample with a very thin (1 to 2 nm) layer of amorphous carbon. Any breaks in the circuit, such as a nonconductive bonding layer, can be fixed by the use of carbon paint.

Typically, the indenter is placed to indent perpendicular to the direction of the beam, parallel to the direction of the holder. As the z-axis has historically been taken as the axis of indentation, and to avoid confusion, the beam axis of the microscope shall be referred to as the y-axis. Therefore, both the x (transverse) axis and the z (indentation) axis lie perpendicular to the beam.

Several of the classic TEM specimen preparation techniques have been used successfully, such as tripod polishing,[125, 126] jet polishing, and focused ion beam (FIB) polishing.[127, 128] These, and additional techniques, are further explained in several texts.[123, 129] However, all traditional methods require some adaptation for attaching the sample to a holder/mounting so as to have surfaces available for compression. For example, a traditional wedge polished specimen is typically placed on a TEM ring, and is supported only by bonding agent, shown in figure 3.2(a). For indentation, the same specimen must be bonded such that the ring does not interfere with the indenter, and that the sample load frame remains stiff, as in figure 3.2(b).

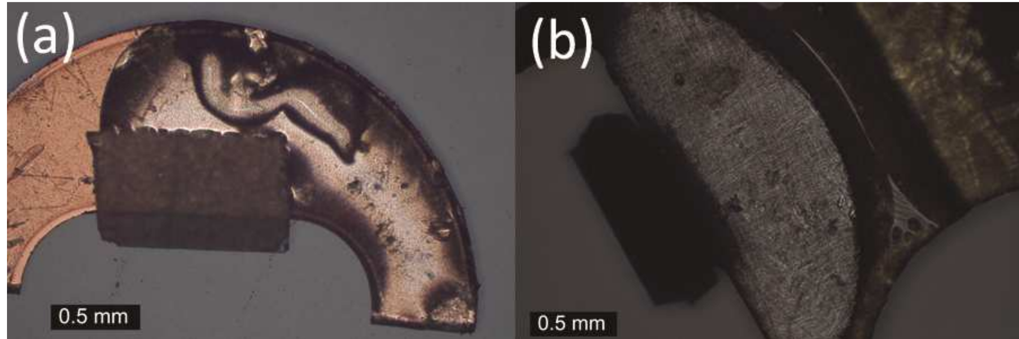

3.2.(a) Image of TEM FEI mount "half-ring" with tripod polished olivine sample discussed in chapter 6 mounted. Here, bonding agent was M-Bond. **(b)** Image of FEI mount "half-ring" style sample mounted to chair. Sample is a (111) silicon substrate with vapor-liquid solid grown silicon towers courtesy of Krylyuk and Davydov at NIST, discussed further in chapter 4. Crystal bond was used to adhere half-ring to sample mount.

The use of a jet-milled single crystal Ni sample, subsequently attached to a brass substrate, is detailed in the supplementary materials of,[130] where the sample is then further milled using FIB. For any type of thinning, if the aspect ratio of the thinned section sample is too large, such as the FIB milled Al specimen discussed in,[120] elastic bending of the crystal may result. The consequences of bending will be discussed in the final section on image analysis. The use of the FIB to prepare specimens has become common for *in situ* experiments.[130-134] However, the FIB creates a thin damage layer, which can change the mechanical behavior of the test material.[135, 136] The use of the FIB for sample preparation should be used with some caution.

Two unique specimen mounting techniques that satisfy the requirements listed above are the use of wet etched silicon wedge/plateaus, and the use of sharp wedges. Using lithography and etch techniques developed for MEMS systems,[137] many wedges can be produced on (100) single crystal Si wafer. These wedges extend in the z-direction, and have a flat plateau, on the order of 1μm in length (Figure 3.3a,b).

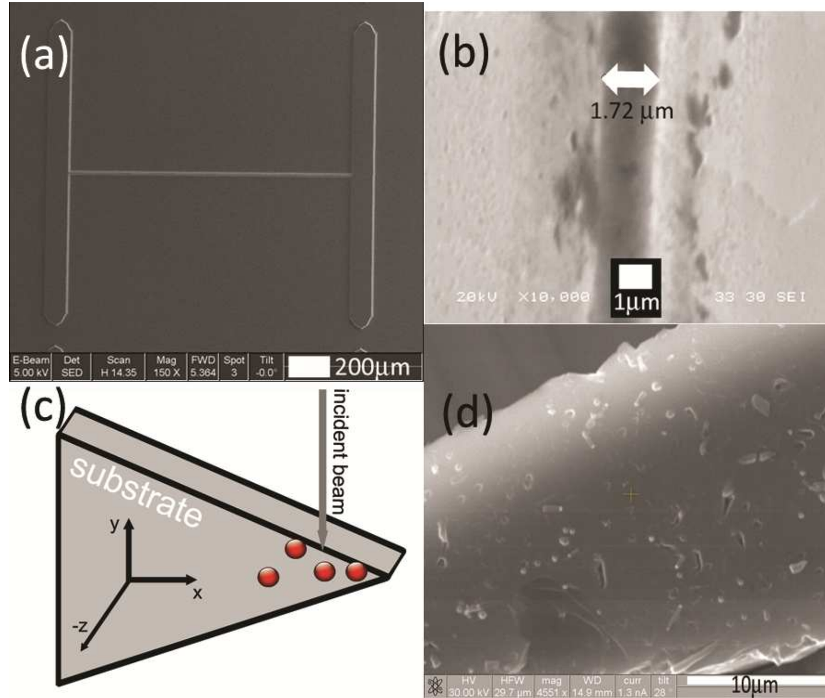

3.3.(a) Low magnification SEM micrograph of a silicon wedge-plateau etched from a silicon wafer using photolithography. Hundreds of such wedge-plateaus can be produced from a single wafer. The large bars on the "H-shape" aid in optical alignment of the plateau, which makes up the center line in the "H". Image courtesy of Hysitron, Inc. **(b)** Higher magnification SEM micrograph of a plateau which is 1.7µm is width. Image courtesy of Hysitron, Inc. **(c)** Cartoon representation of a sapphire wedge, with beam direction indicated. The indenter would be approaching from –z direction to compress the spheres against the substrate. **(d)** SEM of wedge sample, showing (111) Si pillars that have fallen, as well as white dots where pillars are upright. Pillar samples are courtesy of Swiss Laboratories for Mechanics of Materials and Nanostructures (EMPA), in Thun, Switzerland. Wedge shown is a silicon substrate used for growing the pillars. A sapphire wedge would provide a less compliant substrate material, ideal for studying stiffer materials.

Thin films, such as Al in [120, 138], Al-Mg alloys,[139] or nanoporous Au,[140] can then be grown, processed, imaged, and indented on these plateaus. Additionally the mechanical properties of the Si wedges can also be tested.[141] A major advantage of the wedge plateau technique is that many experiments can be performed along the length of the wedge, allowing statistical generation of properties, and for many polycrystalline films a

variation in grain orientation with respect to the beam. When testing along plateaus, experimenters should be aware that the lack of constraint in the y direction can affect the measured mechanical properties.[142] Additionally, there is a well-known substrate effect in indentation.[101, 143, 144] Although the effects of the substrate will affect indentation measurements the goal is, as much as possible, to restrict the deformation to that of the material under test. This requires a high modulus/high hardness substrate. For example, a problem was encountered in,[145] where the increased hardness of silicon nanoparticles compared to bulk single crystal plastically deforms the silicon plateau substrate when compressed by the diamond indenter. To avoid that, the silicon is replaced by a sapphire wedge, which is sharp in the x-y plane (to avoid the substrate shadowing the beam) (Figure. 3.3c, d).

It should be noted that any material used in the sample preparation should be vacuum compatible for UHV, or it will contaminate the microscope. After mounting, it is a good practice to insert the mounted specimen and holder in a plasma cleaner, or hold under vacuum to pump off any contamination.

3.4. Instrument constraints

A typical *in situ* indenter has coarse and fine positioning to bring the tip into contact with the sample at the desired position. In the case of the instrument, figure 3.4, a mechanical course positioning system utilizing thumb screws allows for gross adjustments and alignments. The fine positioning system is actuated by a 3-dimensional piezo system with stepped movements to provide both micro- and nanometer level positioning.

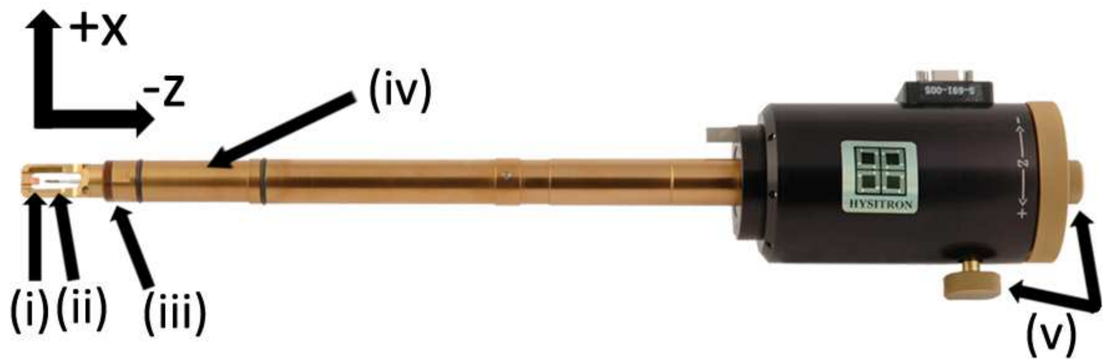

Figure 3.4. A photograph of the Hysitron P-95 PicoIndenter. Axis indicate x and –z direction, whereas the beam (+y) direction is coincident with the viewers perspective. Labels indicate relevant parts of the system; (i) sample mount, (ii) indenter tip, (iii) transducer (hidden by shielding), (iv) piezo manipulator (hidden by shielding), and (v) course mechanical manipulators for x and z movement. The y manipulator is hidden from view.

Operation in vacuum places additional demands on the transducer. Using a harmonic solution, the tip can be modeled as being damped by the capacitive plates.[146] The tip damping is then separated from the damping provided by the material when in contact to measure properties of the material. However, for *ex situ* indentation, the presence of air also provides significant damping. To prevent parasitic oscillation, which is enhanced by vacuum, a high-bandwidth transducer with a high mechanical quality factor must be used.[113]

3.5. Microscope/Indenter operation

Once the sample and holder have been inserted into the microscope, and the microscope is operational, a coarse examination of the sample at low magnification (typically 2500x) with a parallel beam is used to find the area of interest. This area of interest is brought into eucentric focus, and the microscope is aligned according to manufacturer recommendations. The tip is brought in with the coarse positioning system, while keeping the tip in view to avoid crashing the tip into the specimen. The x-z positioning while viewing in 2-D is relatively easy. To bring the tip to the sample in the y

direction, use the defocus to alternately focus on the sample and tip, using finer adjustments until the tip and sample are both in the eucentric focus plane, figure 3.5.

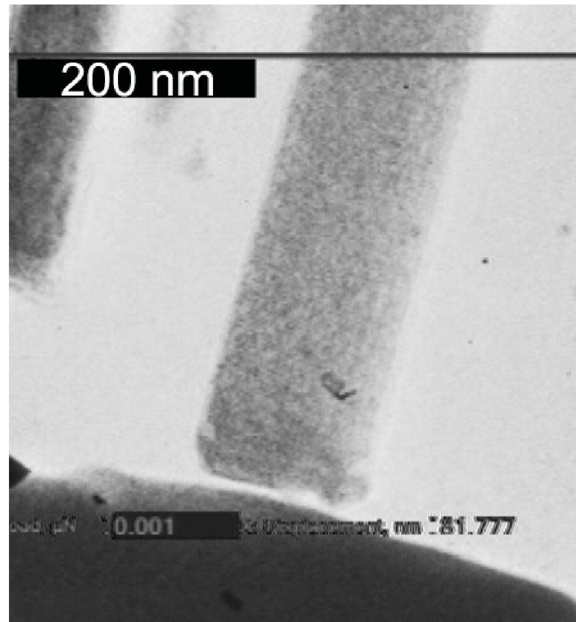

Figure 3.5. A video screen capture taken during compression of a (111) Si pillar approximately 170 nm in diameter. Both the pillar and the tip are in focus, so compression should occur on axis with the pillar.

Obtaining useful images in the TEM takes practice. There are two primary contrast mechanisms, mass-thickness and diffraction contrast, and two primary imaging conditions, bright field, BF, where the incident beam is used for imaging, and dark field, DF, where a diffracted beam is used. Mass thickness contrast is caused by increased scattering from heavier atoms, and/or thicker samples. In this way it is possible to image large gradients in atomic concentration, or variations in thickness. Although all samples will have mass thickness contrast, it is not really useful here. As indentation is a deformation technique, the emphasis is on the imaging of crystal defects. Defects cause diffraction, and therefore the contrast mechanism of interest here is diffraction contrast. Setting up a strong diffraction condition is a requirement for contrast in the image.

It is recommended to use convergent beam electron diffraction, aligning to a zone axis, and then tilting to obtain a two-beam condition. The best two-beam conditions are obtained by using tilts in both α (rotation around z) and β (rotation around x). However,

due to restrictions on sample movement, it is often difficult to tilt in β, although external β tilt control has been reported.[120] A more thorough procedure can be found as a multimedia presentation [147] as well as in introductory texts. [123, 148]

The use of computerized stages allows the set up of multiple two-beam conditions, which can then be switched to obtain the best contrast. In addition to two-beam imaging, the direct beam can be excluded and a diffracted beam can be selected for dark field imaging. DF can highlight grain growth and grain orientation in *in situ* IIT, [139, 149] as well as to highlight dislocation activity. As a reminder, it is critical to record the diffraction pattern, and which spots were used to obtain the image, in order to understand the scattering conditions in the sample.

While not strictly necessary, *in situ* TEM indentation is aided by the addition of a video capture system, which can then be linked to real time data during indentation. Direct correlation is one of the distinct advantages of *in situ* indentation; however, in some cases the use of a more standard image capture system allows for higher resolution images. The video capture system used for the experiments in this thesis runs at NTSC standard (29.97 frames per second / 720 x 480 resolution), using a usb TV capture card. An additional device links the control computer to the video capture, allowing simultaneous output of load-displacement data that is time locked to the video images.

3.6. Analysis

In analyzing *in situ* TEM micrographs and videos, it is important to remember how the image was formed (by interaction of electrons with the sample). This is the reason that all images should be associated with a diffraction pattern. Aside from introductory texts,[123, 148] an excellent text for understanding how defects in samples form images and how to identify them is Head, et al.[150] Some further illustrations are given in chapter 4.

The observation of defects can be obscured by sample bending, as was mentioned in the section on sample preparation. This bending of the crystal planes causes diffraction and interference patterns that are then observed as contrast, figure 3.6, where large aspect

ratio Si pillars can be seen bending in a video frame during *in situ* compression with IIT. This elastic bending contrast can be mistaken as defects, if the user is not careful. However an accumulation of defects can also cause permanent bending of the crystal. This will be further discussed in chapter 4, dealing with dislocation velocities.

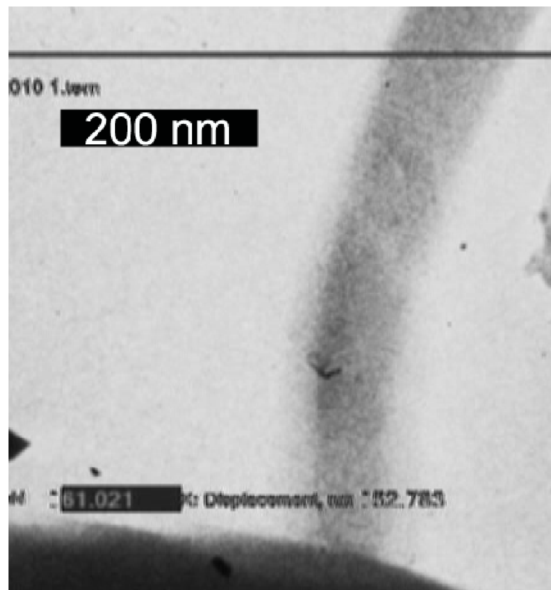

Figure 3.6. A video screen capture taken during compression of a (111) Si pillar approximately 120 nm in diameter. The large aspect ratio and slightly misaligned indenter result in large bending. This pillar fractured soon after this image. Bend contours are visible as dark regions.

It should also be noted that, much like Schrödinger's cat, the act of viewing can and does change the object of viewing. In this case the effect of the beam on the sample can increase dislocation velocities, and enhance nucleation.[151] The beam effect must be considered when doing *in situ* analysis.

3.7. Advantages over conventional indentation

In situ IIT has four particular advantages over conventional IIT. The first, and most compelling advantage gained is the unique insight into deformation mechanisms,

such as plasticity, phase change, and grain rotation. This is the reason that many users find it necessary to perform *in situ* IIT experiments.

In addition to this primary advantage, the authors feel that three other advantages for testing nanostructures stand out;

1. *Requirement of an area function for the indenter*. The Oliver-Pharr area function is presented as a logical solution to the requirement for an area function for traditional nanoindentation.[24] However, with the ability to use either a flat punch in the compression of pillars or spheres, and an axis symmetric indenter in the indentation of films to low contact depths, the projected and contact diameters can be directly measured to within a precision of a few nanometers.

2. *The ability to position the indenter over the exact specimen location*. While many commercially available systems have a scanning feature image, where the tip (or an AFM attachment) can raster the surface to find an area suitable for indentation, this is not a good option when using a flat punch indenter. Scanning is also problematic when a sample contains high aspect ratio features which are easily damaged. Additionally, a sample of nanoparticles, weakly adhered by van der Waals forces may slide across the substrate. Imaging features also allow an identification of pre-existing defect structures, and defective features can then be passed over.

3. *Direct correlation of the force-displacement data with the TEM video image*. Minor et al. demonstrated that irreversible damage to the sample may occur under stresses that are near the force detection limits of the *in situ* indentation device (<200nN). Here, figure 3.7, small asperity contact was visible in the microscope, resulting in dislocations being nucleated and gliding in the sample.[152]

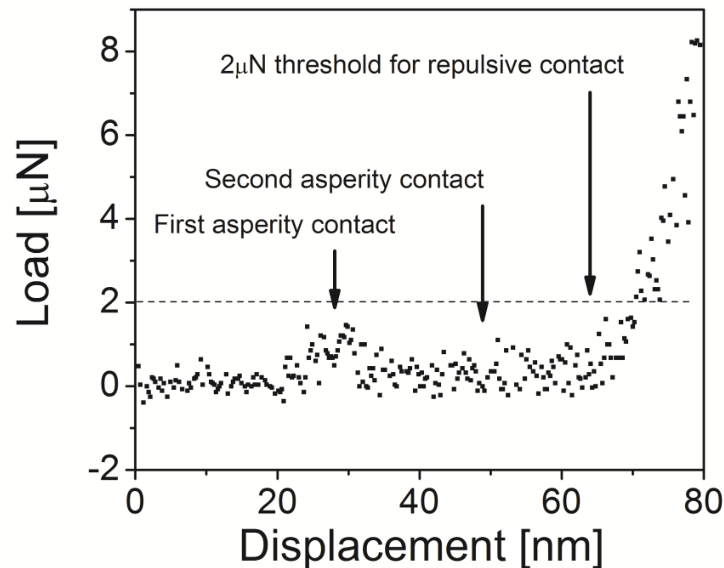

Figure 3.7. Load displacement data showing very small indications that contact has been initiated. Dislocations were obvious in the video micrographs. Adapted from Minor, et al.[152]

This occurred prior to the establishment of a large repulsive contact during the test. This phenomenon would have been lost in traditional IIT, but can be captured and understood quantitatively here.

3.8. Summary

By coupling the high resolution imaging capabilities of the TEM with the quantitative force-displacement data provided by *in situ* TEM nanomechanical test instrumentation, insight into material deformation processes occurring during the indentation test can be resolved. The availability of user friendly and commercial devices avoids the complexities of instrument design for the user, who can now routinely perform experiments that are not possible with standard ex situ IIT instrumentation.

Chapter 4. Plasticity in nanoscale silicon

4.1. Introduction: Dislocation dynamics in high temperature silicon

Dislocations play an important role in determining the electrical and mechanical properties of crystalline silicon. Recent findings regarding room temperature plasticity in silicon will play a key role in how MEMS, NEMS, sensors, and microelectronic systems are designed for reliability. For example, next-generation bipolar devices using silicon nanowires as building blocks[153] require stable electrical properties. However, it has been shown that the I-V characteristic of these "wires" is heavily influenced by the presence of dislocations.[154-156] Zakhorov, et al, found that, by increasing the dislocation density by an order of magnitude, the bias voltage for a 10 pA current decreased by an order of magnitude.[156] For devices to function properly, it is necessary to understand their electrical characteristics *as implemented* in the device including variation in defect densities.

Materials science and engineering textbooks generally treat broad classes of materials with properties that are appropriately connected to their bonding type. Ceramics and many semiconductors, with ionic and covalent bonding, are generally described as brittle but with high hardness. Metals, in their pure state with metallic bonding, and polymers with covalent bonding and van der Waals forces have high ductility and toughness but low hardness. The differences in ductility and toughness are generally attributed to the relative mobility of dislocations in the crystalline materials. Ease of dislocation motion in metals is due to a low Peierls (energy) barrier for moving the dislocation from one lattice row, x_1 to the next, x_2, figure 4.1.

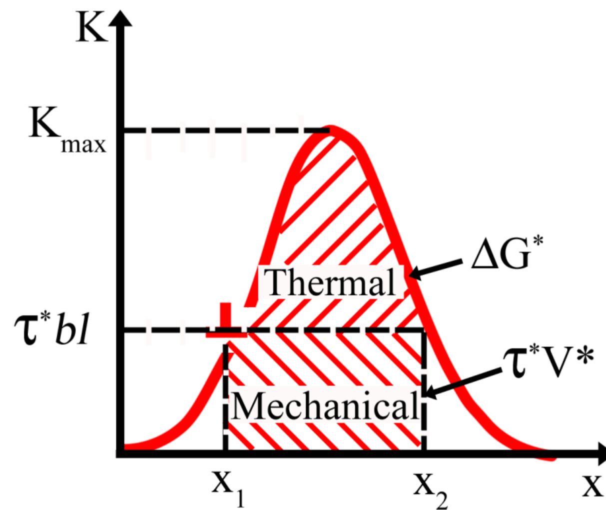

Figure 4.1. The energy barrier, K, approximated by a sinusoidal function can be overcome by a combination of thermal and mechanical energy on the dislocation, allowing it to move through the crystal. Adapted from Hull and Bacon.[157]

From figure 4.1, it can be seen that dislocations will more easily overcome this barrier with either an increase in thermal energy or increased stress. By plotting the velocity at a given stress to the inverse temperature, figure 4.2, which have an Arrhenius relation, the energy barrier can be determined. For silicon at temperatures varying from 900 to 1100 K,[158] this energy is 2.2 eV, whereas for metals, it is typically on the order of 0.1 to 0.8 eV.[159] While, for a variety ceramics and semiconductors, these barriers, measured at elevated temperatures, are found to be 1.0 to 2.4 eV.[160] For any thermally activated mechanism, including dislocation motion, this increase represents orders of magnitude decrease in the velocity, represented in figure 4.2. The thermal process determines the ductile to brittle transition temperature (DBTT), below which materials become brittle.

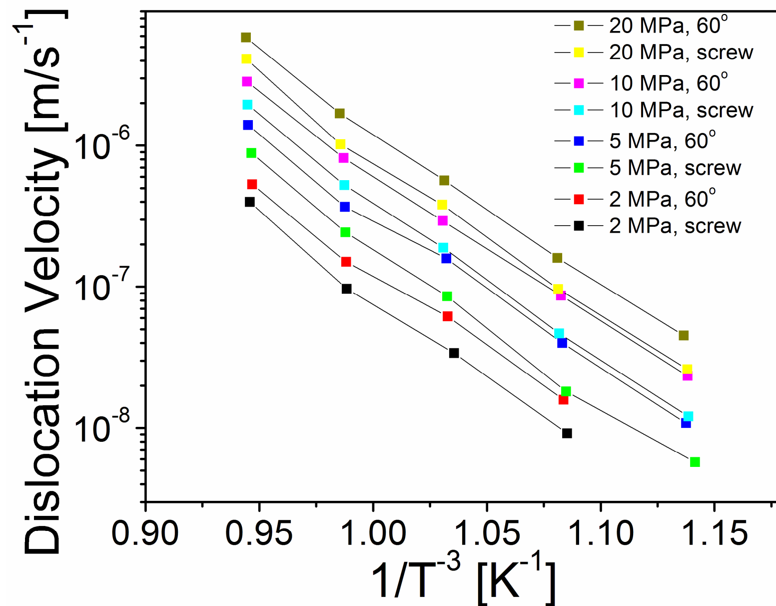

Figure 4.2. The dependence of the dislocation velocity on both temperature and stress, as inferred from figure 4.1, measured by X-ray tomography in high purity single crystal silicon at high temperatures. Adapted from Imai and Sumino.[158]

For many metals, this DBTT is below room temperature, while for most ceramics, the DBTT is several hundred °C, or larger. Hence, the ability of dislocations to act in crack-tip shielding[161, 162] or blunting[163] to reduce the propensity of unstable cracking, and thus increase toughness, is large in metals and alloys compared to ceramics and semiconductors at room temperature. The DBTT, investigated by four-point bend after precracking with Vickers indentation in single crystal silicon, figure 4.3, reveals a sharp transition between brittle failure, indicated by fracture without presence of dislocations (4.3 left inset), and ductile behavior at 540°C, where there is a relatively high dislocation density (4.3 right inset).

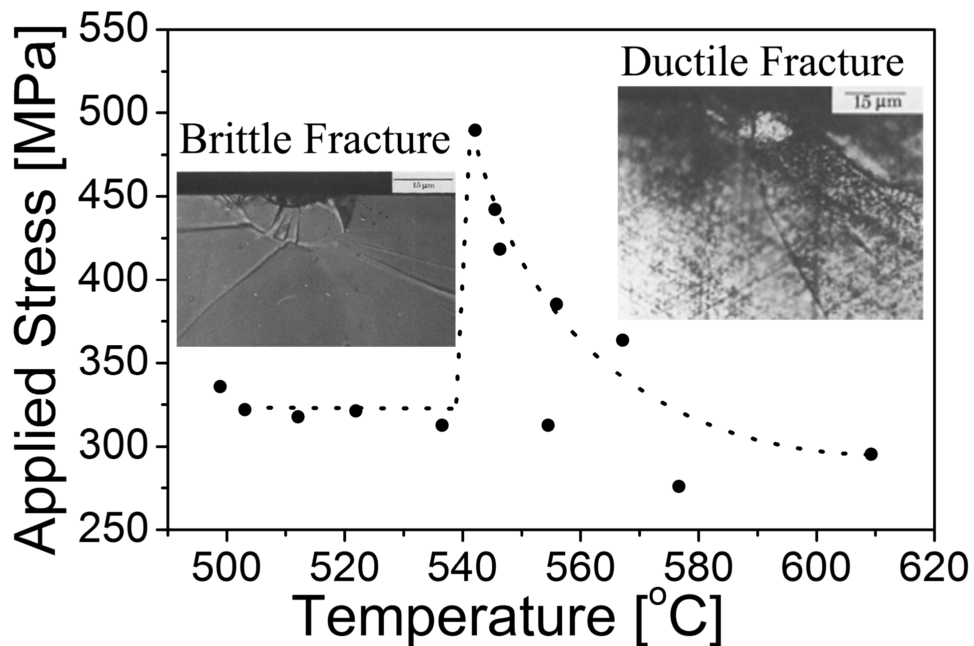

Figure 4.3. Stress, applied by four-point bend after pre-cracking with Vickers indentation, on single crystal silicon at increasing temperatures shows a sharp transition, in both terms of applied stress at failure, and post-deformation morphology. Adapted from Samuels and Roberts.[164]

4.1.1. Defining dislocations in silicon

Prior to understanding the mechanisms of ductile deformation, it is important to outline the structure and likely types of dislocations. At standard temperature and pressure, silicon has the diamond cubic (DC) structure, as does diamond. The DC structure is an interpenetrating face-centered cubic (FCC) lattice with a two atom basis. This second set of atoms is offset from the first, by $c/4[111]$ where c is the unit cell width. The stacking pattern of the DC is typically given the notation, $A\alpha B\beta C\gamma$, compared to the ABC stacking of FCC. Again, like FCC dislocations in the DC are typically found on the $\{111\}$ plane, with a direction of $\langle 0\bar{1}1 \rangle$, however they can appear as dislocations on the equivalent αB or $B\beta$ stacking, figure 4.3. Respectively, these are the glide and shuffle sets.[165]

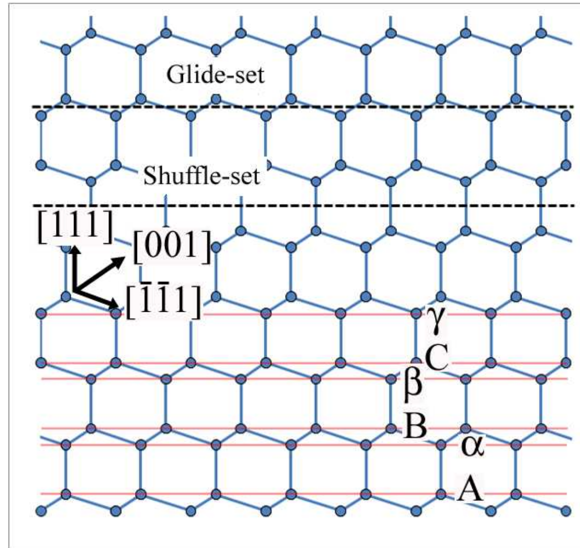

Figure 4.4. A projection of the diamond cubic structure on the $(1\bar{1}0)$ plane, showing stacking sequence, the shuffle, and the glide planes. Adapted from Hale,[166] Hull[165] and Wang, et al. [167]

Dislocations on the glide plane are usually of either 60° or screw character, where 60° indicates the angle between the Burger's vector and the line direction of the dislocation, ***u***. There is an energetic competition between the two sets of dislocations, with the glide set perhaps being preferred in bulk, high temperature samples.[160, 168, 169] The glide set also allows dissociation into partial dislocations, where the dislocation energy, proportional to b^2, can be reduced by the splitting of the dislocation into partials. This is governed by the Frank criteria,[157] and may be preferred under high pressure compression.[170-172] Dislocations as prismatic loops can also be formed by punching out a dislocation in the $[111]$ direction, and must also be considered. These loops are often seen near oxygenated defects in single crystal silicon grown by the Czochralski method.[173]

Calculating the Schmid factor for compression in the $[\bar{1}1\bar{1}]$ direction using

$$m = \cos\phi\cos\lambda \quad , \qquad \text{Eq. 4.1}$$

assuming $\{111\}\langle 0\bar{1}1\rangle$ slip gives a value of 0.272. It should be noted that the dislocation movement, here at low temperatures, is governed by the glide (Peierls barrier) process not the climb process, which requires the diffusion of vacancies to the dislocation. This diffusive process is applicable only to higher temperatures.

With the high Peierls energy in covalent materials, the movement of dislocations is hindered. The low energy configuration are straight dislocations in the $\langle 0\bar{1}1 \rangle$ in the $\{111\}$ glide plane. When available energy for movement is introduced, either as thermal energy or applied stress, figure 4.1, a small segment of the dislocation line can move forward one atomic step, to the next low energy valley. However, this segment is connected to the rest of the dislocation line by small segments not in the low energy configuration. These connecting segments are called kinks, and are elastically strained. In a bulk sample, where the dislocation line must be continuous, these kinks must occur in pairs, and therefore the energy to move a dislocation forward requires the formation of two kinks. However, in materials with large surface area to volume, where the dislocation can thread to the amorphous boundary of the oxide layer, single kink formation is possible.[174, 175] This is important, as the energy required for single kink formation is less than that for the double kink mechanism.

It should be stated that there is significant controversy over the preferred dislocation, glide or shuffle, in silicon. Both modes have been observed at varying conditions of temperature and pressure.[167, 170-172, 176, 177] Ideally, knowing the dislocation type would add evidence to the correct theory.

4.2. A ductile to brittle size transition?

Recently, there has been an abundance of literature, by the Gerberich group[134, 178-180] and others,[181-183] who have found an exception to the brittleness rule for single crystal silicon nano-scale spheres,[178, 179] wires,[181, 182] and pillars.[134, 180, 183] Such evaluations have included both tension and compression in $\langle 111 \rangle$ and $\langle 100 \rangle$ orientated wires and pillars, and random orientations for spheres. Large increases in ductility and fracture toughness have been reported.[178, 184] The fact that the above increases were measured at room temperature is significant since the DBTT has dropped 250° compared to bulk silicon.[180, 184, 185] Theoretically, this can be explained by the single kink barrier, mentioned above. Additionally, for dislocations which have split into partials, the leading partial has been shown to move at higher velocities than the trailing partial.[186] For small length scales,

with dislocations which may thread to the surface, there may no need for the trailing partial to move, in turn enhancing the dislocation velocity.

4.3. Silicon nanopillars

Nanopillars of silicon, grown under two processing conditions were tested, primarily under "open-loop" (no feedback) control in the *in situ* instrument described in chapter 3. The first sets of nanopillars to be tested were through collaboration with Dr. V. Sivakov, Max Planck Institute of Microstructure Physics, Germany, and Drs. B. Mook and J. Michler, Laboratory of Mechanics of Materials and Microstructures (EMPA), Swiss Laboratories for Material Testing and Research, Switzerland. These pillars were typically 200-300 nm in diameter, with a typical aspect ratio of 3 or 4:1, figure 4.5. These pillars were grown by a vapor-liquid-solid (VLS) mechanism.[187] Here, a thin film of Au is deposited on a silicon substrate and annealed whereupon Au droplets coalesce from the film. Then a Si vapor source is introduced, in this case by electron beam evaporation (EBE), above the Au-Si eutectic temperature (373°C). The Si vapor diffuses through the Au droplet to the underlying Si substrate, precipitates and grows as a single crystal in the preferred crystal direction (here $\left[1\bar{1}1\right]$). These pillars contain a considerable amount of Au doping within the pillar near the surface, as determined by aberration corrected scanning transmission electron microscopy (STEM) can be as high of 10^{20} cm^{-3}.[188] A more typical value, measured by atom probe tomography, is on the order of 10^{16} cm^{-3}.[189] However, the exact concentration is related to the processing temperature (eutectic growth), which affects the electrical and mechanical properties. Additionally, shoulders appear on several pillars, indicative of Ostwald ripening of the Au during the VLS growth.

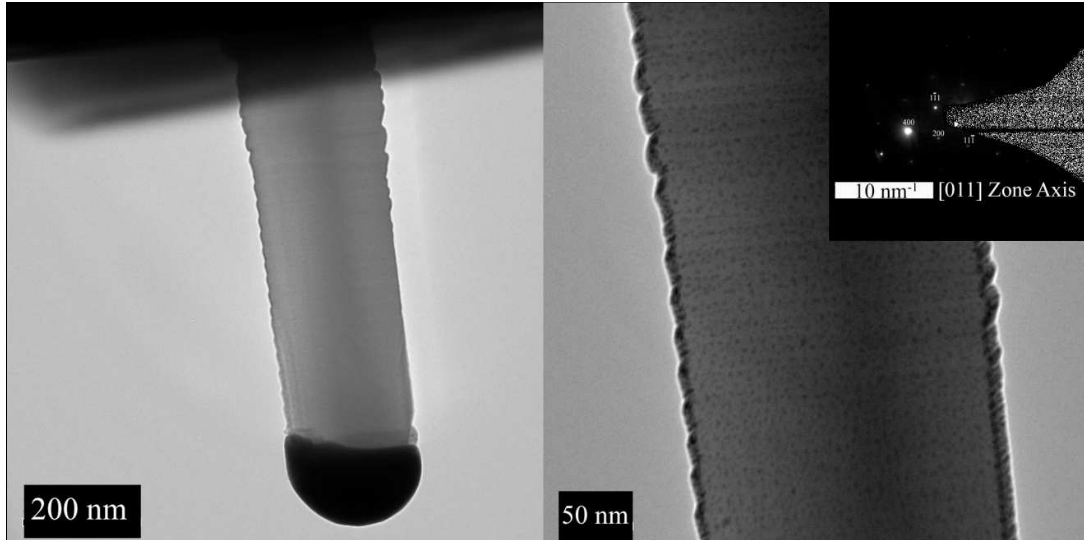

Figure 4.5.(a) Bright field TEM micrograph of a typical EBE-VLS grown nanopillar, inset; the corresponding diffraction pattern. **(b)** Higher magnification of the same pillar, Au dopant can be seen as black dots.

In addition to the EBE grown pillars, chemical vapor deposition (CVD) pillars grown by Dr. Sergei Krylyuk of Dr. Albert Davydov's group at NIST Metallurgy, Maryland) were tested, figure 4.6.

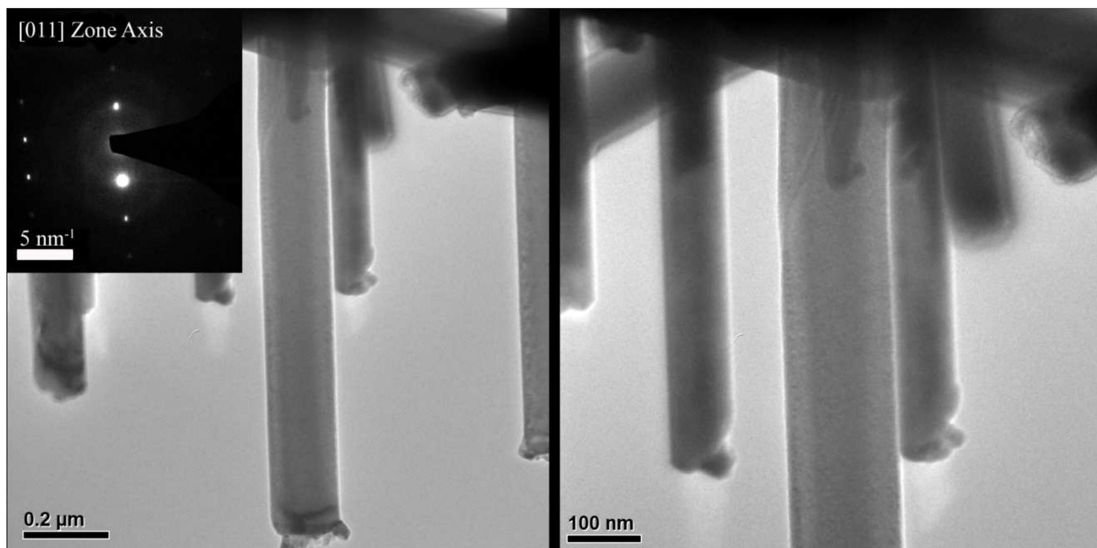

Figure 4.6.(a) Bright field TEM micrograph of a typical CVD-VLS grown nanopillar, inset; the corresponding diffraction pattern. **(b)** Higher magnification of the same pillar, showing defect.

Here, 100 nm Au nanoparticles were used as the growth catalyst in these pillars. as opposed to the previous annealed Au film. Gaseous Si in the form of $SiCl_4$ gas was combined with H_2 and N_2 at 600 torr. p-Si(111) substrates were functionalized by poly-L-lysine. A deposition temperature of 850°C gave a growth rate of 200 nm/min. To prevent post-growth diffusion of the Au catalyst, the samples were force cooled at 550°C by transference to the reactor cold zone. These pillars, figure 4.6(a), had a slightly larger variation in diameter (100 to 200 nm), with lengths of 600 nm to 1.3 μm, giving aspect ratios as high as 10:1. These pillars did not have Au caps as tested, the Au having been etched off using a diluted HF (1:10) rinse, followed by deionized water, and a commercial KI/I etchant (Transene, TFA). This etching process primarily replaces the Au solute near the surface with vacancies, while removing the Au cap. To clarify the type of pillar being discussed, they will be referred by growth technique. The first group of pillars will be referred to as EBE, and the NIST pillars as CVD, in reference to growth technique.

4.4. Compression of silicon pillars

The EBE samples were tested, using the tip-sample alignment procedure of chapter 3, using an open-loop (no feedback) condition. Initially, compression to a max load of 250μN during a 10 s loading period was targeted, figure 4.7. This flattened the Au cap, which showed several discrete displacement bursts (pop-ins). Due to the no-feedback condition, the target max load was not reached. Here, even though the pillar is seen to be elastically compressed, the modulus on loading is obscured because of the yielding of the Au cap.

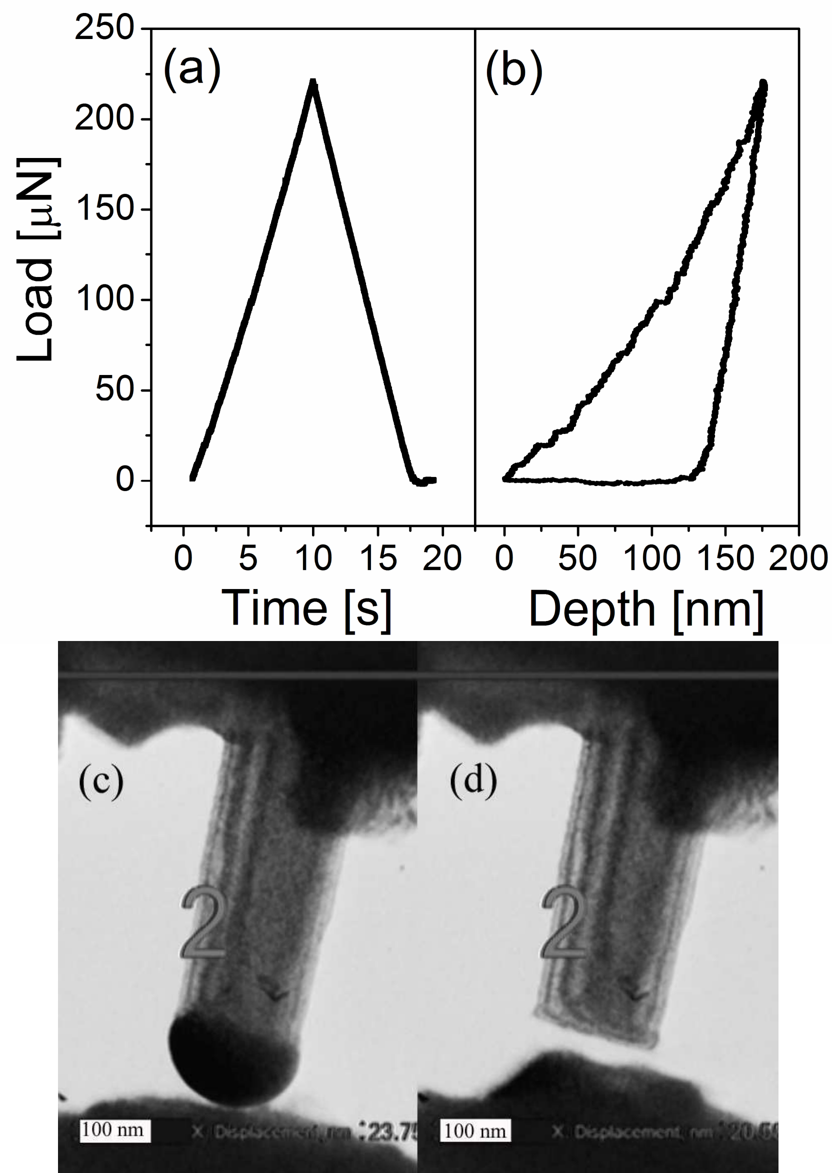

Figure 4.7. (a) Typical load – time plot for the EBE pillars, loading and unloading segments of 10s, with no hold. **(b)** Load – depth for the same indent, showing discrete displacement bursts as the Au cap is compressed. **(c)** Video screen capture of the 200 nm pillar, approximately 620 nm in length, immediately prior to first compression, and **(d)** immediately prior to the second compression, where the Au cap has stuck to the indenter.

4.4.1. Young's Modulus for both sets of pillars

Assuming the Au cap to have no reverse plasticity, the Young's modulus was measured on unloading. The elastic modulus for the pillars was determined from,

$$E = \frac{\Delta\sigma_{true}}{\Delta\varepsilon_{true}} \quad , \qquad \text{Eq. 4.2}$$

where $\Delta\sigma_{true}$ is the true stress,

$$\Delta\sigma_{true} = \frac{P}{A}\left(1+\frac{\delta}{L}\right) \quad , \qquad \text{Eq. 4.3}$$

and $\Delta\varepsilon_{true}$ is the true strain

$$\Delta\varepsilon = \ln\left(1+\frac{\delta}{L}\right) \quad . \qquad \text{Eq. 4.4}$$

For the 200 nm diameter pillar, figure 4.7, with a 4:1 aspect ratio, the modulus was to be 107 GPa, approximately 50 GPa less than bulk Si in the $[111]$. This pillar could be loaded repeatedly, allowing an accumulation of measurements. Repeat compressions of several of the EBE pillars, of diameters 180 to 280 nm, show no relationship between pillar diameter and modulus, and have values of 121±16 GPa.

However, this method involves several major assumptions. First, the substrate is assumed to be a rigid platen. The second is that the Au cap does not contribute to the elastic deformation, and third, that there is no bending. For the first assumption, it is understood that the compliance in the substrate can contribute to the overall elastic deformation. Therefore, it is more appropriate to use the true stress and true strain with the Sneddon correction for micropillar compression, where the compliance in the substrate is calculated as a flat punch indenting an elastic half-space,[190, 191]

$$C_{sub} = \frac{\sqrt{\pi}\left(1-\nu^2\right)}{2E_{sub}\sqrt{A_p}} \qquad \text{Eq. 4.5}$$

from which the stiffness of the system, S, can then be separated from the stiffness of the pillar, S_{pillar}, by,

$$S_{pillar} = \frac{1}{\left(C_{sub} - \frac{1}{S}\right)} \quad . \qquad \text{Eq. 4.6}$$

As the projected area of the base of the pillar, A_p, is four times larger due to the presence of a growth fillet, the compliance of the substrate was observed to have a negligible effect in these pillars, as was also found by Greer, et al.[132] It is worth mentioning again that true stress and true strain were measured during unloading, as the indents were primarily elastic except for the initial contact region on loading.

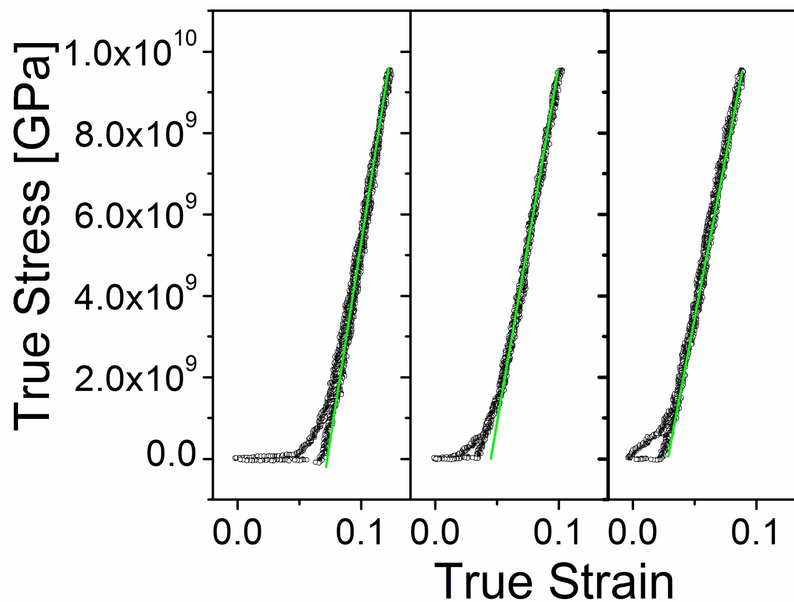

Figure 4.8. Three consecutive indents on a 200 nm tower, figure 4.7(c,d), show that after the Au cap is compressed, that both the true stress-true strain are nearly identical on loading and unloading. The slope of the true stress-true strain, in green, can then be used to compute the modulus. The low modulus is likely due to a combination of elasticity in the Au cap and bending effects.

An average modulus of 121 GPa would be a low value for (111) silicon, requiring investigation of the second and third assumptions. While the stiffness fits, as seen in figure 4.8, appear straight, there is indeed some evidence of bending as can be seen in the video capture of the indentation, discussed later. For stiffness measurements, where the displacement is typically 50 nm, even a 5 or 10 nm deflection would influence the results.

Additionally, the presence of the Au cap is troubling. A simple calculation, using a reduced modulus for uniaxial compression, for 160 GPa Si and 80 GPa Au, gives a value of 53 GPa.

The CVD pillars have much larger aspect ratios, and therefore showed bending in most load – depth curves. However, these pillars, without a Au cap, give values of 129 ± 31 GPa. Therefore, while the effect of substrate compliance is negligible, and effect of the Au cap must be considered, it is likely that the pillar flexure most affects the modulus measurements.

4.4.2. Bending in pillars

During the calculations of the modulus in §4.4.1, measurements in which bending was observed in the shape of the pillar, or where the indenter slid on the pillar, were discarded. With two of the EBE pillars having close to 4:1 (length to diameter) aspect ratio, there is a possibility of buckling. This was found to be the case particularly when the indenter (rounded sphere of ~500 nm radius of curvature) was not properly aligned, and a shearing load was applied. The influence of buckling, even in these lower aspect ratio pillars, will become important when the dislocation velocities are calculated. For the CVD pillars, the 6:1 or greater aspect ratios indicated some bending in nearly all cases.

These 3:1 and 4:1 aspect ratios, thus far defined as length to diameter, must be redefined for buckling analysis. Euler and inelastic buckling for pillars in compression for pillars in compression uses a length to radius of gyration aspect ratio. As the radius of these circular pillars is constant, that gives an "Euler" ratio of 6:1 or 8:1. As the base of the pillar is physically bonded to the substrate, it can be regarded as fixed. This indicates that the pillar angle of the bend, where it meets the substrate, is 90°. This doubles the effective length of the pillar, making the ratio of the 200 nm pillar described above, 12:1. Using the classic Euler buckling formulas for a slender pillar,[33]

$$\sigma_B = \frac{P_B}{A} = \frac{\pi^2 E}{\left(L/r\right)^2} \qquad \text{Eq. 4.7}$$

a buckling load, P_B, of 276μN is found using the known dimensions and the 129 GPa modulus found previously. The buckling load is the load at which deflection from the normal should begin, and an underestimation of the modulus could easily affect this calculation. For several *P-δ* curves for this pillar, buckling was apparent near the end of the compression, at loads of ~220μN.

Following the discussion of §4.5, it will become apparent , that even for linear loading and unloading, such as illustrated in figure 4.8, that that the pillars were bending, determined by analysis of the *in situ* video.

4.5. Dislocation velocities, part I

It should be first made clear that the initial observation and analysis of dislocation velocities *in this section* is flawed. It is included as a lead-in point for improved measurements of the dislocation velocities, later in the chapter. During the compression of the EBE pillars, dark bands were observed, moving mainly from near the tip, progressing towards the substrate, figure 4.9. These bands then moved in the opposite directing during the unloading. It was thought that these were diffraction bands, created by the stress field of a dislocation.

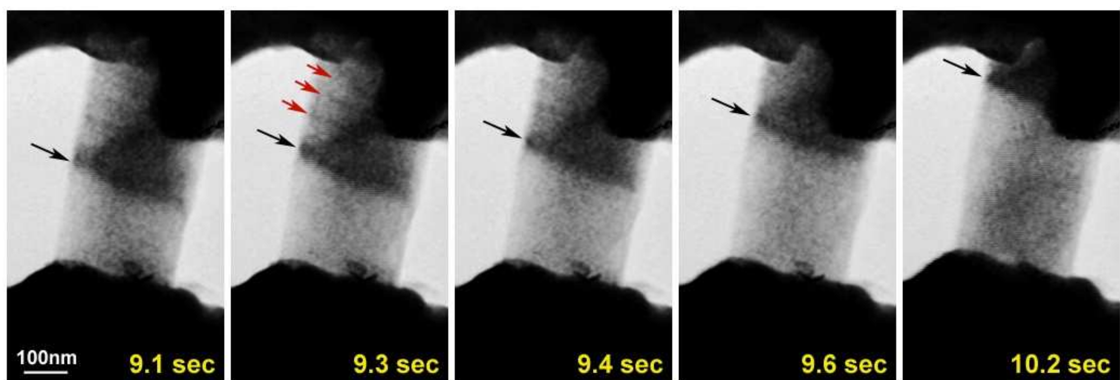

Figure 4.9. Diffraction bands seen during loading, indicated by the arrows in a 265 nm diameter pillar. These bands then propagate down the pillar as loading increases. No residual plasticity is apparent in the pillar after compression.

The velocity of these bands was measured as a function of applied stress and pillar diameter. Values of 80 to 100 nm/s were found, comparable to those found by Imai at 600°C in bulk silicon.[158] The reverse movement was thought to be reverse plasticity from pile-up against the stacking faults seen near the base of many of the VLS pillars. This reverse plasticity can be modeled as an Eshelby pile-up against a grain boundary, such that the stress on the first dislocation, σ^*, from the applied stress, σ, and the other N dislocations, can be found as [192]

$$\sigma^* = N\sigma \quad . \qquad \text{Eq. 4.8}$$

When the applied load is removed, this back stress pushes the dislocations away from the pile-up, such that equilibrium between the Peierls barrier and the back stress is achieved. This stress also serves as a mechanism to turn off the source of dislocation, surface or otherwise, also by stress balance. Given that the theoretical conditions for nucleation are sufficient and can be experimentally observed in spheres, these observations were not totally unexpected.

Here, the first bands appeared at a compressive stress of 1.6 GPa. Using the Schmidt factor, calculated from Eq. 4.1, the average resolved shear stress for the two available dislocation glide sets was $\tau = \sigma \cos\varphi \cos\lambda = 435 \text{ MPa}$. Dislocation slip appeared to be coincident with the nucleation sites being the observable surface roughness along the length of the pillar. This roughness would act as stress concentration points, such that, an effective stress concentration of $k_T = 1.5$ can be expected.[193] The progression of these bands, was that they climbed the column at a constant angle, atypical of a $\{111\}\left[1\bar{1}0\right]$ slip. However, previous observation of dislocations in silicon show that Lüder's band formation is possible.[194] Classical Lüder's bands, demonstrated over 150 years ago, had a yield band that initiated on one side of the sample and zigzagged across the pillar as the band progressed along the samples length.[195] This is depicted in figure 4.10. Given that the initial nucleation stress for silicon was 435 MPa, it would seem that some additional stress would be required to nucleate the site on the opposing side.

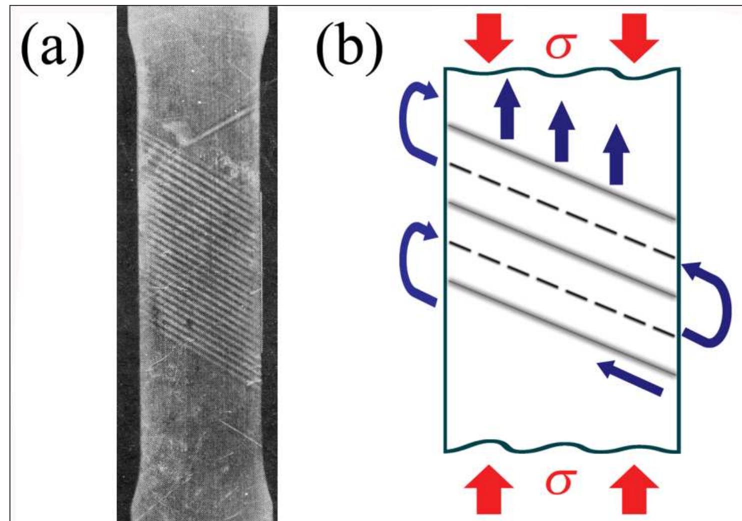

Figure 4.10.(a) A classic Luder's band formed in polycrystalline Al. Adapted from Nadai.[195] **(b)** Schematic representation of the back and forth flow of dislocations in Luder's band progression. Red arrows indicate compressive force, while the blue-black arrows indicate the dislocation motion.

Using the Eshelby pile-up model of equation 4.3, as few as three dislocations could provide an adequate stress to trigger the nucleation site on the opposing side. The back stress would then develop, turning off the nucleation source on the first slip plane and allowing the next nucleation site to be initiated. Although the exact process and number of dislocations was unknown, the velocity of the vertically rising diffraction band associated with dislocations, v_B, depends on the translational velocity of the dislocations on the slip bands.[196] This would require that the velocities of dislocations on a slip band to be nearly an order of magnitude faster than the velocity of the diffraction band. While "metal-like" ductile behavior has been observed, these dislocations would be traveling at velocities on par with Si at 800°C. Also, very little plasticity remained in the pillars, mostly appearing on the $(1\bar{1}1)$, perpendicular to the growth direction.

These inconsistencies were more apparent when comparing to other *in situ* results, where shear banding and/or large scale plasticity were the norm.[130, 152, 197] After discussions with several microscopists, it became apparent that the beam/sample interaction was not as simple as initially believed. In some cases, bending was easily

observed, §4.4.2 and figure 3.6. Unfortunately, bending was not always this obvious. For bending in the microscope Y-direction only, the pillar would not appear curved. Coupled to this, the Y-axis is the most difficult to align for *in situ* experiments. To understand how this type of bending can be observed, a short digression is necessary.

As electrons pass through the sample, there is forward scattering of the electrons from the crystal planes. This forward scattering, figure 3.1, creates the phase-contrast image in conventional TEM. Bragg diffracted electrons also give rise to the diffraction pattern. These diffracted electrons, interacting with the crystal planes, also create diffraction contours, as seen in §4.4.2. The incoherently scattered electrons, with interactions increasing with atomic z and sample thickness, create mass-thickness contrast. Coherently scattered electrons also create contrast differences. In the simplified two-beam approximation, the intensity, I, of the diffracted beam can be described as,[123, 198]

$$I_g = |\phi_g|^2 = \left(\frac{\pi t}{\xi_g}\right)\frac{\sin^2(\pi t s_{eff})}{(\pi t s_{eff})^2}, \qquad s_{eff} = \sqrt{s^2 + \frac{1}{\xi_g^2}} \qquad \text{Eqs. 4.9, 4.10}$$

where t is the distance traveled by the beam, ξ_g, is the extinction distance for the material in question, and s_{eff}, is the effective excitation error. Therefore, as the beam passes through the material, the phase and intensity changes as t changes. For samples with variation in thickness, this gives rise to fringes associated with the intensity of the diffracted beam, as in the pillar in figure 4.11. Bending of the pillar changes the angle of the sample plane, causing a shift in the Bragg diffraction. As these diffracted beams interact, both with each other and the direct beam, an interference pattern is created. This interference pattern is a pair-wise function, initially centered on the bending apex, figure 4.12.

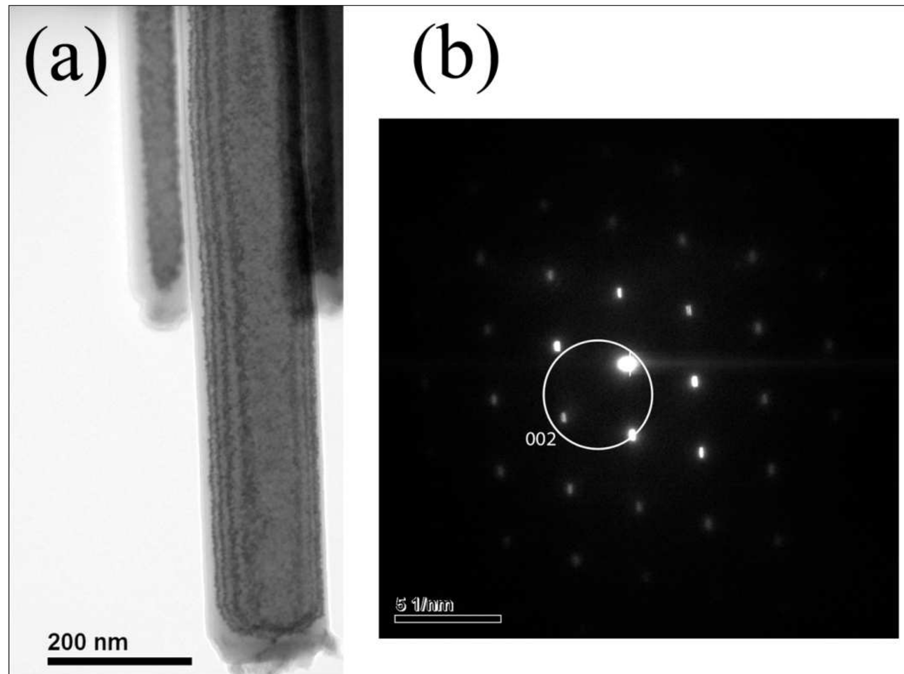

Figure 4.11.(a) A CVD pillar imaged using the direct and the (002) beam. The variations in the intensity are thickness fringes, due to variation in *t*. **(b)** Diffraction pattern for (a), where the white circle indicates the location of the objective aperture.

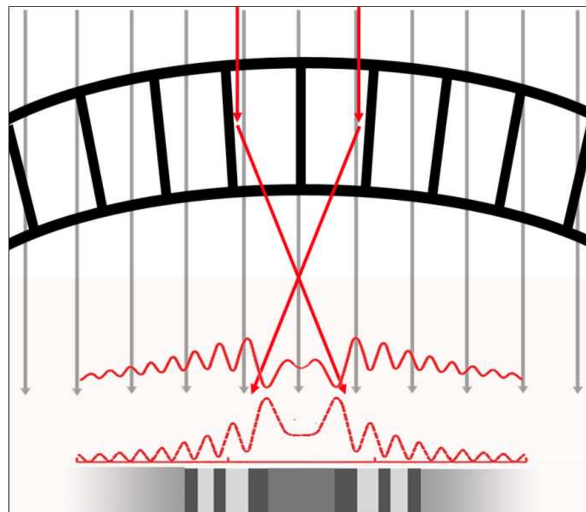

Figure 4.12. Bending of the sample causes diffraction from the bent planes. The interference pattern from the bending is superimposed with that intensity profile from the direct beam. The result is a pair-wise intensity profile that moves under increased flexure. Adapted from Edington, Stach, Howie, and Whelan.[199-201]

Defects also bend the crystal planes, usually such that the planes are bent away from the Bragg condition, which causes a sharp drop in the intensity profile, figure 4.13.

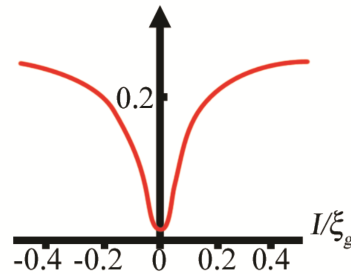

Figure 4.13. Computed bright field intensity profile of a screw dislocation in the center of a thin sample of uniform thickness, $t = 8\xi_g$, with the excitation error, $s_{eff} = \frac{1}{\xi_g}$, and the dot product of the Burger's vector and the diffracted beam, $g \bullet b$, set to 1. The contrast is a sharp function, without fringes. Adapted from Howie and Whelan.[201]

For observation of compressed pillars pair-wise functions exhibiting broad bands are most likely due to bending. These pair-wise contours were observed in almost all cases in the EBE pillars, despite having aspect ratios as low as 3:1. This means that any pillar that contained a moving dislocation would be seen as a summation of the intensity from both the defect, figure 4.13, as well as the bending contour. In addition, if the planes surrounding the dislocation were also bending, it could appear that the dislocation contour was moving very rapidly when, in fact, it may remain stationary. This can be seen in a video sequence for a 180 nm CVD pillar, which after several compressions, has been plastically deformed. Here, the prior damage to the pillar appears to move very rapidly down the length of the pillar, pressing up against some barrier, figure 4.14.

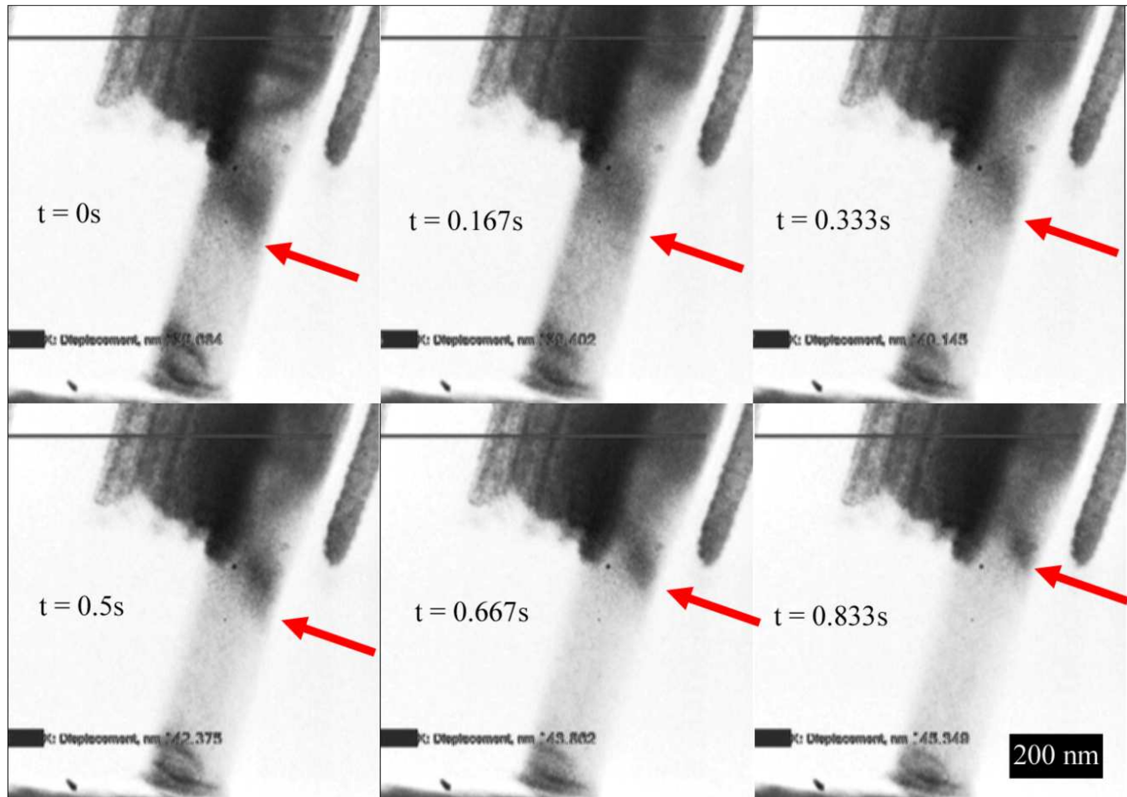

Figure 4.14. Sequence of first 0.8 seconds for damaged pillar under compression. The rapid velocity of the band initially in the center, indicated by the red arrow, is apparent. The velocity of the band is on the order of 100 nm/s. However, residual plasticity remains on unloading.

Unlike the time lapse micrographs of figure 4.9, the load – depth profile of a high aspect ratio pillar, figure 4.14, clearly indicates bending through a rounding over of the stress strain curve. During the hold period, a pair-wise feature appears near the tip, figure 4.15, indicating an elastic bending feature as was described earlier (figure 4.12). Also unlike the EBE pillar experiments, these CVD pillars showed residual damage after unloading.

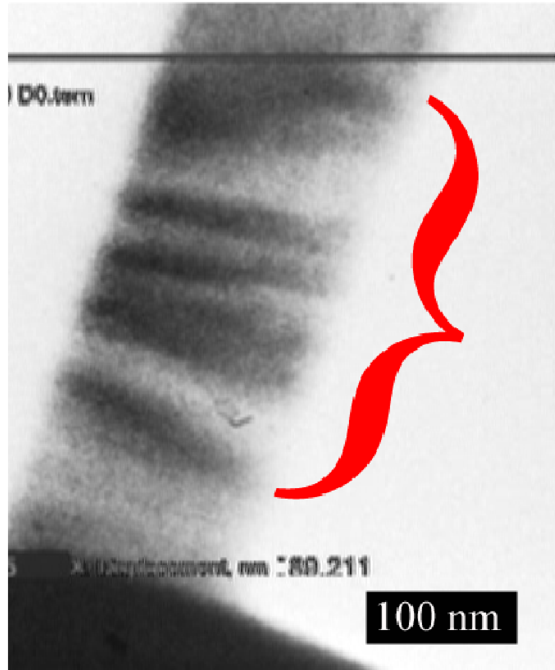

Figure 4.15. Pair-wise feature, indicated near the tip with red marker, which fluctuates with the applied load during the hold period. This feature is indicative of bending. Note that this image was taken on a later indent than figure 4.14, and there has been a change in magnification.

The dislocations, which appear to have been pushed to the end of the pillar then move rapidly back, not stopping until the end of the unloading, as seen in figure 4.16. Even for dislocations experiencing considerable back-stress, Eq. 4.8, an equilibrium stress prior to the zero load condition should occur. Therefore, this rapid movement is not the movement of the dislocations, but something I will refer to as “elastic-plastic bending,” since it has the character of both elastic bending and plasticity.

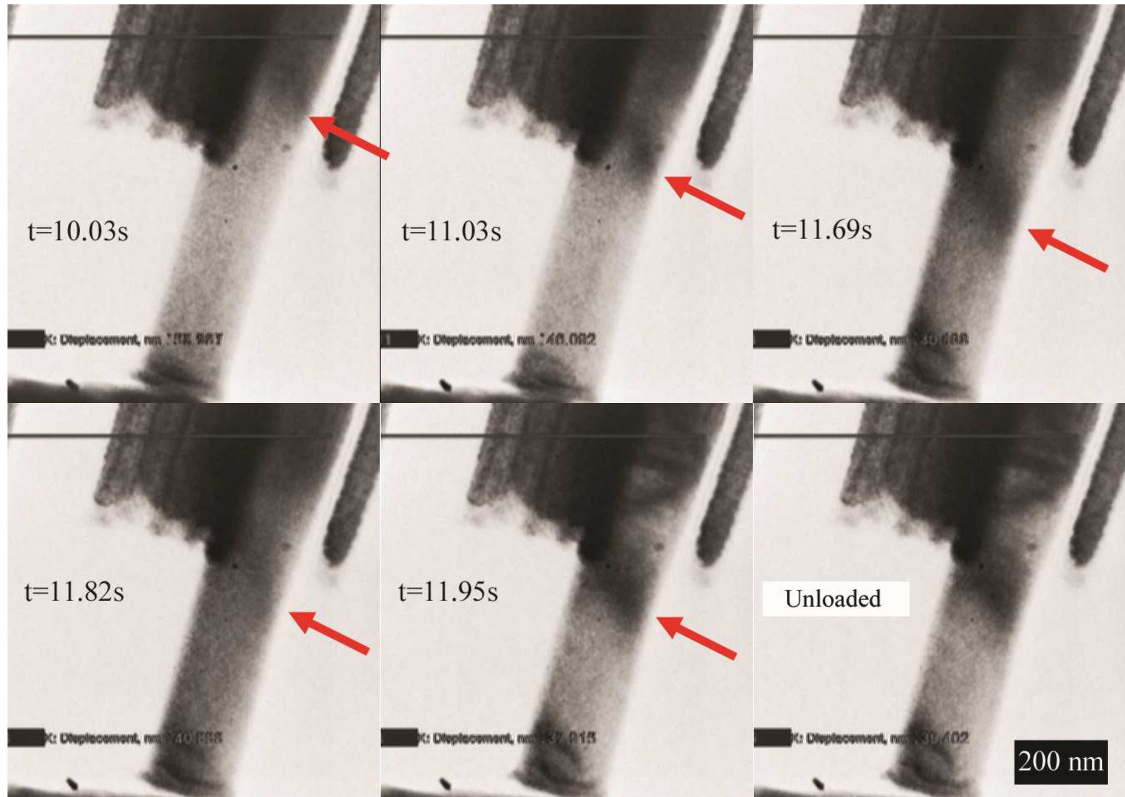

Figure 4.16. Diffraction bands move backwards on unloading, towards the indenter. Bands continue moving until indent ends at 12s. If dislocation movement was due to back-stress, there would be an equilibrium stress, prior to zero load.

It can therefore be concluded that the use of *in situ* indentation video would require significant deconvolution to understand the effects of bending, and what is happening to the accrued plasticity in the pillar. Of course, this could be done by simulating each video frame, or measurements could be done when the pillar is not in compression.

4.6. Dislocation imaging

In figure 4.13 it was shown that, for an edge dislocation in a thin foil, the intensity profile was "sharp." The astute reader will observe that the intensity profiles of the described "plasticity" of figures 4.14 and 4.16 are not sharp. Even under a no-load condition, such as the last frame of 4.16, the strain fields do not produce a sharp contrast. To investigate the origin of these diffraction contours a 120 nm diameter pillar was indented to a maximum stress of 4 GPa. With no capability for double tilt (tilting in both the α and β angles in the microscope) using the *in situ* holder, the pillar location was mapped, the sample lifted off the sample mount using the half-grid method described in chapter 3, and then placed in a double tilt holder. After compression, two additional series of micrographs were taken of this pillar. The first was done by Dr. Ozan Ugurlu, in collaboration with Professor Ikuhara, at Tokyo University in a 200keV microscope. The second was done by Andrew Wagner and the author of this thesis in a Tecnai F30 microscope operated at 300keV. Each image in this section will be attributed directly to the microscopist. The original bright field image of the pillar, prior to *in situ* deformation, figure 4.17(a), reveals no strain fields or prior damage. After a single compression, which due to the extreme aspect ratio of more than 10:1 had significant bending, a broad strain field appeared near the center of the pillar, figure 4.17(b). The initial bright field imaging in the 200keV microscope showed a similar feature, indicating that the pillar had not been further damaged, figure 4.18. This was as expected, as the pillars had been shipped previously without mishap.

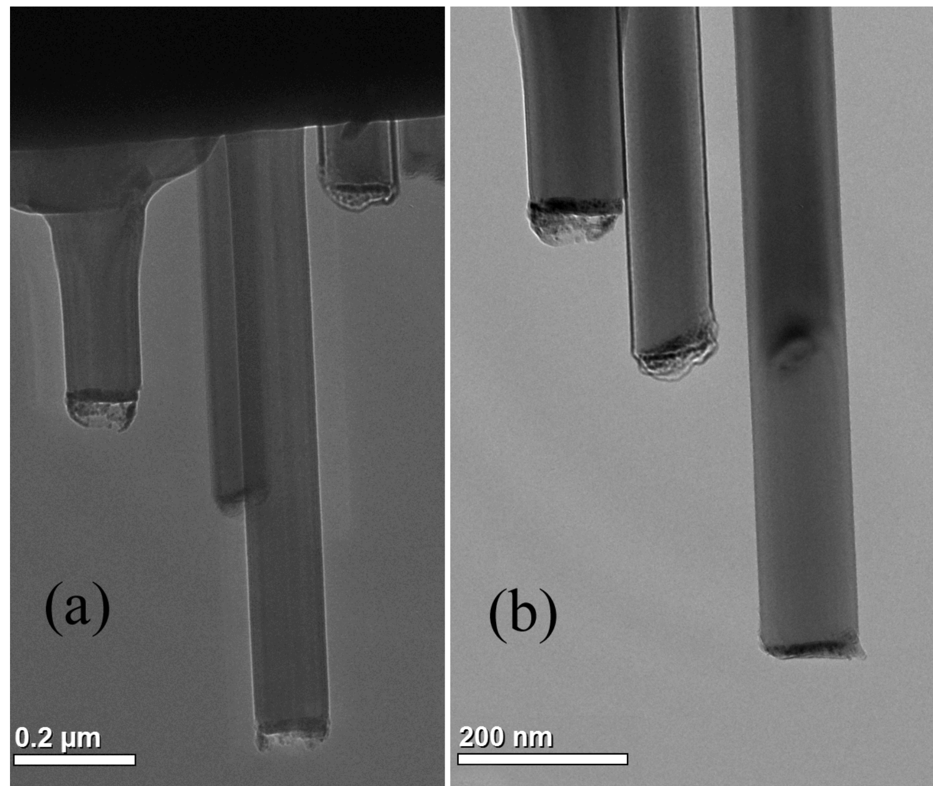

Figure 4.17. Before **(a)** and after **(b)** compression of a 120 nm diameter pillar, to a maximum stress of 4 GPa. No strain contours are visible prior to compression. The contour in the post-micrograph is broad, much like that seen in previous deformed pillars. Micrograph by D. Stauffer, 120keV.

Figure 4.18. Bright field image of 100 nm pillar in 200keV microscope. Strain field is broad, as seen in figures 4.14 and 4.16. Micrograph courtesy of Dr. Ozan Ugurlu.

It is in the dark field image of figure 4.19 that the nature of the strain field becomes apparent. The looping pattern of the dislocation, and the intersection of the dislocation with the amorphous oxide are clear. This intersection, where the strain field of the dislocation relaxes as the dislocation line ends, is typified by a blooming feature.[147, 202] This clearly indicates that the broad features seen in the bright field images are due to the interaction of the strain field across a sample with large variations in thickness.

Additionally, it is likely, from analysis of figure 4.20, that some of the contrast is due to the dislocation causing bending in the pillar.

Figure 4.19. Dark field image of the singly compressed 120 nm diameter pillar, with clear indications of a dislocation strain field, which relaxes at the surface. Courtesy Dr. Ozan Ugurlu.

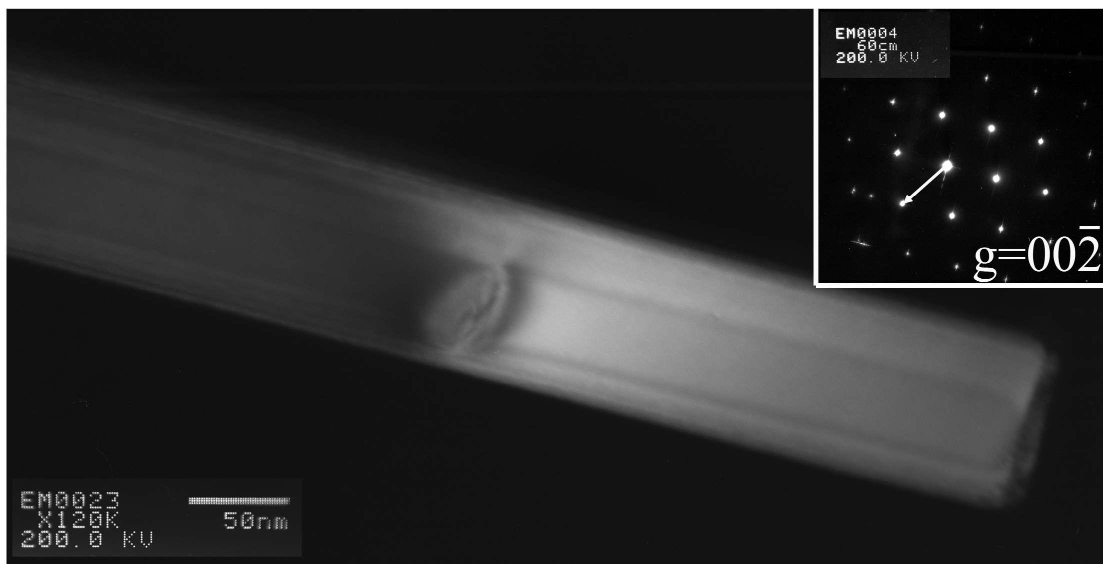

Figure 4.20. Dark field image of the same pillar, bisected by the dislocation. Top half is in a diffraction condition at $g = \left(4\bar{2}2\right)$, while the lower half is not. This indicates a kink in the pillar. Courtesy of Dr. Ozan Ugurlu.

An attempt was then made to analyze these micrographs to determine the Burger's vector, and thus isolate the dislocation plane that had been activated.

4.6.1. Dislocation Imaging: Burgers vector identification

There are two primary means of identifying dislocations in the TEM. Both involve imaging the strain field, $\vec{R}$, around the dislocation. The first, the "invisibility requirement," uses the fact that when the diffraction vector, $\vec{g}$, is perpendicular to the Burger's vector, $\vec{b}$, the resulting contrast in strain field should be zero.[203] This requires a collection of micrographs, varying both $\vec{g}$ and the zone axis. At least two conditions must be found to that satisfy this criteria in order to identify the Burgers vector. Additionally, this method is only truly valid for dislocations with pure screw character, as dislocations with mixed character will still be visible if $\vec{g} \bullet \vec{b} \times \vec{u} \geq 0.64$,[204] although Stach showed visibility for dislocations with $\vec{g} \bullet \vec{b} \times \vec{u} \leq 0.08$.[205] One major caveat to this technique is that thickness of the specimen can affect the image. Here, the specimen thickness is of a circular cross-section and thus varies constantly. One additional concern with imaging is the interference by other pillars and the substrate in tilting α (rotation in the axis of the holder) and β (rotation in axis perpendicular to both the holder and the beam), which limits the number of zone axes that can be imaged. The substrate is very thick, which blocks most of the beam, but can still diffract into the pillar image. Likewise, beams diffracted from the pillar can then interact with the substrate. This is more significant at the pillar base, which is avoided when testing long pillars. For this study, only a single image seemed to satisfy the invisibility criteria, figure 4.21, and then only partially.

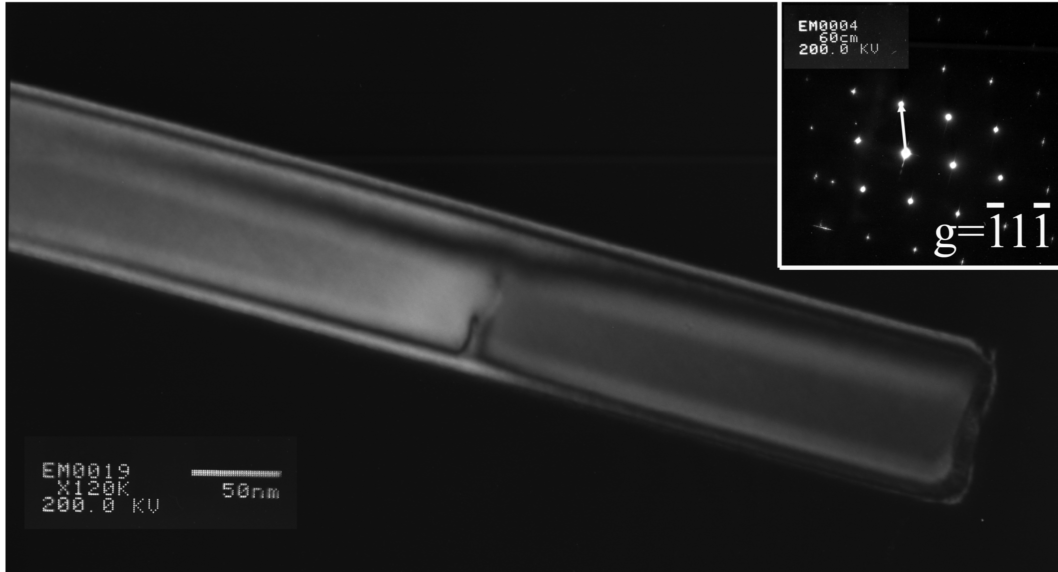

Figure 4.21. One half of the dislocation strainfield is in a "near invisibility criteria". This would require that multiple Burgers vectors be present. Courtesy Dr. Ozan Ugurlu.

Here, the strain field in the central part of the pillar is mostly invisible. This is unlikely if this dislocation were of pure screw character. If the total strain field is caused by multiple dislocations, then those dislocations would not share the same Burgers vector. It would also be possible, for a dislocation to undergo splitting into two Schockley partials, such that,

$$\frac{c}{4}\left[0\bar{1}1\right]=\frac{c}{6}\left[\bar{1}2\bar{1}\right]+\frac{c}{6}\left[11\bar{2}\right] \quad . \qquad \text{Eq. 4.11}$$

It is apparent, from Eq. 4.11, that these two partials would not have the same Burgers vector, so the partial invisibility criteria could also be valid for one of the Burgers vectors and not the other. These two partials would cause a stacking fault. Additionally, it has been noted in §4.1.1., that the dislocations on the shuffle set are more likely to split into partials.

4.6.2. High-resolution imaging

High resolution TEM (HRTEM) was also performed on the same sample, after being shipped back from Tokyo University, figure 4.22.

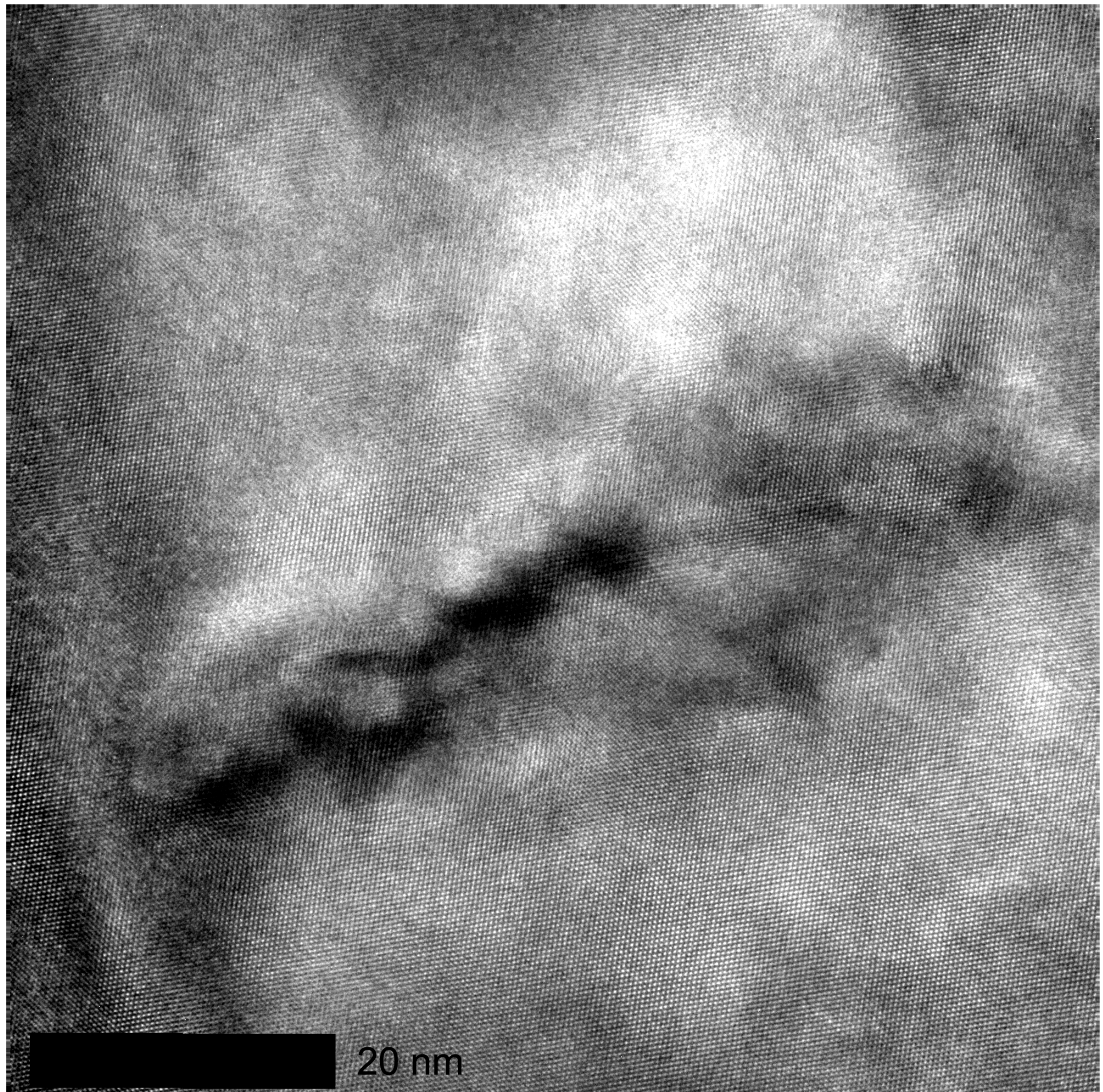

Figure 4.22. HRTEM of dislocated region in 120 nm pillar. The dislocation strain field interrupts the periodic lattice fringes. Courtesy Andrew Wagner

These micrographs clearly show the distortion in the atomic columns, but as detailed simulations have not been performed, the nature of the strain field has not been determined.

4.7. Dislocation velocities, part II

Having a greater understanding that the *in situ* video has been complicated by the combination of elastic and plastic bending, the use of "stop-start" methods, like that of the initial dislocation velocity experiments in LiF[206] were implemented. In these experiments, an applied load was held constant, with the dislocation velocity being described as;

$$v = \frac{\text{distance traveled}}{\text{time at max load}} \quad . \qquad \text{Eq. 4.12}$$

However, in these early etch pit experiments, shear was applied macroscopically, and thus easy to apply and maintain. In compression experiments, the strain rate must be controlled, so the dislocation velocity is defined as;

$$v = \frac{\text{distance traveled}}{\text{time under test}} \quad . \qquad \text{Eq. 4.13}$$

This should provide a lower bound for the dislocation velocities in the pillars. Tests were run with 5 s segments for load, hold, and unload, for a 15 s time under test. Velocities in the still images could be measured by using a pillar in the background as a reference point, figure 4.23.

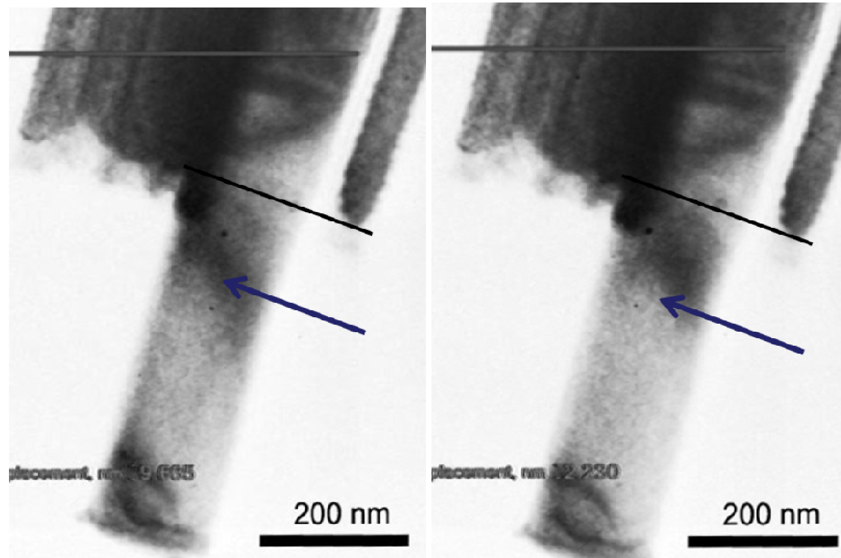

Figure 4.23. The broad band, indicating at least one dislocation, is pushed forward in this 180 nm diameter pillar, after the fifth compression. Measurements were taken at three positions for each band, as it is apparent that the band does not move uniformly along its length.

Measurements along the width of the diffraction band were made, as the band did not move uniformly. These measurements make up the statistical variation in the velocity. The shear stress was calculated assuming a Schmid factor of 0.272, since the type of dislocation was not exactly known. This, as well as the bending, could introduce errors in the calculation of applied shear stress. However, since the bands are seen across the pillar, and the pillar velocities take into account these variations, the effects of bending have, for the most part, been taken into account in the velocity statistics, figure 4.24.

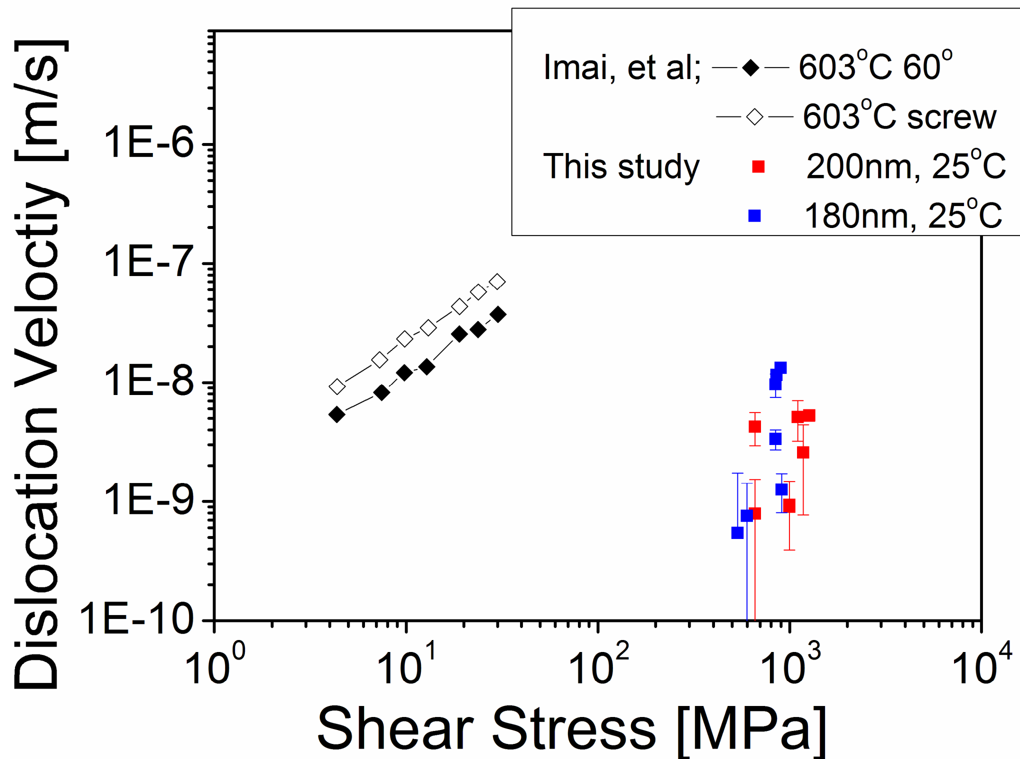

Figure 4.24. Dislocation velocities for Imai at 603°C for bulk silicon,[158] as a variation of stress, compared to those found in this study. The velocities found by here are of the same order of magnitude, but at a much higher shear stress.

Two interesting points arise when looking at these velocity – shear stress plots. The first is the order of magnitude of the velocities, as large as 2×10^{-8} m/s, larger than the lowest values found by Imai, et al at 603°C. However, this was achieved primarily in compression with two orders of magnitude higher applied shear stress. This may be more evidence that the ability of nanoscale silicon to nucleate dislocations and allow them to glide may be linked to the high compressive stresses in these tests, as opposed to the three and four-point bend test of either Roberts or Imai.[158, 164] The second point is the wide spread in the velocities measured by this method. Interestingly, the dislocation velocities for each subsequently nucleated dislocation from a repeatedly compressed pillar had a lower velocity. This is likely due to a pile-up mechanism, which is effectively reducing the applied stress on the dislocations. Since the exact type and

number of dislocations is not known in this case, it cannot be exactly determined using the pile-up model, detailed in Gerberich, et al.[180]

$$N = \frac{\pi(1-\nu)\tau_{applied}\ell_s}{\mu b} \qquad \text{Eq. 4.14}$$

However, if each band in figure 4.23(c) represented a single dislocation, with an average spacing of $\ell_s = 150\text{nm}$, that the actual applied shear on the 10th dislocation, would only be 60% of the actual applied stress. Additionally, the source would feel essentially no applied stress after 16 dislocations had been nucleated under these conditions. This pile-up, which gives silicon the ability to work harden, is the subject of chapter 5.

4.8. Summary

Silicon is described as a classically brittle material, despite decades of research showing that plasticity may be induced in silicon single crystals under high stress levels. *Ex situ* examinations of deformed samples have left open the possibility of phase transformation induced plastic strain. Here, an *in situ* study shows abundant evidence that this residual plasticity is the result of dislocation nucleation and long-range movement **at high velocities at room temperature**. These dislocations pile-up against boundaries within the pillars, which decreases the velocities of dislocations nucleated on subsequent compressions. This strain hardening behavior is the subject of chapter 5.

Here we present direct room temperature measurements of the stresses required for dislocation nucleation and the velocities of dislocation band motion using an *in situ* showing abundant evidence that residual plasticity is due to dislocations that move at high velocity. Reproducible results were observed for 12 repeat runs on the same pillar, and then again for another pillar.

A complete understanding of the mechanism would require access to the extracted and deformed pillar on a grid to further attempt to categorize the type of dislocations. Without knowing the type of dislocation present, there can be no further analysis of the corresponding activation energies for kink-step nucleation. [196, 207, 208] This latter is likely the key to understanding the dislocation motion.

Chapter 5. Strain-hardening in sub-micrometer silicon systems

5.1. Introduction

For devices in switches requiring electrical contacts or MEMS devices subjected to repeated stress, friction or wear, strain-hardening capacity can be critical. From the previous chapter, discussing initial plasticity and dislocation velocity, it was observed that the dislocation velocities decrease on repeated loading. However, to date, there has been little understanding of strain-hardening at the nanoscale due to the difficulties in performing or interpreting such experiments. For many studies, there is a perception that little strain-hardening exists. This is due to the dislocation exhaustion mechanism, by which dislocations escape to the free surface under loading.[131, 197, 209, 210] These studies have mostly focused on face-centered cubic metals. More recently, however, there is a growing recognition that BCC nanopillars do harden,[132, 133] and even FCC metals harden in confined structures, which prevent the escape of dislocations.[130] For other crystal structures such as zinc blendes or diamond cubic, Rabier and Demenet[171] demonstrated substantial hardening for compression under confined pressure, and significant literature exists for bulk strain- hardening in tension and torsion at high temperatures.[211, 212] Additionally, during examination of sub-micrometer silicon nanospheres in the 40 to 400 nm scale regime, it is apparent that even very small silicon single crystals undergo strain-hardening.[178, 179] This is a pivotal test case between metals and ceramics for our hypothesis that crystalline materials can have strain-hardening capacity in compression. The semiconductor silicon is known to undergo some plasticity during nanoindentation, much more than oxides and carbides but less than metals and intermetallics. For such a material, with yield stresses in the GPa range due to its high Peierls barrier,[213, 214] it is difficult to conceive of very large strain-hardening capacity. Nothing could be further from what is observed.

In the following, experimental evaluations of nanospheres and nanopillars will be described. These demonstrate that strain-hardening exponents greater than 0.3 might exist in both. In the case of more greatly confined spheres, values near unity arise. Experimentally, nanopillars are straightforward but nanospheres are analyzed two ways due to complications of the spherical geometry leading to strain gradients. Single crystal

silicon pillars in the range of 180-415 nm in diameter and spheres in the range of 39 to 338 nm in diameter are described.[179] Examples of the plastic deformation which may arise in these are shown in figure 5.1, with numerous additional examples in chapter 4.

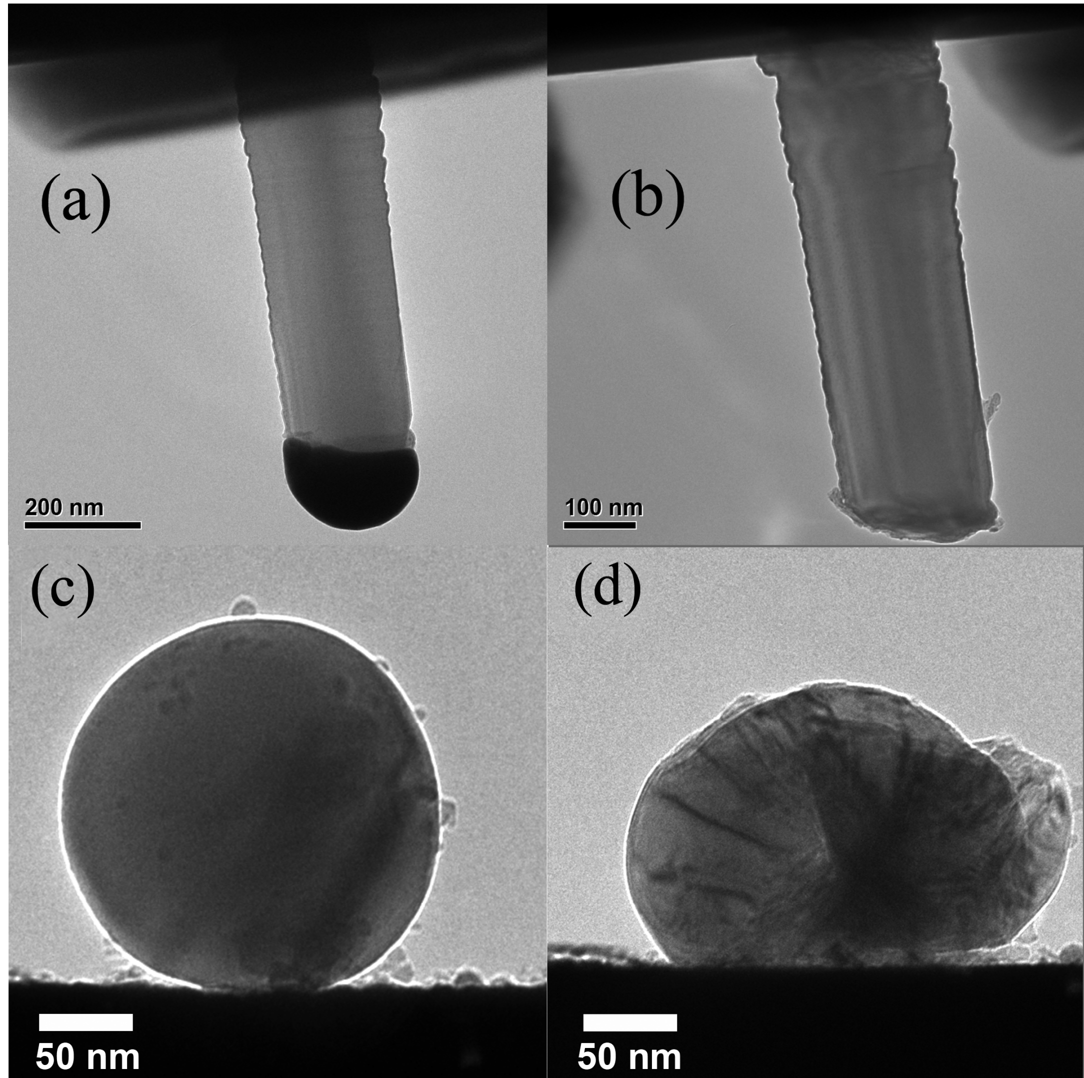

Figure 5.1. TEM micrograph examples of *in situ* work hardened Si nanopillars (a, b) and spheres (c, d). The undeformed 180 nm Si pillar of **(a)** was compressed three times to a strain of less than 5% **(b)**. The Au cap, from the VLS growth, adhered to the indenter. The Si sphere **(c)** was compressed once **(d)**. Residual plastic damage is observed in both pillars and spheres. Images (c) and (d) are courtesy of Dr. Aaron Beaber.

Regarding the source(s) of hardening, an ad hoc theoretical application of surface mediated dislocation nucleation is applied to both spheres and pillars. Different size

effects are observed wherein the magnitude of strain-hardening exponents changes with length scale due to relative geometry and constraint effects.

5.2. Experimental procedures

The experimental analysis is complex for spheres as the initial contact, a diamond indenter at the top and a flat sapphire substrate at the bottom of the spheres, gives small contact areas. The deposition and analysis of such spheres being deposited by a low pressure, high temperature plasma through a nozzle at hypervelocity is described in more detail elsewhere.[215] The original experiments on spheres[178, 179] were evaluated by compression with a Hysitron Triboscope™ mounted on a Digital Instruments™ atomic force microscope (AFM). Later, similar experiments were repeated with *in situ* imaging. This utilized a PicoIndenter™ measuring load-displacement inside a JEOL™ or FEI-T12™ transmission electron microscope (TEM), as described in chapters 3 and 4.

Load-displacement curves in the AFM based system enabled the testing of somewhat smaller nanoparticles, due to line-of-sight requirements inherent in the TEM. These AFM based experiments were conducted under load-controlled feedback. As discussed by Mook, et al.,[179] repeated runs on the same nanoparticle could be obtained with total strains up to approximately 0.2 in individual runs and a summation up to 0.5. A series of runs for a 43.6 nm diameter sphere are shown in figure 5.2. As the total strain could be quite large, flattening of the sphere at the top and bottom needed to be considered.

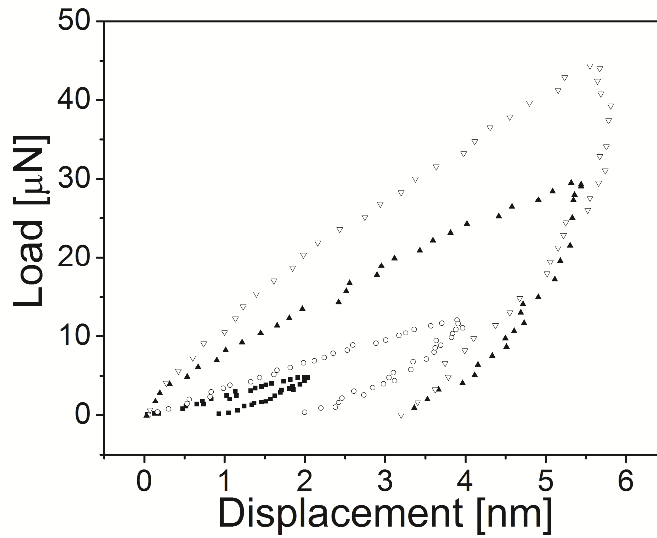

Figure 5.2. Load-depth curves for repeat loading of a 43.6 nm sphere, where loading was done with a Triboscope system in load control. Yielding and residual plasticity was observed from all indentations. While strain is considered to be zero for any individual load-depth curve, the plastic deformation was cumulative. An increase in the contact area resulted from this cumulative deformation. Adapted from Mook, et al.[216]

Initially, the contact areas were small and even at small loads the contact stresses were large. To quantify the stresses, the geometric contact radius was found from

$$a = \left[\delta r - \frac{\delta^2}{4} \right]^{1/2} \qquad 5.1$$

where δ is the total displacement divided equally into the top and bottom of the sphere of radius, r. As such, this was considered to be a geometric contact due to elastic and plastic deformation. It was also considered that, within the experimental measurement error, that the compliance of the tip (diamond) and substrate (sapphire) were small contributions to the total displacement, in comparison to the strain of the silicon. Given that the region directly under the contacts is undergoing severe plastic deformation, this required two additional steps to evaluate the global strain-hardening, particularly for repeat runs. First, upon unloading, any subsequent runs needed to consider that the initial contact area would increase due to previous residual plastic deformation. This could be measured with AFM as described in Mook, et al.[178, 179] However, the strains were

considered to start from zero in the unloaded state for any given run as required. Note then that these repeat compressions on AFM tested spheres have been previously strain-hardened. The second step was to take into account that the center of the sphere was not initially experiencing as much plastic strain although recent atomistic simulations clearly demonstrate dislocation loops completely traversing the sphere diameter when nucleated at either the top or bottom. Still, the stresses are smaller in the sphere center, and to obtain a more representative equivalent stress, a conversion of initial radius of the sphere, r_0, to an effective radius, r_{eff}, was needed.

5.2.1. Contact approximations

Two approximations were used to model the complex contact behavior of spheres in compression. One, using a bilayer model where the stresses (and deformation) are concentrated near the contact edges is more applicable to small strains, while the other which assumes gross distortion of the sphere, is more applicable to large strains. As the large strain approximation was used for the initial work, it is described first, with the lower bound of the small strain approximation using previously defined terms.

5.2.1.1. Right cylinder approximation

For severe plastic deformation (large strains), as seen in figure 5.1(d), the damage region occupies a large percentage of the volume of the sphere. At this point the "sphere" is grossly distorted, and the dislocation interaction and thus work hardening can increase. Here, a constancy of volume for plastic strains is used, where the assumption is that the corners of a right cylinder, shaded darkly in figure 5.3 are equivalent to the truncated sides of a "pancaked" sphere such that r_{eff} of a right cylinder gives the same volume as the original, undeformed sphere. The experimental view in figure 5.1(d) is in the "unloaded" state. Therefore there has been elastic springback of both the top and bottom surface of the sphere.

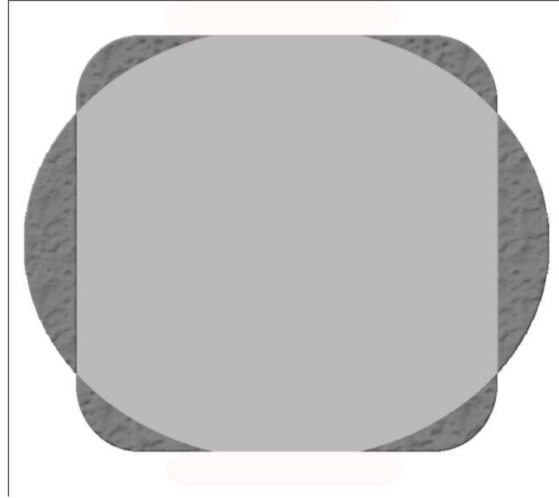

Figure 5.3. Schematic representation of the right cylinder approximation, where damage deforms the edges of the contact into something more resembling a flat surface. The contact area can then be described as a right cylinder of volume equal to the sphere prior to compression.

Equating the volumes of the original sphere and the right cylinder,

$$\frac{4}{3}\pi r_0^3 = \pi r_{eff}^2 \left(2r_0 - \delta\right) , \qquad \text{Eq. 5.2}$$

where the right cylinder has been foreshortened from the original sphere height, $2r_0$, by δ. This then gives an effective cylinder radius of

$$r_{eff} = 1.155\left[\frac{r_0}{2r_0 - \delta}\right]^{1/2} , \qquad \text{Eq. 5.3}$$

which can then be used to calculate the stresses for individual experiments. Stresses were evaluated in two ways, using the equivalent right cylinder with $A = \pi r_{eff}^2$ and by using a contact stress with a the contact radius of Eq. 5.1 with $A = \pi a_c^2$. Here, $2a_c$, is the contact diameter at both the top and the bottom. Using r_{eff}, this gives an estimate of the average stress for an equivalent volume.

Also considered was a harmonic mean stress viewing the deformed sphere as a strained, bilayer structure. Here, the contact stresses at the top and bottom would control dislocation nucleation, but the overall strain-hardening capability would be influenced by the entire volume.

5.2.1.2. Harmonic mean approximation

For spheres under low plastic strains, the stress is primarily concentrated near the contact. This gives rise to damaged regions at the top contact (with the indenter) and the bottom contact (substrate), figure 5.4.

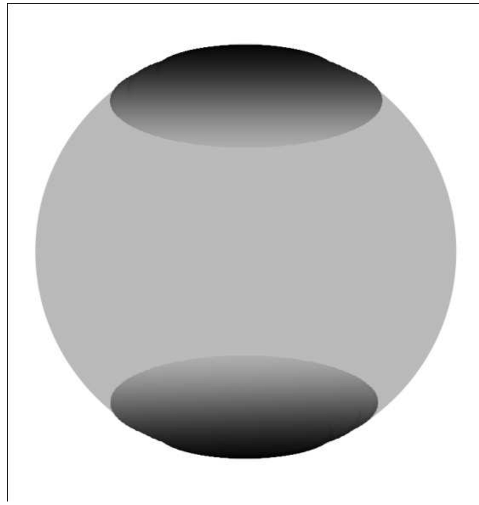

Figure 5.4. Schematic representation of the harmonic mean approximation in a sphere, where a bi-layer system is used to model the damage region, near the contacts, in a sphere.

For these harmonic mean stresses, the spheres were taken as layers of highly deformed regions at the top and bottom with the contact area based upon Eq. 5.1, and a more nearly average area radius from Eq. 5.3. The concept of a layered structure, as observed by TEM contrast differences[217] gives rise to a harmonic mean stress as used by Hill for composite structures.[218] This gave a stress intermediate to those using the contact radius from Eqs. 5.1 and with the harmonic mean given by

$$\sigma_m = \frac{2}{\dfrac{1}{\sigma_C} + \dfrac{1}{\sigma_{cyl}}} \quad . \qquad \text{Eq. 5.4}$$

Here σ_C is the contact stress using Eq. (1) and σ_{cyl} is the equivalent stress of a right cylinder using Eq. 5.3. The harmonic mean stress is the Voigt average, which represents a

lower bound. A similar set of procedures for strains used the strain in the two contact regions after Tabor [23] to be,

$$\varepsilon_c = 2\left\{0.2\left(\frac{a}{r}\right)\right\} \quad , \qquad \text{Eq. 5.5}$$

which is twice that of the spherical indenter strain, Eq. 1.25, as strain occurs in both the top and the bottom of the sphere. For an average strain in the sphere, the total displacement, δ, divided by the sphere diameter, gives

$$\varepsilon_d = \frac{\delta}{d} \quad . \qquad \text{Eq. 5.6}$$

Coupling the Tabor strain with the global estimate, Eqs. 5.5 and 5.6, gives the harmonic mean strain

$$\varepsilon_m = \frac{2}{\dfrac{1}{\varepsilon_C} + \dfrac{1}{\varepsilon_d}} \quad . \qquad \text{Eq. 5.7}$$

For much larger strains, the deformation would be more evenly distributed throughout the sphere and the rationale of a right cylinder would be more appropriate, as discussed previously.

5.2.2. True stress – true strain

The stress-strain could then be assessed from the previous data, for a right-cylinder approximation and for a harmonic mean representation. The strain-hardening behavior was then evaluated using true stress-true strain plots in compression as determined from

$$\sigma_T = \sigma\left(1+\varepsilon\right) \quad ; \quad \varepsilon_T = \ln\left(1+\varepsilon\right) \quad . \qquad \text{Eq. 5.8}$$

It is important to keep in mind that, in compression, strains are negative. As a sphere or pillar is compressed the cross-sectional area increases making the true stress somewhat less than the engineering stress. From such plots, the strain-hardening exponents, n, were then determined from the power-law equation,

$$\sigma_T = k\,\varepsilon_T^n \quad . \qquad \text{Eq. 5.9}$$

Using Eq. 5.9, strain-hardening exponents were also determined for columns of nanopillars loaded in compression. Only a few of these data were analyzed, two representing pillars prepared by focused-ion-beam (FIB) machining, and others representing growth by a vapor-liquid-solid (VLS) process. The FIB samples had a small taper but the CVD VLS samples, as supplied by NIST, were relatively straight-sided.

5.3. Results on silicon spheres

From data, such as that shown in figure 5.2, strain-hardening exponents were determined as discussed above. Two sets of true stress – true strain data for repeat runs are shown from the load control data in figure 5.5.

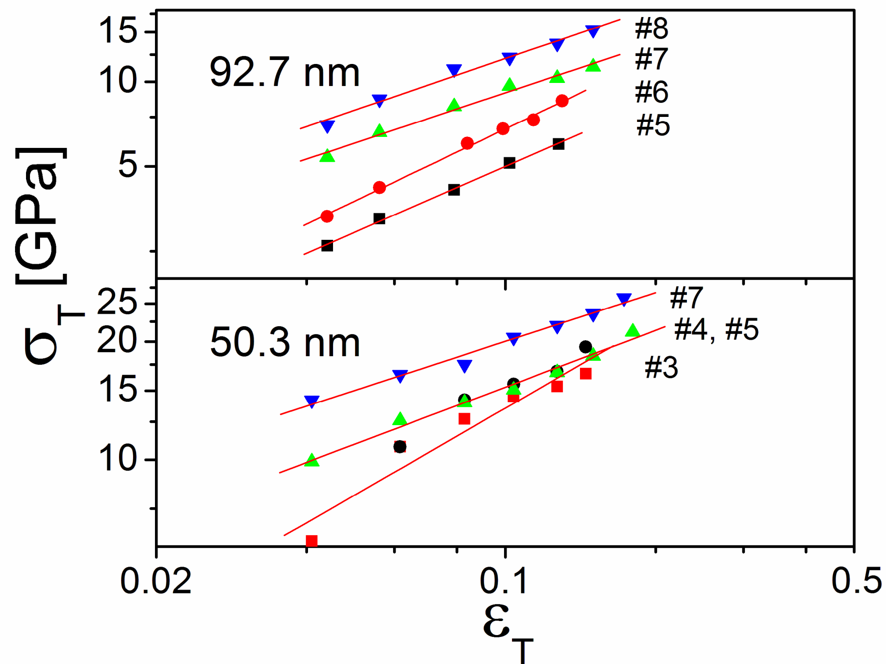

Figure 5.5. True stress – true strain for two spheres tested in the AFM based Triboscope system, where the harmonic mean approximation was used to determine the stress. Work hardening, due to cumulative damage, can be seen as increasing stress for a given strain as the run number increases. The strain hardening exponents, table 5.1, were calculated from these plots.

Strain magnitudes were generally between 0.02 and 0.2. For each subsequent run, the stresses were generally higher than the previous run. For example, at a strain of 0.1 for runs 5 through 8 for the 92.7 nm diameter sphere, the stresses increased from 5 to 6.8 to 9 to 12.5 GPa. However, a minor variation in the strain-hardening exponents resulted, as determined for the effective right cylinder. Similarly, for several runs the stresses increased from about 14 to 20 GPa at a strain of 0.1 for a 50.3 nm diameter sphere, but with greater variation in strain-hardening exponent. For five such nanoparticles, strain-hardening exponents are reported for repeat runs in table 5.1 based on the right cylinder method. For a given sphere there appears to be no dominant trend in *n* with run sequence. Except for the smallest nanosphere, there does appear to be a strong increase in strain-hardening exponent with increased sphere diameter. Average values increased by a factor of three from 0.25 to 0.75 as size increased from 43.6 nm to 92.7 nm.

Sphere diameter [nm]	Test Method	Run # / strain hardening exponent, *n*						$\bar{n}$
38.6	LC	2/0.79	5/0.90	7/0.94	9/0.75	12/0.78	15/0.66	0.80±0.14
43.6	LC	2/0.23	3/0.21	4/0.15	5/0.38	6/0.29		0.25±0.13
50.3	LC	2/0.41	3/0.49	4/0.49	5/0.44	7/0.39		0.44±0.05
63.5	LC	2/0.62	3/0.63	4/0.64	5/0.64	6/0.63		0.63±0.02
92.7	LC	3/0.81	4/0.81	5/0.75	6/0.77	7/0.69	8/0.65	0.75±0.10

LC = load control

Table 5.1. Strain hardening exponents, measured for each run for multiply loaded Si spheres of diameters from 38.6 to 92.7 nm. A Triboscope/AFM system was used in load-controlled mode for these compressions. The strain hardening exponents were calculated using the right cylinder approximation, described in more detail in §5.2.1.2.

Additionally, for eight spheres in the size range of 60 to 340 nm, single runs were conducted generally to a strain of 0.4 as represented by Eq. (6). These tests were conducted with the *in situ* transmission electron microscope system in displacement control. Examples for four of the runs in figure 5.6 show a similar trend of increasing stress with decreased size. Here for stresses defined by the right cylinder method, at a strain of 0.1, there was nearly a factor of six increase in average stress as size decreased. This is larger than what might be expected as addressed in the discussion session. A

factor of four increase in sphere diameter produced a factor of four increase in strain-hardening exponents tested in displacement control, in contrast to the 63 nm sphere tested in open-loop. See table 5.2 and figure 5.6. Displacement control is known to be more sensitive than either open-loop or load control in showing discrete events.[52]

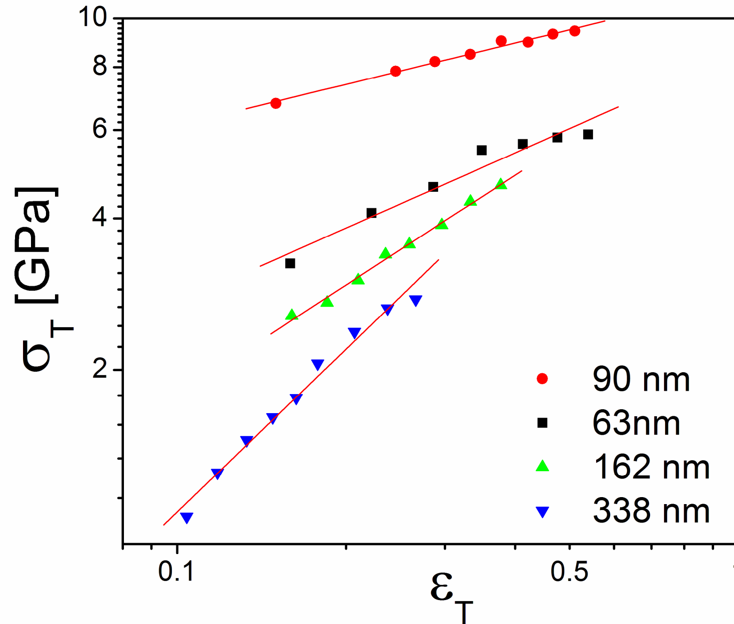

Figure 5.6. A comparison of the true stress – true strain plots for the first compression of individual spheres, tested in load control, shows that as sphere size decreases, the stresses increase, but the strain-hardening exponent decreases. Stresses here are determined using the right cylinder approximation.

Sphere diameter [nm]	Test Method	n (Right Cylinder)	n (Harmonic Mean)	$\bar{n}$
63	Open Loop	0.55	0.43	0.49
90	DC	0.33	0.31	0.32
113	DC	0.23	0.23	0.23
138	DC	0.64	0.67	0.66
162	DC	0.76	0.88	0.82
173	DC	0.84	1.23	1.04
255	DC	1.09	1.31	1.20
338	DC	1.21	1.40	1.31

Table 5.2. Strain hardening exponents, measured for each run for Si spheres singly compressed primarily in displacement control. Here, an *in situ* PicoIndenter was used to perform the compressions. Exponents are given for each of the two analysis methods, harmonic mean and right cylinder approximations, detailed in §5.2.2.

To double check the efficacy of these estimates of strain-hardening, the layered structure of the harmonic mean approach of Eqs. 5.4 and 5.7 was also used to determine *n*. Examples of four true stress-strain plots are shown in figure 5.7. Compared to the data for the 90 nm and 162 nm spheres of figure 5.6, the log-log slopes were similar.

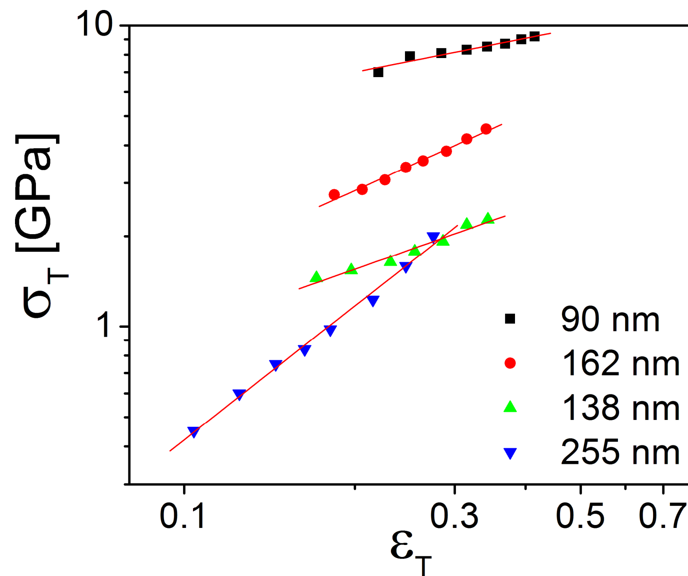

Figure 5.7. A comparison of the true stress – true strain plots for the first compression of individual spheres for *in situ* tests that as sphere size decreases, the strain hardening exponent decreases. Stresses here are determined using the harmonic mean approximation.

5.4. Results on silicon pillars

For the silicon pillars, the relatively uniform diameters simplified the stress analysis and only load/area and displacement/length were used to analyze engineering stress-strain, with conversion for a true stress – true strain by Eq. 5.8. Six pillars were analyzed for their strain-hardening characteristics. The 160 nm diameter pillar was examined for its response to repeat runs where residual plastic strains were small, on the order of 1 – 2 percent. Beyond this there was clearly an onset of bending, as discussed in chapter 3 and 4. Stresses for each run typically ranged between 2 – 4 GPa, as shown for four of the runs in figure 5.8.

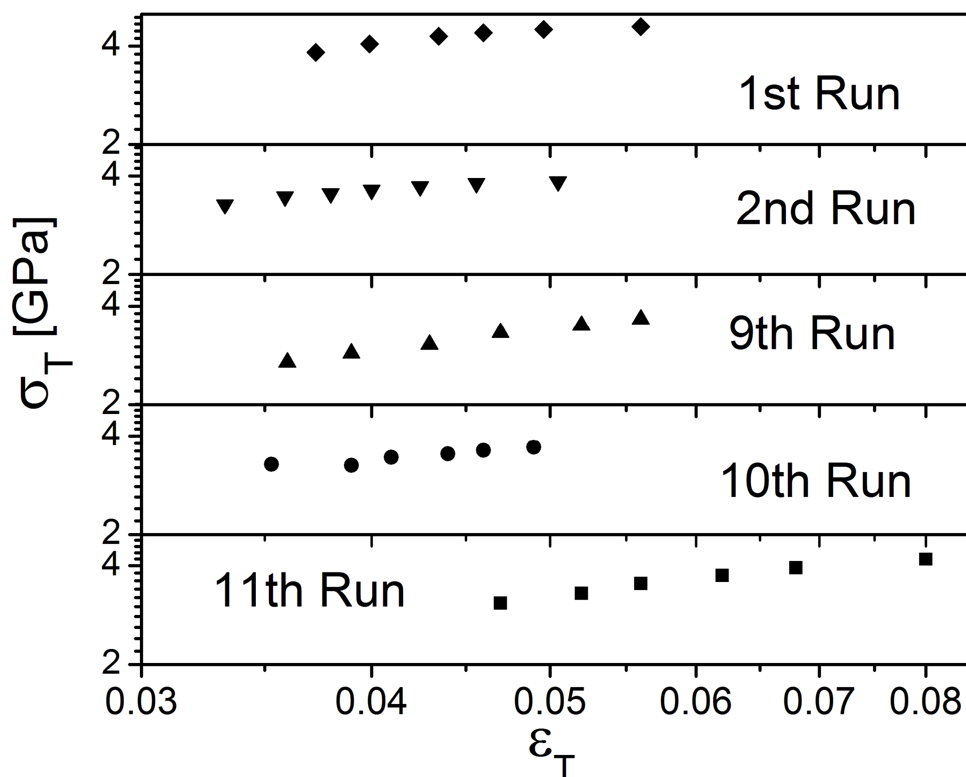

Figure 5.8. Repeat compression true stress – true strain for a 180 nm $\langle 111 \rangle$ oriented Si pillar, grown by VLS. The strain-hardening exponents have slight increases for each subsequent compression. The strain-hardening exponent values are found in table 5.3. Bending of the pillars was observed at larger strains.

Examples of single stress-strain behavior of four different pillars, two each of $\langle 100 \rangle$ and $\langle 111 \rangle$ orientations are shown in figure 5.9. These represent larger diameter pillars with smaller (3 to 4:1) aspect ratios.

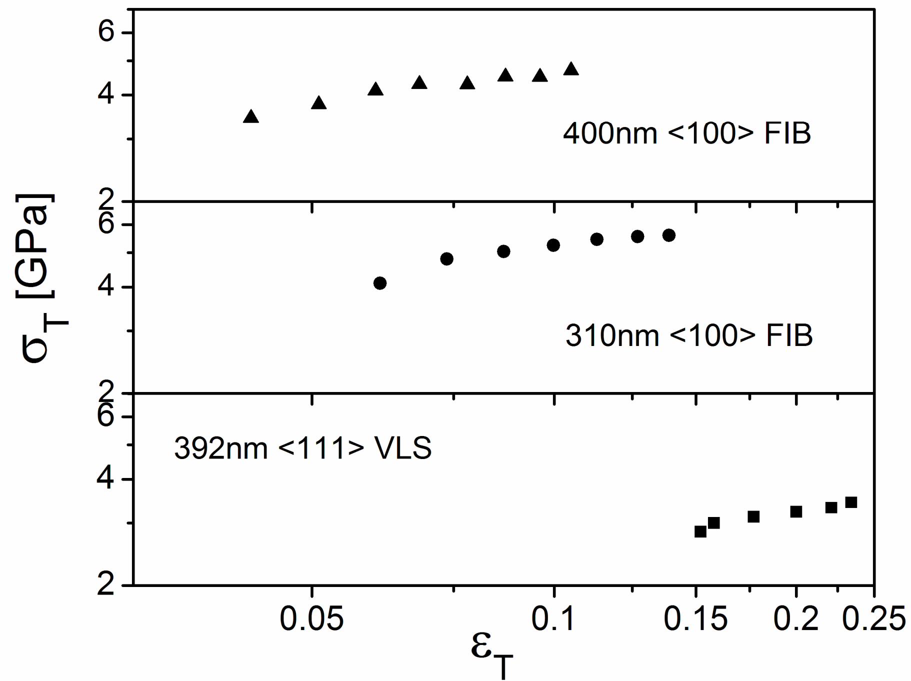

Figure 5.9. True stress – true strain plots for three FIB cut Si towers. Two towers are oriented in the $\langle 100 \rangle$, and one in the $\langle 111 \rangle$. Values for the strain-hardening exponent are in table 5.3.

In general the strain-hardening exponent increased with repeat runs but seemed to decrease with increasing pillar size. This latter result appeared to be inconsistent with the sphere size effect where the exponent increased with increasing sphere size; see table 5.3. After some theoretical considerations, such differences will be discussed.

Table 1(c): *In-Situ* TEM strain hardening exponents of nanopillars

Pillar diameter [nm]	Test Method	*n*	Orientation	notes
180	DC	0.415	<111>	Plastic bending or buckling suggested
200	DC	0.706	<111>	
310	DC	0.316	<100>	FIB cut
392	DC	0.355	<111>	VLS grown
400	DC	0.293	<100>	FIB cut
415	DC	0.220	<111>	VLS grown

DC = Displacement Control   FIB = Focused Ion Beam   VLS = Vapor - Liquid - Solid

Table 5.3. Determination of strain-hardening exponents of Si pillars using the *in situ* SEM and TEM PicoIndenters for $\langle 111 \rangle$ and $\langle 100 \rangle$ oriented pillars operated in displacement control. For some pillars, the large aspect ratio resulted in observable bending/buckling of the pillar. Both Vapor-Liquid-Solid grown and Focused-Ion-Beam machined pillars were studied.

5.5. Strain-hardening model

Due to the apparently large variations in strain-hardening exponents in table 5.2, it is important to provide an analysis as to why there would be a large size dependence. Two obvious variables are dislocation nucleation limited and dislocation plasticity motion limited behavior. As size decreases, the number of nucleation sites, particularly at the free surfaces, becomes small. Similarly, a decreased size could limit the mean free path of dislocation motion if all, or most of, the dislocations remain. Such constrained flow could possibly increase both strength and strain-hardening. Here, a first-order model is proposed using these size constraints, coupled with nucleation theory.

First, consider spheres under the compression of two relatively flat platens. The overarching assumption is that strain-hardening will be mediated by the number of surface sites per unit area. Here, the unit area is assumed to be the contact area as surface asperities under contact will represent stress concentration sites. Taking the contact area,

A_C, at both the top and bottom to be that given by Johnson[13] for neither pile-up nor sink-in,

$$A_C = \pi a^2 = \pi \delta d \quad , \qquad \text{Eq. 5.10}$$

where a is the contact radius, δ is the displacement, and d is the sphere diameter. As before, the strain is defined by Eq. 5.6, which when combined with Eq. 5.10, gives

$$A_C = \pi d^2 \varepsilon \quad . \qquad \text{Eq. 5.11}$$

This is intuitive, since increasing displacement (strain) will broaden out the contact region. The further assumption is that the number of available nucleation sites, at the contact surface, increases with strain, and is proportional to both the strain hardening exponent, and to the increase in contact area, giving

$$n \propto \frac{d\,A_C}{d\,\varepsilon} \propto \frac{d}{d\,\varepsilon}\left\{\pi d^2 \varepsilon\right\} \propto \pi d^2 \quad . \qquad \text{Eq. 5.12}$$

Since a given nucleation site will more easily nucleate a dislocation the higher the applied stress, Eq. 5.12 can then be modified to accommodate this, giving

$$n \propto \frac{\sigma}{\mu} \pi d^2 \quad , \qquad \text{Eq. 5.13}$$

with the stress normalized by the shear modulus, μ. The number of sites would be the contact area divided by the area of a given site, A_S, this latter value being given an ad hoc assignment. It is assumed that a nucleation site is proportional to an activation area, which is proportional to the Burgers vector, b, times a length parameter, ℓ_S, as described by Cordill, et al.[219] With Eq. 5.13, and the proportionality to the number of nucleation sites per unit area, A_C/A_S, this becomes

$$n \propto \frac{\sigma}{\mu} \cdot \frac{\pi d^2}{\chi \ell_S b} \quad , \qquad \text{Eq. 5.14}$$

with χ a proportionality factor for activation area. The normal stress must be resolved on a slip plane, and the diameter of the sphere affects the applied stress, approximated by a Hall-Petch relationship, $k_y d^{-1/2}$. With the activation length scale proportional to the sphere diameter, $\ell_S = \gamma d$, one postulates that

$$n = \text{const.} \times \frac{\text{no. of contact surface sites}}{\text{unit area}} \times \frac{\sigma}{\mu} \quad , \qquad \text{Eq. 5.15}$$

and combined with Eq. 5.14, a Hall-Petch stress and resolved shear, gives

$$n = \frac{\pi k_y d^{1/2} \cos\phi \cos\lambda}{\chi \gamma b \mu} \quad . \qquad \text{Eq. 5.16}$$

One last point is there should be a cutoff diameter, d_0, below which there are no, or insufficient dislocations, nucleated to give strain-hardening. Here, d_O was chosen to fit the data, and a k_y equal to $1\,\text{MPa}\cdot\text{m}^{1/2}$ was selected as it represented a simple but reasonable representation of strength data previously published,[179, 220] as well as the new data of this investigation.

$$n = \frac{\pi k_y (d - d_O)^{1/2} \cos\phi \cos\lambda}{\chi \gamma b \mu} \quad . \qquad \text{Eq. 5.17}$$

For a constant $\pi k_y / \chi \gamma b$, the data can be fit for two orientations of diamond cubic silicon with respect to the indentation axis. These are the $\langle 100 \rangle$ and $\langle 111 \rangle$ where $\cos\phi \cos\lambda$ would be 0.408 or 0.272 for $\{111\}$ slip, and can be considered an upper and lower bound to the possibilities for resolved shear.

Consider an example case of a 320 nm sphere. Note that with b = 0.384 nm, $k_y \cong 1\,\text{MPa}\cdot\text{m}^{1/2}$, and $\mu = 66\,\text{GPa}$, that $\chi\gamma$ would be 17.8 for a 320 nm sphere with a value of 40 nm chosen for d_0. The proportionality factor, γ, can be determined by $\ell_S = \gamma d$, if the length scale parameter is known. From several previous studies of deformed nanospheres,[(20, 21)] the activation volume in silicon nanospheres for dislocation nucleation can be determined by

$$V^* = \ell_S b^2 \quad . \qquad \text{Eq. 5.18}$$

Therefore, V^* for a 320 nm particle is $50 b^3$. Since the activation volume is equivalent to the activation area times the Burgers vector, it is seen that,

$$V^* = A^* b \quad . \qquad \text{Eq. 5.19}$$

Simplifying, $A^* = \ell_S b$. This means that the length scale parameter, ℓ_S, is 19.2 nm, or 50*b*. In the case of the aforementioned 320 nm sphere this would fix γ at 0.06. Additionally, it has previously been determined that, for $k_y \cong 1\,\mathrm{MPa\cdot m^{1/2}}$, $\chi\gamma$ = 17.8 above. Given this assignment, a value of $\chi = 17.8/0.06 = 297$ results. For $\ell_S = 19.2\,\mathrm{nm}$, an activation area of, $A^* = \ell_S b = 7.4\times10^{-18}\,\mathrm{m}^2$, is calculated. The contact area for this 320 nm sphere, considering both the top, and bottom, for a displacement of 44 nm is $4\times10^{-15}\,\mathrm{m}^2$. For an activation area of approximately 7.4 $\times10^{-18}$ m^2, there could be as many as 540 total sites, or 270 each at the top and bottom. This implies approximately a 16 by 16 array of sources at each contact. Each site would then be (for $2a \sim 160$ nm) about 10 nm $\times$10 nm in size. If dislocations are spaced, on average, to be 10 nm, for Taylor hardening, this would give $\sigma_y = \alpha E b\sqrt{x} \approx 3\,\mathrm{GPa}$ with a value of α of about 0.5. This appears to be of the correct order as $V^* = b^2\ell_s$ since for $\ell_s \sim$ 10 nm, $V^* = 26b^3$. This is within a factor of 2 of that from Eq. 5.18. Such deviations are not surprising given the number of approximations required.

With $\chi\gamma$ defined, it is possible to use Eq. 5.17 to compare the strain-hardening result for the deformed spheres. However, the cylinders represent a different geometrical case. Similar to the spheres, it is assumed that the number of dislocation nucleation sites increases with plastic strain, but with a different functionality. Rather than the contact area, A_O, at the top and bottom of the pillar increasing with displacement as for spheres, here it remains nearly constant. Still, as plastic strain increases and more dislocations are generated, the number of sources would increase. It is assumed that due to the contact area dominance for spheres being weaker in pillars, this leads to a smaller dependence on strain. This gives the available area for nucleation to be

$$A_{av} = A_O\,\varepsilon^{1/2} = \frac{\pi d^2}{2}\,\varepsilon^{1/2} \qquad \text{Eq. 5.20}$$

for a square-root strain dependence and the original contact area of $\frac{\pi d^2}{4}$ existing at both the top and bottom of the pillar. The increase in available area is partially due to internal

sites. As before it is assumed that the strain-hardening exponent is proportional to the rate of increase of available area giving

$$n \propto \frac{d\,A_{av}}{d\,\varepsilon} = \frac{\pi\,d^2}{2\varepsilon^{1/2}} \quad . \qquad \text{Eq. 5.21}$$

Within this area there are a number of individual nucleation sites of area $\chi b \ell_S$, such that the number of surface sites plus those sites that are internally generated per unit area becomes $A_{av}/\chi b \ell_S$. For increasing normalized stress, Eq 5.14, and a stress dependence of $k_y d^{-1/2} \cos\phi \cos\lambda$, Eq 5.21 becomes

$$n = \frac{\pi k_y\, d^{-1/2} \cos\phi \cos\lambda\, d^2}{2\chi \ell_S b \mu \varepsilon^{1/2}} \quad . \qquad \text{Eq. 5.22}$$

Again, taking $\ell_S = \gamma d$ and following the same approach as for spheres, one finds

$$n = \frac{\pi k_y\, d^{1/2} \cos\phi \cos\lambda}{4\chi \gamma \mu b \varepsilon^{1/2}} \qquad \text{Eq. 5.23}$$

What is missing here is that much larger volumes exist for a given pillar diameter compared to a sphere. As a result, even under high stresses, there are large spacings between dislocations. As such, the available area for dislocation nucleation shifts away from the pillar top and bottom. For a volume in center of the pillar at least four times larger than a corresponding diameter sphere, one *could* modify Eq. 5.16 to

$$n = \frac{\pi k_y\, d^{1/2} \cos\phi \cos\lambda}{16\chi \gamma \mu b\, \varepsilon^{1/2}} \quad . \qquad \text{Eq. 5.24}$$

This is clearly speculative but could account for the much smaller strain-hardening exponents in the pillars due to the lower confinement in the deforming volume. While the evidence for such an ad hoc assessment of strain-hardening is weak for the single crystal silicon pillars evaluated to date, there is some evidence for larger diameter pillars of MgO.[221, 222] For $\langle 111 \rangle$ oriented single crystal MgO, Korte and Clegg[221, 222] evaluated the stress-strain response of 0.5, 2, and 5 μm pillars. Their respective yield strengths were

5.4, 4.5, and 3.6 GPa. The conventional stress-strain response could be converted to true-stress, true-strain using strains in the vicinity of 0.06 ± 0.04, figure 5.10.

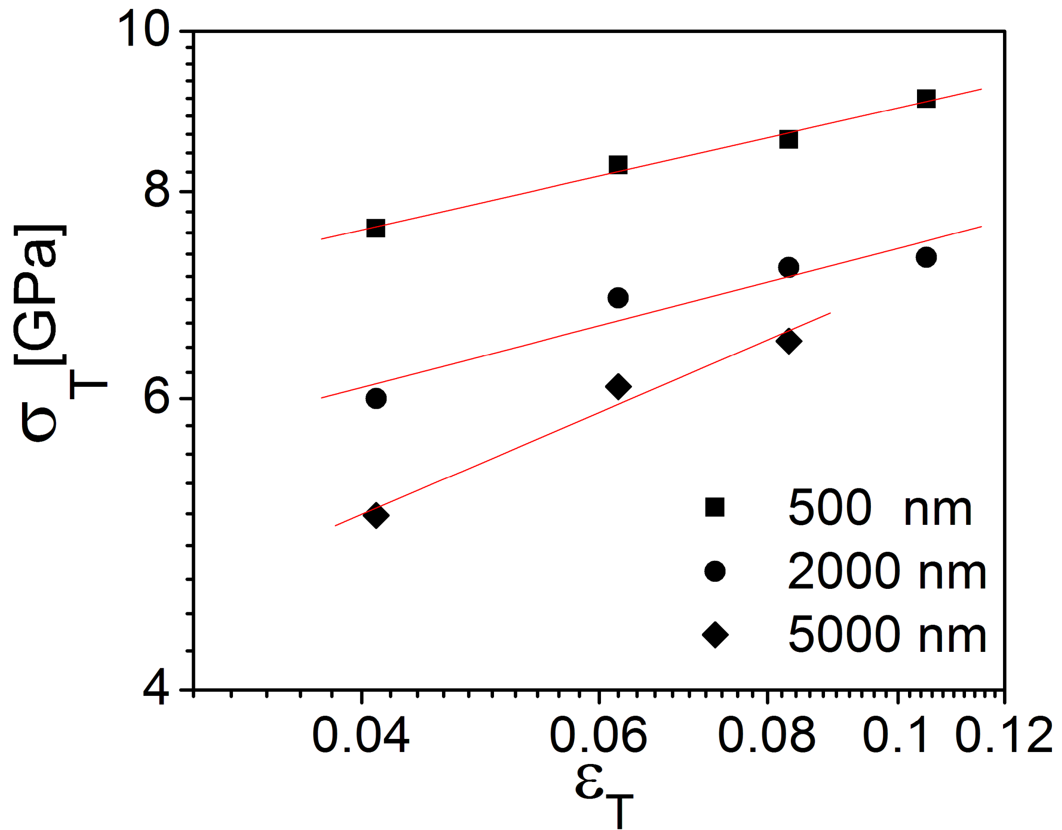

Figure 5.10. True stress – true strain plots for the <111> MgO pillars of Korte, et al,[221, 222] showing a size dependence on the strain-hardening exponent.

As seen in figure 5.11, the strain-hardening exponent nearly doubled from about 0.2 to 0.4 while the parameter $\left(d/\bar{\varepsilon}\right)^{1/2}$ increased by a factor of three. The dependence on size appeared to be less than suggested by Eqs. 5.10 and 5.14, but qualitatively trends in the correct direction.

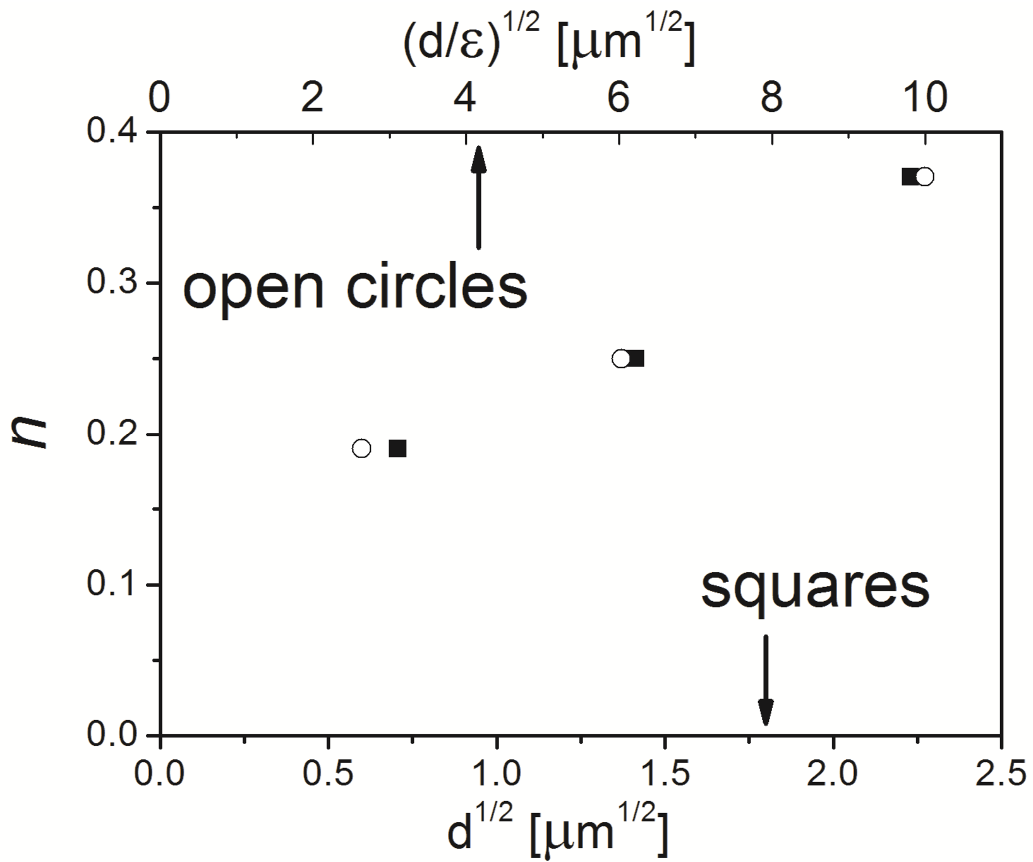

Figure 5.11. Strain-hardening exponents, calculated from the plot of figure 5.10. The strain-hardening exponent is related to the ratio of the root pillar diameter to the strain (open circles) as suggested by Eq.(13). However, for similar strains, the strain-hardening exponent is proportional to the root of the diameter (filled squares).

5.6. Discussion of the results using the proposed model

What has been considered here is the strain-hardening induced by the compression of small spheres or pillars of silicon. The *in situ* TEM method analogous to those pioneered by others,[115-118, 121, 222, 223] has allowed the true stress-true strain behavior to be reasonably averaged in nanospheres, and more accurately determined in nanopillars. Here, we compare the experimental results to the proposed first order model as detailed in the previous section. It is emphasized here that such models, dependent upon surface mediated dislocation nucleation, are appropriate to relatively dislocation free nanovolumes as is the case for these silicon single crystals. For larger volumes where

initial internal multiplication sites are operational, these approaches would need to be modified.

Given the two proposed methods for analyzing average stress and strain in spheres under compression, §5.2.1.1 and 5.2.1.2, it is first important to demonstrate the differences produced regarding strain-hardening exponents. Qualitatively the stress-strain plots of the *in situ* compressed spheres appear similar in figures. 5.6 and 5.7. A comparison of the harmonic mean and right cylinder methods can then be detailed by plotting the strain-hardening exponents, from table 5.2, as shown in figure 5.12.

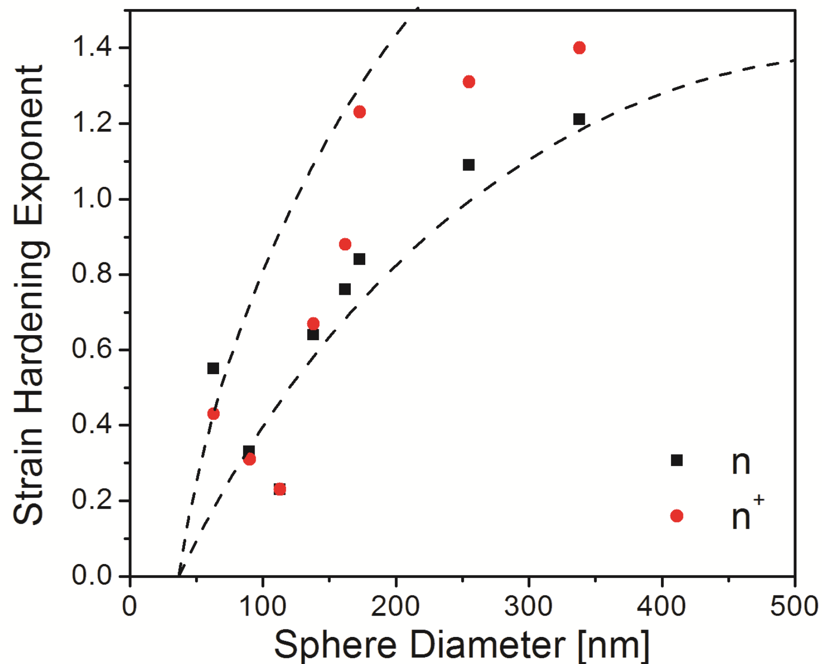

Figure 5.12. Strain-hardening exponent for the Si spheres, plotted versus the sphere diameter. Values calculated by the right cylinder approximation (squares) are smaller than those using the harmonic mean approximation (circles), especially for larger diameters. Dashed lines are provided as guides to the trend are based on Eq.(12) using large variations in $\cos\phi\cos\lambda$.

For both approaches, there is a strong increase in strain-hardening exponent with increasing sphere diameter. Both the right cylinder averages and harmonic mean approach gave similar results for spheres less than 150 nm in diameter but the latter consistently gave higher strain-hardening exponents at larger diameters. As the right

cylinder approach was easier to justify, and the two methods gave reasonably similar results, further analysis used the simpler right cylinder method.

First, the increase in strain-hardening exponent with increasing diameter is qualitatively addressed. For both sets of sphere data, from tables 5.1 and 5.2, there is a strong increase in n with sphere diameter except for two data points in figure 5.13.

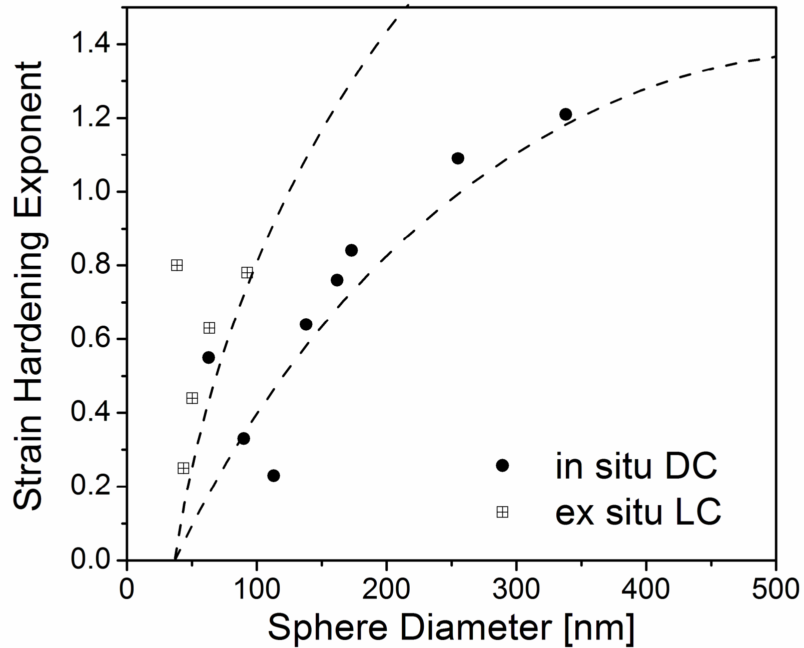

Figure 5.13. Comparing load – controlled (LC) tested sphere to (DC) tested spheres, the strain-hardening exponents for the LC data trend higher than the largest value of the two $\cos\phi\cos\lambda$ plots of Eq.(12), reproduced from figure 5.12.

The increase is considered to be due to an increase in dislocation nucleation rate in the larger spheres, as seen in the size dependence of Eq. 5.16. One must consider that since the activation area bears an inverse relationship to the applied stress, more nucleation sites become available at higher stresses. These stresses should increase for the smaller spheres. However, these sources are rapidly exhausted in small spheres and the further rate of hardening is much less. This is exacerbated by the confinement represented by the smaller spheres. For smaller diameters, the mean free path of dislocations is decreased due to the back stress from dislocation - dislocation interactions (Eqs. 4.8, 4.14). This prevents further nucleation in the smaller spheres. It is proposed that a combination of

surface-mediated dislocation nucleation and confinement leads to smaller increases in dislocation densities per unit strain and hence lower strain hardening exponents. Clearly, the confinement is less in larger spheres and coupled with increased contact area, the potential for the activation of large numbers of dislocation sources can result at larger strains. As stated previously, this is somewhat offset by the elevated flow stresses in small spheres which facilitate nucleation at potential sites within the contact area. Both of these features are embodied in Eq. 5.16, which includes the cut-off diameter.

Additionally, figure 5.13 shows that the strain-hardening exponents, nominally bounded by the shear stress values of the Schmid factor, $\cos\phi\cos\lambda$, based on {111} slip and compression orientations of either $\langle 100 \rangle$ or $\langle 111 \rangle$, show a discrepancy between the two types of feedback operation. Here the displacement control data favors a theoretical fit of $\cos\phi\cos\lambda = 0.408$ and the load control data favors a fit with $\cos\phi\cos\lambda = 0.272$. This is fortuitous, however, as the loading axis for all of these spheres is unknown. Additionally, as discussed in chapter 3, dislocation velocities can be increased by the presence of a high voltage electron beam by the addition of energy to overcome the Peierls barrier. While the LC indents were performed in an AFM based system, the DC compressions were carried out in the 120keV microscope, with varying amounts of beam current. However, beam exposure fails to provide an explanation for the "open loop" (no feedback) compression of the *in situ* 63 nm diameter sphere, which appears to better match the load control data. Whether these two separate data groupings are due to some fundamental condition associated with feedback control or drift, is a consideration for the future work.

The data of table 5.3, and figures 5.6 and 5.7 for pillars, are not as reliable due to the relatively smaller strain ranges available prior to bending or buckling. This was particularly obvious in the smallest diameter pillars where bend contours were clearly observed concomitant with dislocations and permanent strain upon unloading, as discussed extensively in chapter 4. It is strongly suggested that this compromised the data to some degree and that the strain-hardening exponents reported for the 160 and 200 nm diameter pillars are inaccurate. Still, the stresses for these two smallest diameter pillars are consistent with the same size scale diameter spheres, e.g. ~ 3 GPa. Because of

prior bending in the previous runs, stresses to achieve the same five percent strain progressively decreased from 4.5 to 3.3 GPa. This could result in very high apparent strain-hardening exponents due to predominantly elastic stress-strain behavior with small elastic-plastic bending strains superimposed. This would cause the elastic response (n = 1) to give somewhat smaller values of strain-hardening due to large compressive stress but larger than normal compressive plus bending strains ($n < 1$). Note that the aspect ratio, height to diameter, was closer to 7:1 for these small diameter pillars. For reliable measures of strain-hardening, additional experiments will be required for aspect ratios closer to 3:1, which reduces the likelihood of buckling.[33] There are literature data for pillars of this aspect ratio on somewhat larger MgO single crystals. As shown in figure 5.11, n values ranged from 0.2 to 0.4, consistent with the reported measurements here for larger diameter silicon nanopillars. For the four larger diameter pillars with smaller aspect ratios, i.e. the FIB cut pillars, the bending is sufficiently suppressed that reasonable strain-hardening exponents of 0.3 $\pm$ 0.08 are found for the two pillar orientations of $\langle 100 \rangle$ and $\langle 111 \rangle$. As the average pillar size was 380 nm, this result compares to a measured strain-hardening exponent of greater than unity for a corresponding diameter sphere. This may be qualitatively understood considering the relative confinement and increased dislocation activity for the sphere compared to the pillar, as proposed in Eq. 5.24. An idealized rendition is shown, figure 5..14, for a single type of slip system to illustrate the potential.

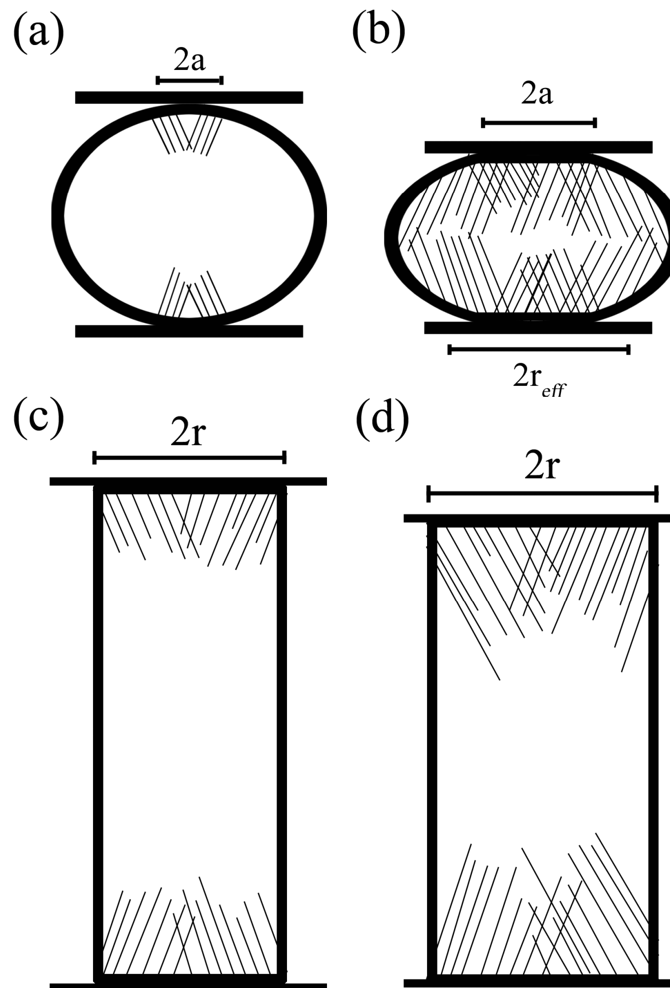

Figure 5.14. Idealized schematic of plasticity in compressed spheres and pillars. **(a)** At small strains, there is dislocation interaction only near the contact for a sphere, but at larger strains, **(b)**, the dislocation structure interacts in the entire sphere. This can be contrasted to **(c, d)** where in a pillar the dislocation structure needs to propagate further for increased work hardening.

At ~10 percent strain similar stresses might be produced in both the sphere and pillar of equal diameters. However, at larger strains, for large numbers of dislocations moving sufficient distances to give 20 percent strain, slip planes would have to be closer together in the sphere. This would require larger applied shear stresses as discussed elsewhere.[224] Additionally, there would be larger interaction stresses and commensurate back forces leading to higher stresses within the spheres. This high dislocation density also increases

the potential for locks and internal dislocation sources. Therefore, it is not surprising that the very large strain-hardening exponents estimated in the spheres are considerably greater than for the pillars.

How do these differences compare to what might be expected from Eqs. 5.15-5.17? The average strain for the four largest samples is 0.109 giving $\varepsilon^{1/2}$ of 0.33. Since $4\varepsilon^{1/2}$ is little different from unity it appears that the strain-hardening exponent for comparable diameter pillars could be nearly a factor of four smaller than the spheres as observed for the 300-400 nm size range. Note that this would be for pillars with a 4:1 aspect ratio. The assumption here is that $\chi\gamma$ for the two geometries is essentially the same. Also, because of some ad hoc assumptions regarding the assignment of dislocation nucleation areas, one must consider the modeling, especially for pillars, as a working hypothesis.

5.7. Phase transformations in silicon

Finally, it is probable in some of the larger spheres, but not the pillars to have the diamond cubic to β-Sn (Silicon $1 \rightarrow$ II) phase transformation occur on loading. This usually manifests itself by a pop-in (loading) or pop-out, or knee in the load-displacement curve (unloading).[56, 225, 226] Such a result for a 212 nm diameter sphere is shown in figure 5.15. Maximum compressive stresses in the pillars were 4 GPa, one third that reported for the β-Sn transformation.

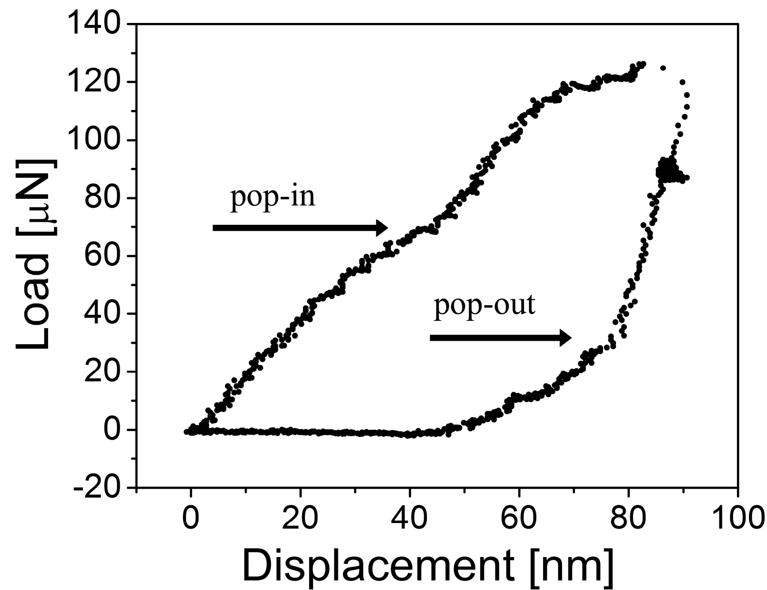

Figure 5.15. For an *in situ* loaded sphere, evidence of a phase transition can be seen in the unloading elbow, or "pop-out". This unloading feature is consistent with a reverse phase transition from the high pressure β-Sn phase to the low pressure amorphous, Si-I, and Si-II phases. The amount of phase transformed region would be small. Data courtesy of Dr. Aaron Beaber.

Here, it is seen in that both pop-in and pop-out occur on loading and unloading. From measurements of the sphere height, both post and pre-compression, it was found that the residual strain was no more than 4.8% strain, even though the hysteresis in the load – depth curve would imply much more. One may conclude that there is reverse dislocation plasticity or a new phase transformation upon unloading restoring part of the deformed volume. Beaber, et al, show, in an as yet unpublished study of nano- and submicron-spheres, that there is a size transition in behavior from deformation of microspheres to nanospheres.[227] In this work, large spheres exhibit these pop-out events, while spheres of less than 100 nm in diameter do not.

At much larger Vickers indentations, others have shown there is little or no plastic deformation below 500ºC.[164] This may be due to the triaxial stress state. However, this is not an issue for the small sphere volumes where state of stress and length scale allows

dislocation plasticity prior to fracture, as discussed in chapter 4. Perhaps appropriate to this study, Gogotsi, et al. suggest that "indentation-induced metallization (Silicon II) . . . . is accompanied by confined plastic flow . . . . in order to partially accommodate high strains in the surrounding material."[228] Future work should address whether it is dislocation plasticity, phase transformation or a combination of the two which results in the large jump in strain-hardening exponent in the 100-150 nm diameter regime. Irrespective of the relative hardness between the Si I and Si II phases, the transformation and/or its interface could easily act as dislocation generation sites. If the latter, this would require additional interpretation of Eq. 5.16 to include dislocation nucleation at both surface and internal interfaces.

One remaining issue is the unanticipated strain hardening exponents near unity. Such linearity between stress and strain is normally only expected for elastic behavior. Clearly strains are well beyond the elastic regime because of the large residual displacements observed. For typical examples of both load-controlled and displacement-controlled data, plots using a linear scale produce linear loading slopes. However, the tangent moduli were only 100 GPa and 10 GPa for the smaller and larger spheres respectively. These are still large compared to expectations, since previous data by Rabier at 425°C for GaAs only gave work hardening rates of 6.9 GPa.[171] Two points are important. First, due to high energy dislocation arrangements, one might expect this silicon data to have higher strain-hardening rates than the more low energy dislocation structures which might occur at 425°C for GaAs. Second, as the pressures are very high in these compressed spheres, one might also expect that as the pressure increased that the flow stress would increase. This is due to the elastic moduli increasing under pressure, as observed in the Murnaghan equation of state.[229] As a result, an increase in the elastic stiffness tensor would lead to greater Peierls barriers for dislocation nucleation and motion.

5.8. Summary

Experimentally, deformation of single crystal silicon nanospheres and sub-micron pillars has been measured in compression. These exhibit considerable plasticity with plastic strains approaching 0.5 for spheres. As observed by transmission electron and atomic force microscopy with *in situ* loading devices, considerable strain-hardening is observed as well. Strain-hardening exponents ranging from 0.2 to unity are observed with a size scale dependence which increases with diameter. For a given diameter in the range of 200-400 nm, spheres have a hardening exponent approximately three times larger than pillars with a 4:1 aspect ratio. Theoretical considerations find that the strain-hardening exponent increases approximately as the square-root of the sample diameter. Arguments based on both relative contact areas and confinement suggest a milder dependence for nanopillars compared to nanospheres. The latter are significantly more constrained than pillars leading to strain-hardening exponents increasing to near unity for single crystal silicon.

Chapter 6. Future Directions

6.1. Introduction

In the previous chapters the improved mechanical properties of so-called "brittle" materials, such as thin oxides of alumina and chromia, and sub-300 nm single crystal silicon spheres and pillars has been demonstrated. For example, such nanostructures can withstand large strains prior to fracture. The ability of single crystal silicon to accommodate dislocations *at room temperature* and then strain harden is quite remarkable. However, the size effects for both classes of materials, native oxides and silicon, have not been fully explored. Additionally, the combination of the two *in situ* techniques, electrical contact indentation and TEM indentation, has the potential to be a powerful analytical tool. This chapter deals with future directions for this work, with some preliminary data. Additionally, potential experiments for the application of room temperature plasticity in other important brittle materials are proposed, using geological materials.

6.2. Further exploration of fracture in aluminum thin films

6.2.1. Grain size effects

Surprisingly, no correlation between film thickness and depth of delamination measured by conductance was found in the plastically constrained Al_2O_3/Al/Si_xN_y/SiO2/Si multilayer films. In these film systems, initial calculations suggested that the plastic constraint from the Si_xN_y underlayer would likely cause excessive stress in the Al and native oxide layers. However, this may be due to the low modulus found in the amorphous Si_xN_y layer, only 100 GPa near the surface. The sharp indenter used to deform this system had a contact radius on the order of the surface roughness wavelength. For this case, it is possible that the data scatter could be caused by the variation in the number of grains being sampled. It is easy to conceive, that with these grain sizes, from 63 to 215 nm depending on film thickness, perhaps 1, 2, or 3 grains might be sampled at a time. Indentation of films with the roughness wavelength

either much greater or much less than the contact diameter is needed. Additionally, decreasing the grain size will increase the hardness of the film, by the classic Hall-Petch mechanism. This could further enhance the plastic constraint, relieving the requirement for a plastically constraining underlayer. The grain size, for all thickness of films, can be controlled by varying the deposition rate parameters. Increasing the deposition rate causes a corresponding decrease in the grain size, and increase in roughness. Decreased grain size and increased roughness would make it more likely that several asperities will be contacted for each indentation, likely increasing the likelihood of oxide failure.

6.2.2. Elastic constraint

So far, the plastically constrained films showed no reliability enhancement, with regard to failure of the oxide. They typically fractured at depths very similar to the non-plastically constrained film. FilmDoctor simulations show that the pressure effects in the system would be more likely to be enhanced for substrates with very high moduli. Replacing the Si silicon, 160 GPa, with a MgO substrate, 290 GPa, would increase the elastic constraint in the film. The MgO/Al interface is also strongly adhered, decreasing the chances of any delamination events.

6.2.3. Characterizing fracture *ex situ*

Much of the work in the Al film systems of chapter 2 would be more fully supported with data explaining the extent of fracture, and whether fracture may have occurred away from the contact. As was seen in the FilmDoctor simulation of figure 2.20, the deformation of a rough surface can cause large elastic stresses in neighboring hillocks. As these hillocks are related to the grains in these films, where the grain boundaries act as stress concentration points, fracture could potentially occur away from the contact. This fracture would not be detected in the current ECR test set-up, even if contact were just outside the contact, as the oxidation of the Al metal is extremely rapid.

This would require the ability to image these fractures at the surface. Initial attempts, using both AFM and SEM, were unable to discern where the cracking had occurred. Scans by AFM showed significant pile-up at the contact, and cracking was obscured. However, if a means of detecting changes in the oxidation existed, from that in the controlled oxidation of pure O_2 in the growth chamber as described in chapter 2 to the rapid oxidation in air, the type and extent of fracture could be analyzed.

Kelvin probe microscopy (see Nonnenmacher, et al..[230] for more details) is a variation of non-contact AFM, where the cantilever is driven away from resonance by means of a lock-in amplifier, at constant distance from the sample. The potential difference between the reference electrode, typically a Pt coated Si tip, and the sample can then be measured accurately, typically on the order of 5 mV.[231]

Preliminary experiments on Cr films, where the film had been indented to 5gf using a Beuhler Micromet with a Vickers tip, showed that work function differences in the material could be measured in plastically deformed regions, figure 6.1.

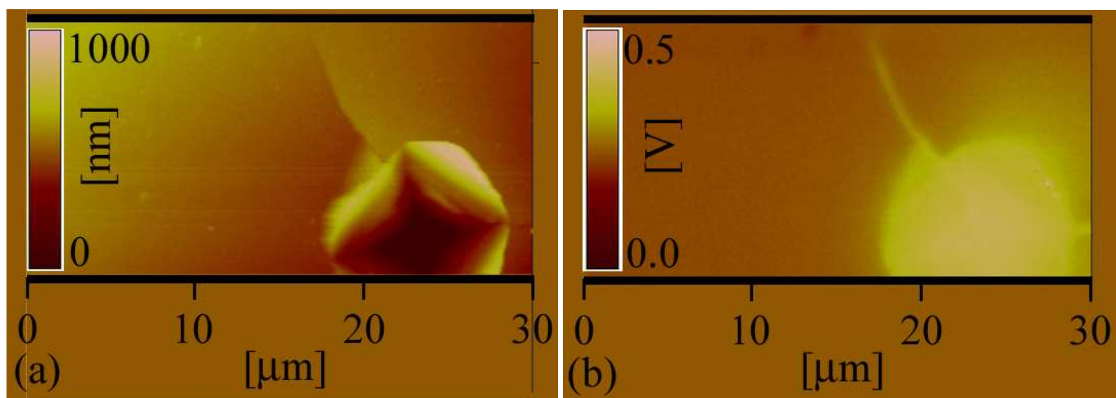

Figure 6.1.(a) Microindentation performed on a 100 nm Cr film, indicates large pile-up and plastic deformation, as expected. **(b)** Work function differences are also seen as the scan transitions from undamaged to the plastically damaged region, indicated by changes in potential with respect to the Pt tip. The 130mV increase in voltage implies a decrease in the work function of the material. Scans were performed in collaboration with David Ellison.

While this method would not be able to detect fracture inside the pile-up region, by placing very shallow indents in the material, the possibility of fracture away from the plastically deformed area could be probed. For a crack running through the film, likely

due to substrate cracking, figure 6.2, the plastic damage at the crack edge also causes a change in the work function difference.

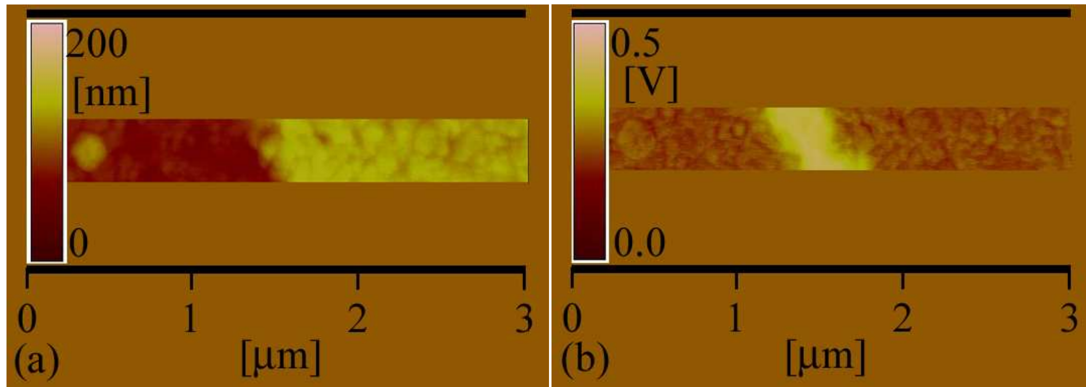

Figure 6.2. Higher resolution scans of the radial cracks seen in figure 6.1 **(a)** The cracking in the the substrate propagates to the surface, when indented to high loads causing a height difference on either side of the crack. **(b)** The potential voltage difference between the peak of where KFM shows a work function difference of 158mV only in the damaged region.

In the potential scan image of figure 6.2, it can be seen that the 158mV increase in potential is found only at the crack itself, not over the area where the film has been lifted. This is contrast to the height images, which shows that the surface to the right of the crack has been elevated. While these work function differences may also be due to the extent of the plasticity in the metal film, this usually has the effect of increasing the work function, not decreasing it. A decrease in the work function could possibly be due to increased oxygen vacancies in the oxide layer. To test this theory, additional Al films could be grown, and then rapidly oxidized in air, and compared to the controlled oxidation in the growth chamber. From this, the possibility of precisely locating film cracking and plastic deformation could be useful for *ex situ* investigation.

6.3. Electrical contact for film delamination

Flexible electronics, including amorphous solar cells, touch screens, and next generation robot tactile sensitive skin all rely on reliable "soft" film systems. However, when coupled to more conventional electronics these devices often fail at the soft film/metal interconnect or soft film/semiconductor interface.[232-234]

A well-defined procedure for the mechanical testing of adhesion exists for the typical ductile metal films on hard substrates and hard film / hard substrates, such as W and Cu multilayers on Si.[235] This procedure calculates the buckling stress, σ_B, of surface debonding during indentation as;[236]

$$\sigma_B = \frac{\mu^2 E}{12(1-\nu^2)}\left(\frac{t}{c}\right)^2 , \qquad \text{Eq. 6.1}$$

where E and v are the Young's modulus and Poisson's ratio of the film, t, is the film thickness, μ is a geometric prefactor, and c is the radius of the film blister (figure 6.3). The film constants are typically determined from nanoindentation, and c can be measured *ex situ* by light microscopy or AFM. However, the geometric prefactor, μ, requires more specific knowledge of the loading conditions at the time of failure. In the case of a metal film debonding from a semiconductor substrate, the loading at time of failure is often seen in discontinuities in the indentation load-depth profile, such as large increases in depth without an increase in load. Hard films which debond on unloading can be modeled as a circular blister with $\mu = 14.68$ (figure 6.3a).[237] Films which debond on loading are typically modeled as pinned annuli, (figure 6.3b) with $\mu = 42.67$. These are often referred to as (a) single buckling, and (b) double buckling.

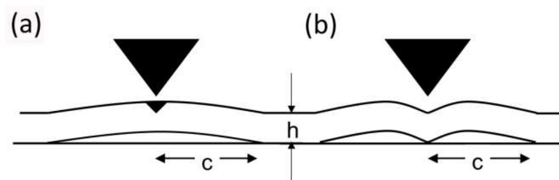

Figure 6.3.(a) An unpinned circular blister, where the film bebonds on unloading, and **(b)** a pinned blister where debonding has occurred during loading. Adapted from Cordill et al.[237]

In the case of hard films on soft substrates, such as W on PMMA, there are no discontinuities in the load-depth profile, and as such the loading conditions at failure are not known. This complicates the testing procedures. Here, a simple system is proposed for the testing of adhesion model for W films on poly- (methyl methacrylate) (PMMA) using conductive nanoindentation. Initial tests on metal films/hard substrates with low adhesion, such as copper on silicon, show significant increases in conductance on unloading. Using the Maxwell model for conductance, Eq. 1.27, repeated here for clarity

$$G = \frac{d}{\rho} \quad , \qquad \textit{Eq. 1.27}$$

it can be seen that any large increases in G on the *unloading* would likely be due to an increased contact area and not oxide fracture. As the film delaminates from the substrate it can be understood that the area of the film/tip contact would increase for either 6.3(a) or 6.3(b). For metals with an oxide film, increases in G during the loading period could be a result of either oxide failure, as in the case of Al, or debonding of the film. Determinations of delamination would need to be made *ex situ* in this case. KFM, described in §6.1.3 of this chapter, would be a good candidate for this. Polycrystalline Cu films have been well-documented regarding delamination, and typically lose adherence during the unloading segment. Here, in 100 nm thick Cu films, grown directly on a Si substrate, a large current spike can be seen during the unloading segment after being indented to a displacement of 75 nm, figure 6.4.

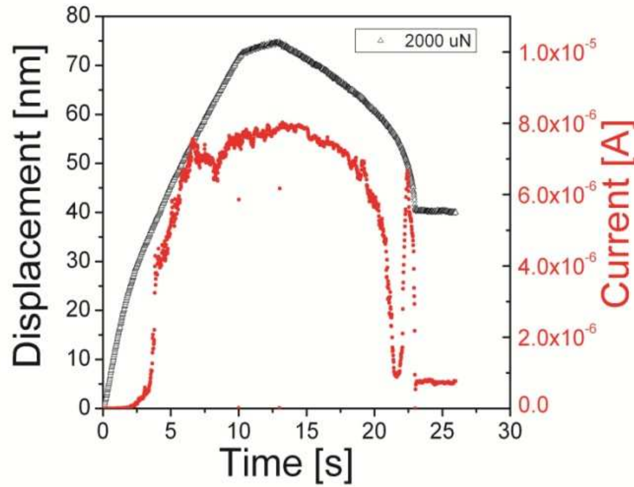

Figure 6.4. A plot of displacement (dark triangles) and current (red circles) versus time shows that a large spike in the current occurs during unloading in 100 nm Cu films.

The extent of delamination can be determined from the ratio of the buckle radius, c, to the contact diameter, a. For delamination, the ratio $\frac{c}{a}$ should be larger than 3, with larger ratios indicating a greater extent of delamination. For the indent of figure 6.4, the ratio, $\frac{c}{a}$ was determined by post-indentation scanning with the indenter probe to be 3.4, which indicates that the buckling was not extensive. The use of a sharp indenter would have been more appropriate for these experiments, but for testing the delamination of films on soft substrates, a large radius sphere would be more appropriate to avoid fracture of the film or substrate. Using a simple system, such as W on PMMA, which has already been extensively studied,[234] would provide a benchmark for testing other film/substrate systems.

6.4. Deformation in iron oxides by conductive indentation

The earth minerals wüstite, magnetite, martite, hematite, and maghemite, while making up an extremely small fraction of the Earth's crust, make up the majority of the mixture known as "rust". However, these materials have not been thoroughly explored

with regard to length scale phenomena. Films of Fe, of thickness 34, 54, and 85 nm have been grown in the same chamber as the aluminum multilayers discussed in chapter 3, with at ambient temperature, at 2.4±0.1 mTorr of Ar, at a rate of 0.6Å/s. These Fe films were then capped with an alumina layer to prevent oxidation. The Fe films are epitaxial, having no observable grain boundaries in a 5μm scan, and are very flat, with an rms roughness of 0.6 nm. As the effect of the thin alumina scale on aluminum has been explored, the properties of the Fe films can then be investigated. After analysis of the single crystal Fe, an examination of films of magnetite on Fe can be made. These magnetite films, deposited at 400°C, at 20.0 mTorr of Ar with 0.5 mTorr of oxygen at a rate of 0.45 Å/s, are grown directly on freshly sputtered Fe films under the conditions just described. The magnetite grows epitaxially on the Fe, with the rms roughness increasing slightly to 0.9 nm.

The mechanical properties, primarily hardness and modulus, of magnetite can then be investigated by conventional nanoindentation.

Additionally, further experiments on the fracture properties of the alumina cap can be probed, where the underlying elastic and plastic constraints has been varied.

6.5. Determination of dislocation identity in compressed silicon.

Despite the efforts of chapter 4, which showed that the dislocations caused post-compression bending in the pillars, two issues remain. One, the type of dislocation was not identified, and two the large strain gradients present from pillar bending were not eliminated. These failures are mostly due to a failure of geometry. For determining the dislocations type, the thin pillars bonded to the substrate present major imaging constraints. Also, all pillars showed some evidence of bending contours during *in situ* compression, even when the P-δ curves were straight. Recent work from the Michler group show that the plastic response of compressed silicon does not change as a single dimension increases in length.[238] Thus, thin “walls” of silicon also exhibit plasticity. This can also be seen in the initial work of Stach, et al, for the indentation of the wedge-plateaus used as sample substrates in chapter 3.[141] Further increasing the height of these

pillars, thin walls could then be created by either focus ion beam (FIB), or further wet etching. One must be careful that the width of the wall does not become too wide, or bending will occur, as seen by Stach.[120] If walls less than 1μm in height and width, and less than 100 nm in thickness were FIB milled, this could provide a stable platform for indentation. Additionally, it would provide a foil thin enough for dislocation determination by the $g \bullet b \times u$ or weak beam methods discussed in chapter 4. Another means of preparing a thin foil is the use of the tripod polisher, followed by FIB milling, as was done on the olivine sample in chapter 3. By FIB milling and annealing the final sample, the initial dislocation density should be low, and therefore the nucleation and determination of dislocations should be similar to that of the single crystal pillars. These thin walls will then be indented using an indenter with a sharp radius of curvature, and large angle, such as a cube corner, to avoid hitting the supporting structure during the *in situ* indentation.

6.6. Application to geological materials

Olivine is a magnesium iron silicate that makes up approximately 80% of the Earth's mantle by volume. Like silicon, olivine shows very little evidence of plasticity at room temperature in bulk samples, figure 6.5, but could possibly show a length scale brittle to ductile transition. Thus far, sample geometry had been an issue as the samples were initially 1mm^3 single crystals, but the development of the tripod polishing/FIB finishing scheme outlined in chapter 3 has alleviated these issues. This development was followed by the failure of the temperature controlled *in situ* indenter that was on loan through a collaboration with Dr. Ryan Major from Hysitron, Inc. The controller is capable of heating and electrical contact during *in situ* indentation, and due to geometry constraints on the holder is designed only for Jeol microscopes Activation energies for dislocation motion in constant thickness FIB milled "thin foil" samples could be measurable, by controlling both temperature and stress.

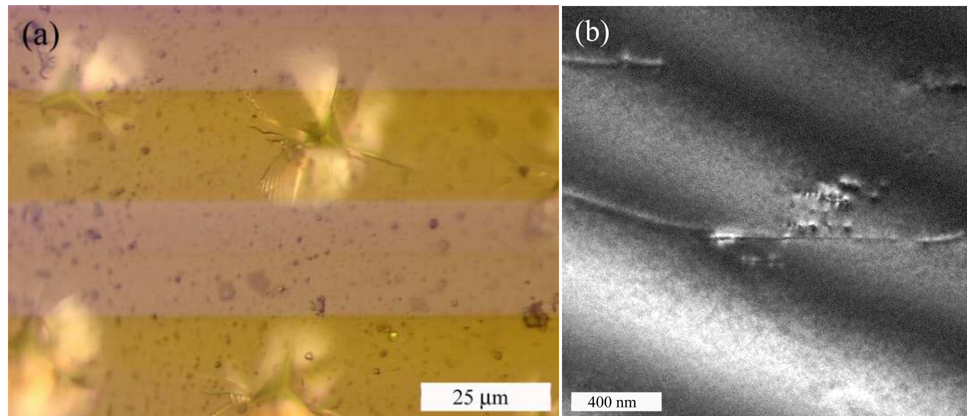

Figure 6.5.(a) Optical images of radial cracks emanating from the corners of indents on the (0001) face of single crystal olivine. **(b)** Dark field micrograh of a FIB lift-out of a region near a crack tip in single crystal olivine, showing that even near a crack tip there are few dislocations. Samples are courtesy Professor David Kohlstedt, while the TEM micrograph is courtesy Dr. Ozan Ugurlu. Diffraction data was not available.

6.7. Combining the two *in situ* techniques

The combination of both electrical contact and *in situ* TEM compression has been the ultimate goal of this research. This became a possibility using the prototype holder, described briefly in §6.5, which was available for the proof of concept experiments described below. However, during the availability of the prototype indenter, the video capture system on the 100keV Jeol 1210 was not operational. Therefore, no videos were taken during the compression. Compression tests were performed on n-doped VLS grown Si wires grown by the Davydov group at NIST. Pillar diameters were sharply distributed, ranging only from 120 to 140 nm. Heights were more variable, from 600 to 1000 nm. Again, for these CVD pillars, no Au caps were present. However, unlike the samples tested in chapter 4, the tops of these doped pillars were rounded, figure 6.6.

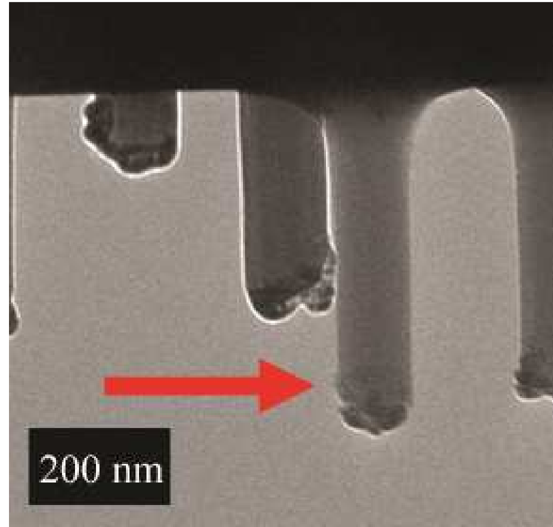

Figure 6.6.(a) Micrograph taken with Jeol 1210 at 100keV, showing a pillar, indicated by red arrow, prior to being compressed.

Indents with a 5 s load segment, 3 s hold, and 5 s unload to a nominal displacement of 80 nm were run. The nominal displacement can be defined as 80 nm from the position of the indenter at the start of the run, to the maximum displacement at the hold. As indents were performed with the tip out of contact, the actual displacement is always less than the nominal displacement. Typical displacements in contact were on the order of 20 to 40 nm. The tip used was the carbide of the type discussed in chapter 2, which had been machined as a flat punch. The applied bias was 10 mV during the load and unloading segments, while during the hold segment, the bias was swept from -10 mV to + 10 mV, and then back to over the entirety of the sweep period.

Initial results show that as the tip comes into contact, the measured conductance decreases, figure 6.7(a). This is likely a result of the work function differences in the two materials, although this would need to be verified, likely with KFM. The I-V sweep suggests Ohmic behavior, figure 6.7(b), although this cannot be verified, as the applied bias range is very low.

Using the measured I-V sweep to calculate the resistance, roughly 800kΩ by linear fit, and knowing the length, l, and cross-sectional area, *A,* of the pillar from the TEM micrographs, the resistivity, ρ, of the pillar was found to by,

$$\rho = \frac{RA}{l} \quad \text{Eq. 6.2}$$

to be $1.5\,\Omega\cdot\text{cm}$. Initially, the contact resistance is neglected, but this can then be iterated knowing that the tip/sample contact resistance is in series with the resistance of the pillar. This converges for a tip/sample contact resistance of 109kΩ, and a sample resistivity of $1.3\,\Omega\cdot\text{cm}$, consistent with a roughly 10^{16} cm^{-3} doping level. The actual doping level is not known. The assumptions here are that the substrate does not significantly contribute to the resistance in the two-point measurement, and that the beam effects are negligible, which at this point are both broad assumptions. To test the assumption that the beam had no effect, sweeps were ran out of contact with the pillar, showing several orders of magnitude less current, effectively flat for the entire bias region. However, the conductance here is *i)* increasingly negative, giving credence to an argument regarding differences in work function between the tip and the sample, and *ii)* increases linearly with displacement.

The effect is repeatable, in that further indents on the same pillar gave near identical results. No gross bending was seen during visual observation of the pillars under load. Likewise, no plasticity in the body of the pillar was evident after deformation. Nevertheless, residual plasticity is seen in the load-depth curve, figure 6.7(a). This is like due to the high stresses at the rounded tip, which were observed to be compressed. These are interesting results, which are worth further inquiry.

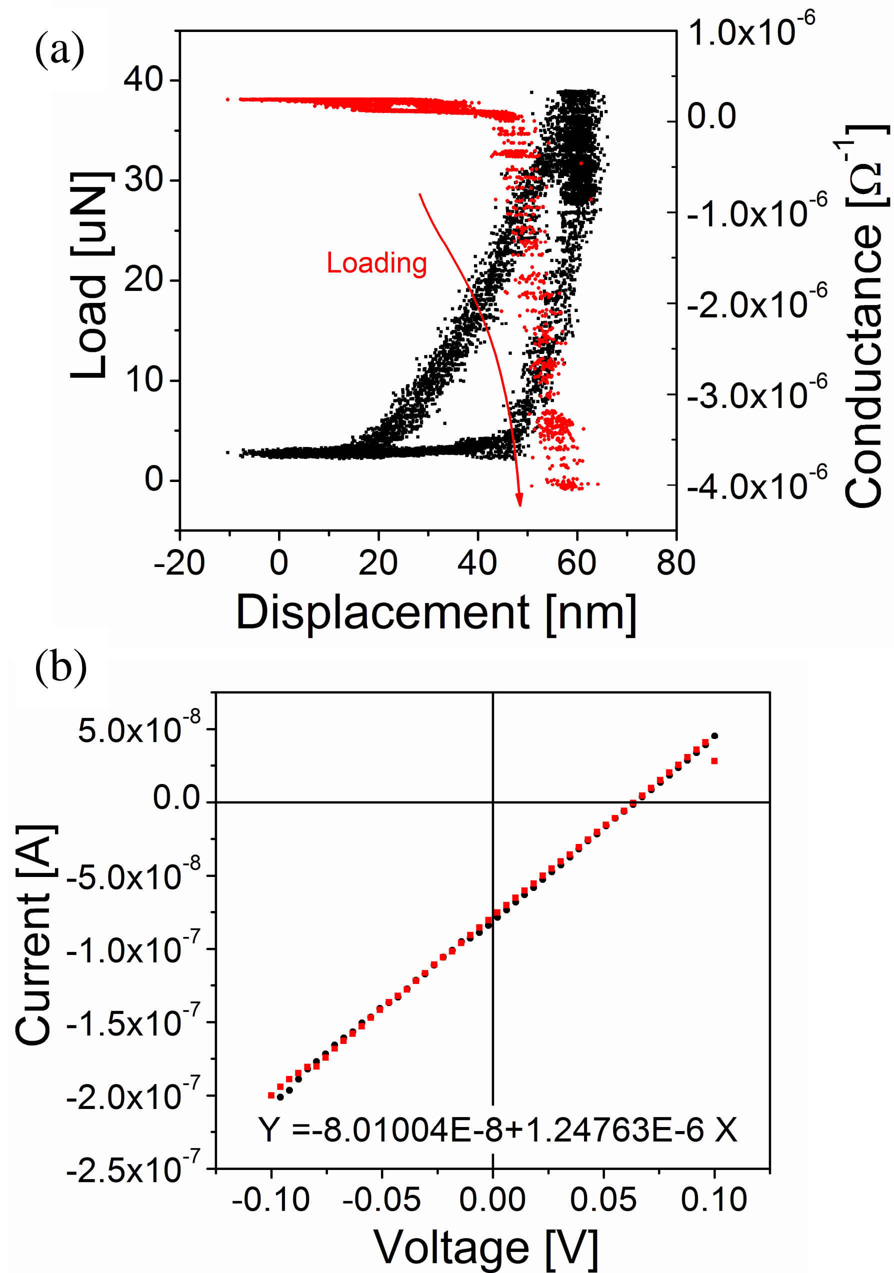

Figure 6.7.(a) Load – depth and conductance depth for a 110 nm diameter, n-doped, pillar compressed with 10mV bias. More than 20 nm of residual plasticity remains after compression, appearing primarily at the rounded tip. **(b)** The I-V sweep, performed during the hold period for (a). There is some observation of creep during the sweep, as the load decreases at constant displacement during the hold.

This technique could therefore be used to measure resistance of single pillars of various types, including conductive ceramics, and metals. Additionally, as plasticity is introduced in Si, the number of carriers due to broken bands increases, decreasing the resistance. This is in contrast to metals, where dislocations, acting as scattering sites, increase the resistance. With the previous understanding of dislocation type, structure, and density, qualitative measurements could be made regarding carrier, n, increases as,

$$\rho = \frac{m_e v_F}{ne^2 l} \quad , \qquad \text{Eq. 6.3}$$

where m_e is the mass of the electron, l is the mean free path, e is the charge of an electron, and v_F is the velocity at the Fermi level. The limitation here though is that as dislocation density increases are linked to mean free path decreases, so this cannot be used to exactly determine the carrier concentration increases in this two probe experiment. However, relationships between dislocation densities introduced during processing could be explored with respect to the expected electrical properties.

6.8. Summary

Several experiments have been proposed here to push the capabilities of the *in situ* techniques of this thesis forward, including the investigations of film delamination and fracture of oxides on metal films. Further refining the experimental technique of *in situ* TEM indentation to take full advantage of the instrument capabilities has been a major objective, and has found some success. Additionally, both dislocation velocities AND work hardening in silicon nanostructures has been investigated. Silicon, arguably the most important technological material of our time, has been shown that length scale effects have a role in this enhancement in dislocation nucleation and propagation. The experiments in this chapter are provided as a means to further explore these effects.

References

1. G. Salomonsen, N. Norman, O. Lonsjo and T. G. Finstad, Journal of the Less-Common Metals **158**, 251-265 (1990).
2. K. Tamura, Y. Kimura, H. Suzuki, O. Kido, T. Sato, T. Tanigaki, M. Kurumada, Y. Saito and C. Kaito, Jpn. J. Appl. Phys. **42** (12), 7489-7492 (2003).
3. J. S. Moodera, E. F. Gallagher, K. Robinson and J. Nowak, Applied Physics Letters **70** (22), 3050-3052 (1997).
4. J. C. Grosskreutz, J. Electrochemical Soc. **116** (1969).
5. R. W. J. Chia, C. C. Wang and J. J. K. Lee, Journal of Magnetism and Magnetic Materials **209**, 45-49 (2000).
6. S. K. Venkataraman, D. L. Kohlstedt and W. W. Gerberich, Thin Solid Films **223** (2), 269-275 (1993).
7. W. D. J. Callister, John Wiley & Sons, Inc, 56, 117-120, 620 (2003).
8. Gopal, Revankar, Deere and Company, ASM Handbooks Online (2003).
9. W. W. Gerberich, W. M. Mook, C. B. Carter and R. Ballarini, Int. J. of Fracture **148** (2) (2008).
10. G. Feng and W. D. Nix, Scripta Materiala **51** (6), 599-603 (2004).
11. R. Hill, L. E.H. and S. J. Tupper, Proc. Roy. Soc. **A188**, 273-289 (1947).
12. R. Holm, Springer-Verlag: Berlin/Heidelberg/New York, 1-55, 367-397 (1967).
13. K. L. Johnson, Cambridge University Press, 90, (1985).
14. H. E. e. Boyer, in *ASM International: Metals Park, Ohio* (1987).
15. E. L. Tobolski and A. Fee, in *ASM International; 10 edition*, edited by H. Kuhn and D. Medlin (2000).
16. W. D. Nix and H. Gao, J. Mech. Phys. Solids **46** (3), 441-425 (1998).
17. N. A. Stelmashenko, M. G. Walls, L. M. Brown and Y. V. Milman, Acta Materialia **41**, 2855-2865 (1993).
18. N. I. Tymiak, D. E. Kramer, D. F. Bahr, T. J. Wyrobek and W. W. Gerberich, Acta Materialia **49**, 1021-1034 (2001).
19. W. W. Gerberich, N. I. Tymiak, J. C. Grunlan, M. F. Horstemeyer and M. I. Baskes, J. Appl. Mech. **69**, 433-442 (2002).
20. H. Hertz, Mech. **92**, 151-171 (1881).
21. N. Schwarzer, Philosophical Magazine **86** (33-35), 5179-5197 (2006).
22. A. C. Fischer-Cripps, Springer: New York (2004).
23. D. Tabor, New York: Oxford Calrendon Press (1951).
24. W. C. Oliver and G. M. Pharr, J. Materials Research **7** (6), 1564-1583 (1992).
25. W. C. Oliver and G. M. Pharr, J. Materials Research **19** (1), 3-20 (2004).
26. I. N. Sneddon, Proc. Cambridge Philos. Soc. **44**, 492-507 (1948).
27. I. N. Sneddon, Int. J. of Eng. Sci **3**, 47 (1965).
28. N. Schwarzer, et al, (SIO® - Saxonian Institute of Surface Mechanics, www.siomec.de, Ummanz, Germany, 2011).
29. J. G. Swadener and G. M. Pharr, Philosophical Magazine A **81** (2), 447 - 466 (2001).
30. T. Chudoba, N. Schwarzer and F. Richter, surface and coatings technology **154** (2-3), 140-151 (2002).

31. N. Schwarzer, J. Schimmel and F. Richter, physica status solidi (a) **145** (2), 379-383 (1994).
32. P. C. Chou and N. Pagano, *Elasticity: Tensor, Dyadic, and Engineering Approaches*. (Dover Publications, New York, NY, 1967).
33. A. P. Boresi, O. M. Sidebottom, F. B. Seely and J. O. Smith, John Wiley & Sons, Inc: New York **2nd Edition**, 77 (1978).
34. R. W. Hertzberg, John Wiley & Sons, Inc **4th Edition**, 3-52 (1996).
35. R. C. Juvinall and K. M. Marshek, *Fundamentals of Machine Component Design*. (John Wiley and Sons, New York, NY, 2006).
36. H. Habbab, B. G. Mellor and S. Syngellakis, Acta Materialia **54** (7), 1965-1973 (2006).
37. E. S. Berkovich, Ind. Diamond Rev. **11** (127), 129-133 (1951).
38. R. B. King, Int. J. Solids Structures **23** (12), 1657-1664 (1987).
39. W. M. Mook and W. W. Gerberich, Presentation: MRS Fall Meeting (2007).
40. F. D. Murnaghan, Proc. N.A.S **30**, 244-247 (1944).
41. Y. V. Sharvin, Zh. Eksp. Teor. Fiz. **48**, 984 (1965).
42. B. Nikolic' and P. B. Allen, Phys. Rev. B **60** (6), 3963-3969 (1998).
43. G. Wexler, Proc. Phys. Soc. **89**, 927-941 (1966).
44. A. Tholen, D. Erts, H. Olin, L. Ryen and O. E., Phys. Rev. B **61** (19), 12 725-712 727 (2000).
45. A. Matthiessen and C. Vogt, Philosophical Transactions of the Royal Society of London **154**, 167-200 (1864).
46. R. Zuercher, M. Mueller, F. Sachslehner, V. Groeger and M. Zehetbauer, J. Phys. Condens. Matter **7**, 3515-3528 (1995).
47. B. R. Watts, J. Phys. F: Metal Physics **18** (1988).
48. B. Sipos, N. Barisic, R. Gaal, L. Forro, J. Karpinski and F. Rullier-Albenque, Phys. Rev. B **76**, 132504 (2007).
49. J. A. Greenwood and J. H. Tripp, Trans. ASME, Series E, J. of Applied Mechanics **34** (153), 417-420 (1967).
50. L. Kogut and K. Komvopoulos, J. Appl. Phys. **94** (5), 3153-3162 (2003).
51. M. J. Cordill, W. M. Mook, A. K. Nair, D. Farkas and W. W. Gerberich, JOM **59** (9), 59-61 (2007).
52. O. L. Warren, S. A. Downs and T. J. Wyrobek, Zeitscrift fur Metallkunde **95**, 287 (2004).
53. M. Werner, R. Job, A. Zaitzev, W. R. Fahrner, W. Seifert, C. Johnston and P. R. Chalker, Phys. Stat. Sol. **154**, 385-393 (1996).
54. Y. V. Pleskov, Y. E. Evstefeeva, M. D. Krotova, V. P. Varnin and I. G. Teremetskaya, J. of Electronanalytical Chemistry **595**, 168-174 (2006).
55. P. Gluche, M. Adamschik, A. Vescan, W. Ebert, F. Szuecs, H. J. Fecht, A. Floeter, R. Zachai and E. Kohn, Diamond and related materials **7**, 779-782 (1998).
56. S. Ruffell, J. E. Bradby, J. S. Williams and O. L. Warren, J. Materials Research **22** (3), 578-586 (2006).
57. R. Nowak, D. Chrobak, S. Nagao, D. Vodnick, M. Berg, A. Tukiainen and M. Pessa, Nature Nanotechnology **4**, 287-291 (2009).

58. S. P. Sharma and J. H. I. Thomas, Journal of Applied Physics **47** (5), 1808-1811 (1975).
59. L. Fang, C. L. Muhlstein, J. G. Collins, A. L. Romasco and L. H. Friedman, Journal of Materials Research **23** (9), 2480-2485 (2008).
60. B. Bhushan, Palacio, M., Kinzig, B., Journal of Colloid and Interface Science **317**, 275-287 (2008).
61. J. B. Pethica and D. Tabor, Surface Science **89**, 182-190 (1979).
62. D. I. Kim, N. Pradeep, F. W. DelRio and R. F. Cook, Applied Physics Letters **93**, 203102 (2008).
63. J. C. Maxwell, Dover Publications: 3rd Edition, English (1904).
64. W. W. Gerberich, Nelson, J.C., Lilleodden, E.T., Anderson, P., Wyrobek, J.T., Acta Materialia **44** (9), 3585-3598 (1995).
65. A. B. Mann and J. B. Pethica, Applied Physics Letters **69** (7), 907-910 (1996).
66. D. Kramer, H. Huang, M. Kriese, J. Robach, J. Nelson, A. Wright, D. Bahr and W. W. Gerberich, Acta Materialia **47** (1), 333-343 (1999).
67. D. F. Bahr, D. E. Kramer and W. W. Gerberich, Acta Materialia **46** (10), 3605-3617 (1997).
68. D. E. Kramer, K. B. Yoder and W. W. Gerberich, Philosophical Magazine A **81** (8), 2033-2058 (2000).
69. J. B. Pethica and W. C. Oliver, Phys. Scripta **T19**, 61-66 (1987).
70. W. A. Soer, K. E. Aifantis and J. T. M. De Hosson, Acta Materialia **53**, 4665-4676 (2005).
71. C. L. Muhlstein, (Minneapolis, 2010).
72. ISO/DIS 14577-1, 2, 3, and 4 (ISO group TC 164/SC 3/WG 1 and ASTM E28.06.11) (2002).
73. J. A. Greenwood and J. B. P. Williamson, Proceedings, Royal Society **A295** (300), 411-413 (1966).
74. A. J. W. Moore, Proc. Roy. Soc., Lond. **195** (231), 36,216 (1948).
75. G. Liu, Q. Wang and C. Lin, Tribology Transactions **42** (3), 581-591 (1999).
76. L. Kogut and I. Etsion, Tribology Transactions **46** (3), 383-390 (2003).
77. J. Simmons, Journal of Applied Physics **34**, 1793 (1963).
78. W. F. Brinkman, R. C. Dynes and J. M. Rowell, Journal of Applied Physics **41** (5), 1915-1921 (1970).
79. J. J. Åkerman, R. Escudero, C. Leighton, S. Kim, D. A. Rabson, R. W. Dave, J. M. Slaughter and I. K. Schuller, Journal of Magnetism and Magnetic Materials **240**, 86-91 (2002).
80. H. Jeffreys, Proceedings of the London Mathematical Society **23**, 428-436 (1923).
81. G. Wentzel, Zeitschrift der Physik **38**, 518-529 (1926).
82. H. A. Kramers, Zeitschrift der Physik **39**, 828-840 (1926).
83. L. Brillouin, Comptes Rendus de l'Academie des Sciences **183**, 24-26 (1926).
84. D.-I. Kim, N. Pradeep, F. W. DelRio and R. F. Cook, Applied Physics Letters **93** (20), 203102-203103 (2008).
85. J. Parker, L. Wang, K. A. Steiner, P. A. Crowell and C. L. Leighton, Phys. Rev. Letters **97**, 227206 (2006).

86. M. R. Fitzsimmons and C. F. Majkrzak, *Modern Techniques for Characterizing*. (Kluwer, Boston, 2005).
87. B. V. Crist, XPS International, Inc. (1999).
88. J. E. Castle, H. Chapman-Kpodo, A. Proctor and A. M. Salvi, Journal of Electron Spectroscopy and Related Phenomena **106**, 65-80 (2000).
89. M. Aronniemi, J. Sainio and J. Lahtinen, Surface Science **578**, 108-123 (2005).
90. C. S. Fadley, Journal of Electron Spectroscopy and Related Phenomena **5** (1), 725-754 (1974).
91. J. F. Watts, Oxford University Press, 7 (1990).
92. M. P. Seah and W. A. Dench, Surface and Interface Analysis **1** (1), 2-10 (1979).
93. R. Cheng, C. N. Borca, B. Xu, L. Yuan, B. Doudin, S. H. Liou and P. A. Dowben, Applied Physics Letters **81** (11), 2109-2111 (2002).
94. J. Dai, J. Tang, H. Xu, L. Spinu, W. Wang, K. Wang, A. Kumbhar, M. Li and U. Diebold, Applied Physics Letters **77** (18), 2840 (2000).
95. I. Ikemoto, I. Kikujiro, S. Kinoshita, H. Kuroda, M. A. Alario Franco and J. M. Thomas, Journal of Solid State Chemistry **17** (4), 425-430 (1976).
96. J. S. Villarrubia, Journal of Research of the National Institute of Standards and Technology **102**, 425-454 (1997).
97. H. Gao, C.-H. Chiu and J. Lee, Internation Journal of Solids and Structures **29** (20), 2471-2492 (1992).
98. J. H. Kim, C. S. Korach and A. Gouldstone, Journal of Materials Research **23** (11), 2935-2943 (2008).
99. V. Provenzano, R. Valiev, D. G. Rickerby and G. Valdre, NanoStructured Materials **12**, 1103-1108 (1999).
100. S. A. Firstov, T. G. Rogul and S. N. Dub, in *Innovative Superhard Materials and Sustainable Coatings for Advanced Manufacturing*, edited by J. Lee, N. Novikov and V. Turkevich (Springer Netherlands, 2005), Vol. 200, pp. 225-232.
101. R. Saha and W. D. Nix, Acta Materialia **50** (1), 23-38 (2002).
102. T. Ohmura, S. Matsuoka, K. Tanaka and T. Yoshida, Thin Solid Films **385** (1-2), 198-204 (2001).
103. D. E. Kramer, A. A. Volinsky, N. R. Moody and W. W. Gerberich, J. Materials Research **16** (11) (2001).
104. T. Y. Tsui, C. A. Ross and G. M. Pharr, Journal of Materials Research **18** (6), 1383-1391 (2003).
105. M. S. Bobji, S. K. Biswas and J. B. Pethica, Applied Physics Letters **71** (8), 1059-1061 (1997).
106. W. W. Gerberich, N. I. Tymiak, J. C. Grunlan, M. F. Horstemeyer and M. I. Baskes, Journal of Applied Mechanics **69** (4), 433-442 (2002).
107. D. A. Spence, Journal of Elasticity **5** (1975).
108. M. Iwasa and T. Ueno, Zairyo **30** (337) (1981).
109. N. B. Pilling and R. E. Bedworth, J. Institute of Metals **29** (1923).
110. H. Bernstein, Metallurgical and Materials Transactions A **22** (1), 975-986 (1991).
111. H. Huang and et al., Journal of Micromechanics and Microengineering **15** (3), 608 (2005).

112. S. K. Venkataraman, D. L. Kohlstedt and W. W. Gerberich, J. Materials Research **8** (4), 685-688 (1993).
113. L. D. Marks, O. L. Warren, A. M. Minor and A. P. Merkel, MRS Bulletin **33** (2008).
114. N. Gane and F. P. Bowden, J. Appl. Phys. **39** (3), 1432 (1968).
115. N. Gane, Proc. Roy. Soc. Lond. A **317**, 367-391 (1970).
116. M. I. Lutwyche and Y. Wada, Applied Physics Letters **66** (21), 2807-2809 (1995).
117. Y. Naitoh, K. Takayanagi and M. Tomitori, Surface Science **357-358**, 208-212 (1996).
118. M. A. Wall and U. Dahmen, Microsc Microanal **3** (1997).
119. M. A. Wall and U. Dahmen, Microsc Res Techn **42** (1998).
120. E. A. Stach, T. Freeman, A. M. Minor, D. K. Owen, J. Cumings, M. A. Wall, T. Chraska, R. Hull, J. W. Morris, A. Zettl and U. Dahmen, Microsc. Microanal. **7**, 507-517 (2001).
121. A. M. Minor, J. J. W. Morris and E. A. Stach, Applied Physics Letters **79** (11), 1625-1627 (2001).
122. J. L. Martin and L. P. Kubin, Ultramicroscopy **3** (2), 215-226 (1978).
123. D. B. Williams and C. B. Carter, *Transmission Electron Microscopy: A Textbook for Materials Science*, 1 ed. (Springer, New York, NY, 1996).
124. R. F. Egerton, P. Li and M. Malac, Micron **35**, 399-409 (2004).
125. S. J. Klepeis, J. P. Benedict and R. M. Anderson, MRs Proceedings **115** (1987).
126. D. D. Stauffer, O. Ugurlu, R. Major and W. W. Gerberich, (University of Minnesota, Minneapolis, 2011).
127. L. A. Giannuzzi and F. A. Stevie, Micron **30**, 197-204 (1999).
128. M. Sugiyama and G. Sigesato, J. Electron Microscopy **53** (5), 527-536 (2004).
129. J. Ayache, L. Beaunier, J. Boumendil, G. Erhet and D. Laub, *Sample Preparation Handbook for Transmission Electron Microscopy*. (Springer, New York, NY, 2010).
130. Z. W. Shan, R. K. Mishra, S. A. S. A., O. L. Warren and A. M. Minor, Nat Mater **7** (2), 115-119 (2008).
131. M. D. Uchic, D. M. Dimiduk, J. N. Florando and W. D. Nix, Science **305** (5686), 986-989 (2004).
132. J. R. Greer and W. D. Nix, Phys. Rev. B **73**, 245410 (2006).
133. J. R. Greer and W. D. Nix, Applied Physics A: Materials Science & Processing **80** (8), 1625-1629 (2005).
134. F. Östlund, K. Rzepiejewska-Malyska, K. Leifer, L. M. Hale, Y. Tang, R. Ballarini, W. W. Gerberich and J. Michler, Advanced Functional Materials **19** (15), 2439-2444 (2009).
135. D. Kiener, C. Motz, M. Rester, M. Jenko and G. Dehm, Materials Science and Engineering: A **459** (1-2), 262-272 (2007).
136. H. Bei, S. Shim, M. K. Miller, G. M. Pharr and E. P. George, Applied Physics Letters **91** (11), 111915-111913 (2007).
137. K. R. Williams and R. S. Muller, Microelectromechanical Systems, Journal of **5** (4), 256-269 (1996).

138. A. M. Minor, J. W. Morris and E. A. Stach, Applied Physics Letters **79** (11), 1625-1627 (2001).
139. W. A. Soer, J. T. M. D. Hosson, A. M. Minor, J. W. Morris Jr and E. A. Stach, Acta Materialia **52** (20), 5783-5790 (2004).
140. Y. Sun, J. Ye, A. M. Minor and T. J. Balk, Microscopy Research and Technique **72** (3), 232-241 (2009).
141. A. M. Minor, E. T. Lilleodden, M. Jin, E. A. Stach, D. C. Chrzan and J. W. Morris, Philosophical Magazine **85** (2), 323 - 330 (2005).
142. Y. Choi, K. J. Van Vliet, J. Li and S. Suresh, Journal of Applied Physics **94** (9), 6050-6058 (2003).
143. D. E. Kramer, A. A. Volinsky, N. R. Moody and W. W. Gerberich, J. Materials Research **16** (11), 3150-3157 (2001).
144. G. Huajian, C. Cheng-Hsin and L. Jin, International Journal of Solids and Structures **29** (20), 2471-2492 (1992).
145. J. Deneen, W. Mook, A. Minor, W. Gerberich and C. Barry Carter, Journal of Materials Science **41** (14), 4477-4483 (2006).
146. J. Hay, P. Agee and E. Herbert, Experimental Techniques **34** (3), 86-94 (2010).
147. E. A. Stach, (2008).
148. M. De Graff, *Introduction to Conventional Transmission Electron Microscopy*. (Cambridge University Press, Cambridge, 2003).
149. M. Jin, A. M. Minor, E. A. Stach and J. J. W. Morris, Acta Materialia **52** (18), 5381-5387 (2004).
150. A. K. Head, P. Humble, L. M. Clarebrough, A. J. Morton and C. T. Forwood, *Computed electron micrographs and defect identification*. (North-Holland Publishing, Amsterdam, 1973).
151. X. D. Han, K. Zheng, Y. F. Zhang, X. N. Zhang, Z. Zhang and Z. L. Wang, Advanced Materials **19** (16), 2112-2118 (2007).
152. A. M. Minor, A. S. A. Syed, Z. S. Shan, E. A. Stach, E. Cyrankowski, T. Wyrobek and O. L. Warren, Nature Materials **5** (9), 697-702 (2006).
153. Y. Cui and C. M. Lieber, Science **291** (5505), 851-853 (2001).
154. P. Omling, E. R. Weber, L. Montelius, H. Alexander and J. Michel, Physical Review B **32** (10), 6571 (1985).
155. R. H. Glaenzer and A. G. Jordan, Solid-State Electronics **12** (4), 247-258 (1969).
156. A. G. Zakharov, V. G. Dudko, G. M. Nabokov and D. A. Sechenov, Russian Physics Journal **31** (1), 70-72 (1988).
157. D. Hull, Bacon, D.J., Butterworth Heineman **3rd Edition**, 248 (1984).
158. M. Imai and K. Sumino, Philos. Mag. A. **47**, 599-621 (1983).
159. H. Conrad and G. Schoeck, Acta Metallurgica **8** (11), 791-796 (1960).
160. H. Alexander and P. Haasen, Solid State Physics **22**, 27 (1968).
161. I. H. Lin and R. Thomson, Acta Metallurgica **34** (2), 187-206 (1986).
162. H. Huang and W. W. Gerberich, Acta Metallurgica et Materialia **40** (11), 2873-2881 (1992).
163. R. M. McMeeking and D. M. Parks, in *ASTM STP 668* (ASTM, Philadelphia, PA, 1979), pp. 175-194.
164. J. Samuels and S. G. Roberts, Proc. Roy. Soc. Lond. A **421**, 1-23 (1989).

165. R. Hull, in *Datareview Series* (INSPEC, London, 1999).
166. L. Hale, (2011).
167. C.-Z. Wang, J. Li, K.-M. Ho and S. Yip, Applied Physics Letters **89** (5), 051910-051913 (2006).
168. H. Siethoff and P. Haasen, in *Lattice defects in semiconductors*, edited by R. R. Hasiguti (University of Tokyo Press, The Pennsylvania University Press, Tokyo, 1968).
169. W. Shockley, Physical Review **91** (1953).
170. J. Godet, P. Hirel, S. Brochard and L. Pizzagalli, physica status solidi (a) **206** (8), 1885-1891 (2009).
171. J. Rabier and J. L. Demenet, physica status solidi (b) **222** (1), 63-74 (2000).
172. W. Cai, V. V. Bulatov, J. F. Justo, A. S. Argon and S. Yip, Physical Review Letters **84** (15) (2000).
173. S. Prussin, Journal of Applied Physics **43** (6), 2850-2856 (1972).
174. R. Hull, E. A. Stach, R. Tromp, F. Ross and M. Reuter, physica status solidi (a) **171** (1), 133-146 (1999).
175. R. Hull, J. C. Bean, D. J. Eaglesham, J. M. Bonar and C. Buescher, Thin Solid Films **183** (1-2), 117-132 (1989).
176. J. Rabier, M. F. Denanot, J. L. Demenet and P. Cordier, Materials Science and Engineering A **387-389**, 124-128 (2004).
177. S. Izumi, H. Ohta, C. Takahashi, T. Suzuki and H. Saka, Philosophical Magazine Letters **90** (10), 707 - 714 (2010).
178. W. W. Gerberich, W. M. Mook, C. R. Perrey, C. B. Carter, M. I. Baskes, R. Mukherjee, A. Gidwani, J. Heberlein, P. H. McMurry and S. L. Girshick, Journal of the Mechanics and Physics of Solids **51** (6), 979-992 (2003).
179. W. M. Mook, J. D. Nowak, C. R. Perrey, C. B. Carter, R. Mukherjee, S. L. Girshick, P. H. McMurry and W. W. Gerberich, Physical Review B **75** (21), 214112 (2007).
180. W. W. Gerberich, J. Michler, W. M. Mook, R. Ghisleni, F. Ostlund, D. D. Stauffer and R. Ballarini, Journal of Materials Research **24** (3), 898-906 (2009).
181. X. Han, K. Zheng, Y. Zhang, X. Zhang, Z. Zhang and Z. Wang, Advanced Materials **19** (16), 2112-2118 (2007).
182. T. Kizuka, Y. Takatani, K. Asaka and R. Yoshizaki, Physical Review B **72** (3), 035333 (2005).
183. B. Moser, K. Wasmer, L. Barbieri and J. Michler, J. Materials Research **22** (4) (2007).
184. F. Östlund, K. Rzepiejewska-Malyska, K. Leifer, L. M. Hale, Y. Tang, R. Ballarini, W. W. Gerberich and J. Michler, Advanced Functional Materials **19** (15), n/a-n/a (2009).
185. C. St. John, Philos Mag **32** (6), 1193-1212 (1975).
186. H. R. Kolar, J. C. H. Spence and H. Alexander, Physical Review Letters **77** (19), 4031 (1996).
187. R. S. Wagner and W. C. Ellis, Applied Physics Letters **4** (5), 89-90 (1964).

188. S. H. Oh, K. v. Benthem, S. I. Molina, A. Y. Borisevich, W. Luo, P. Werner, N. D. Zakharov, D. Kumar, S. T. Pantelides and S. J. Pennycook, Nano Letters **8** (4), 1016-1019 (2008).
189. J. E. Allen, E. R. Hemesath, D. E. Perea, J. L. Lensch-Falk, LiZ.Y, F. Yin, M. H. Gass, P. Wang, A. L. Bleloch, R. E. Palmer and L. J. Lauhon, Nat Nano **3** (3), 168-173 (2008).
190. H. Zhang, B. E. Schuster, Q. Wei and K. T. Ramesh, Scripta Materialia **54** (2), 181-186 (2006).
191. W. D. Nix, J. R. Greer, G. Feng and E. T. Lilleodden, Thin Solid Films **515** (6), 3152-3157 (2007).
192. J. D. Eshelby, Philosophical Transactions of the Royal Society of London. Series A, Mathematical and Physical Sciences **244** (877), 87-112 (1951).
193. E. Dieter, *Mechanical Metallurgy*. (McGraw Hill, New York, N.Y., 1976).
194. S. Mendelson, J. Appl. Phys. **43** (5) (1972).
195. A. Nadai, *Theory of Flow and Fracture of Solids, 2nd Ed.* (McGraw Hill Book Company, New York, 1950).
196. G. T. Hahn, Acta Metallurgica **10** (8), 727-738 (1962).
197. C. A. Volkert and E. T. Lilleodden, Philosophical Magazine **86** (33), 5567 - 5579 (2006).
198. P. Hirsch, A. Howie, R. Nicholson, D. W. Pashley and M. J. Whelan, *Electron Microscopy of Thin Crystals*. (Buttersworth, London, UK, 1965).
199. J. W. Edington, *Practical Electron Microscopy in Materials Science*. (Van Nostrand, New York, NY, 1976).
200. E. A. Stach, (2010).
201. A. Howie and M. J. Whelan, Proceedings of the Royal Society of London. Series A. Mathematical and Physical Sciences **267** (1329), 206-230 (1962).
202. E. A. Stach, (2008).
203. J. P. Hirth and J. Lothe, *Theory of Dislocations*. (John Wiley and Sons, New York, NY, 1982).
204. D. B. Williams, Carter, C.B., Springer Science & Business (1996).
205. E. A. Stach, University of Virginia, 1998.
206. J. J. Gilman, W. G. Johnston and G. W. Sears, Journal of Applied Physics **29** (5), 747-754 (1958).
207. M. Wen and A. H. W. Ngan, Acta Materialia **48** (17), 4255-4265 (2000).
208. G. Vanderschaeve and et al., Journal of Physics: Condensed Matter **12** (49), 10093 (2000).
209. S. Brinckmann, J.-Y. Kim and J. R. Greer, Phys. Rev. Letters **100** (15) (2008).
210. H. Bei, S. Shim, G. M. Pharr and E. P. George, Acta Materialia **56** (17), 4762-4770 (2008).
211. H. Alexander, Zeitschrift fur Metalkunde **52** (1961).
212. H. Alexander and P. Haasen, Acta Metallurgica **9** (1961).
213. E. A. Stach and R. Hull, Applied Physics Letters **79** (3), 335-337 (2001).
214. R. Hull, J. C. Bean, L. J. Peticolas, B. E. Weir, K. Prabhakaran and T. Ogino, Applied Physics Letters **65** (3), 327-329 (1994).

215. A. R. Beaber, L. Qi, J. Hafiz, J. Heberlein, W. W. Gerberich and S. Girshick, Surface and Coatings Technology **207** (2007).
216. W. M. Mook, Nowak, J.D., Perrey, C.R., Carter, C.B., Mukherjee, R., Girschick, S.L., McMurray, P., Gerberich, W.W., Phys. Rev. B **75**, 214112 (2007).
217. J. D. Nowak, A. R. Beaber, O. Ugurlu, S. L. Girshick and W. W. Gerberich, Scripta Materialia **62** (11), 819-822 (2010).
218. R. Hill, Proc. Roy. Soc. London **A65**, 349-354 (1952).
219. M. J. Cordill, Moody, N.R., Gerberich, W.W., Int. J. of Plasticity (*in press, 2008*).
220. J. D. Nowak, W. M. Mook, A. M. Minor, W. W. Gerberich and C. B. Carter, Philosophical Magazine **87** (1), 29 - 37 (2007).
221. S. Korte and W. J. Clegg, Scripta Materialia **60** (9), 807-810 (2009).
222. S. Korte and W. J. Clegg, Philosophical Magazine **91** (7), 1150 - 1162 (2011).
223. N. Gane and F. P. Bowden, Journal of Applied Physics **39** (3), 1432-1435 (1968).
224. M. J. Cordill, N. R. Moody and W. W. Gerberich, International Journal of Plasticity **25** (2), 281-301 (2009).
225. E. R. Weppelmann, J. S. Field and M. V. Swain, Journal of Materials Science **30** (9), 2455-2462 (1995).
226. A. Kailer, Y. G. Gogotsi and K. G. Nickel, Journal of Applied Physics **81** (7), 3057-3063 (1997).
227. A. R. Beaber, (2011).
228. V. Domnich, Y. Aratyn, W. M. Kriven and Y. G. Gogotsi, Rev. Adv. Mater. Sci **17**, 33-41 (2008).
229. F. D. Murnaghan, P Natl Acad Sci USA **30** (9), 244-247 (1944).
230. M. Nonnenmacher, M. P. O'Boyle and H. K. Wickramasinghe, Applied Physics Letters **58** (25), 2921-2923 (1991).
231. U. Zerweck, C. Loppacher, T. Otto, Grafstr, ouml, S. m and L. M. Eng, Physical Review B **71** (12), 125424 (2005).
232. M. Cordill, JOM Journal of the Minerals, Metals and Materials Society **62** (6), 9-14 (2010).
233. S. Khongtong and G. S. Ferguson, J Am Chem Soc **124** (25), 7254-7255 (2002).
234. N. R. Moody, E. D. Reedy, E. Corona, D. P. Adams, X. Zhou, J. A. Emerson, T. D. Nguyen, M. S. Kennedy, M. J. Cordill, L. Hale, J. Yeager and D. F. Bahr, 2009.
235. M. D. Kriese, W. W. Gerberich and N. R. Moody, J. Materials Research **14**, 3007-3018 (1999).
236. D. B. Marshall and A. G. Evans, Journal of Applied Physics **56** (10), 2632-2638 (1984).
237. M. J. Cordill, D. F. Bahr, N. R. Moody and W. W. Gerberich, Device and Materials Reliability, IEEE Transactions on **4** (2), 163-168 (2004).
238. J. Michler, in *Materials Research Society Fall 2010* (2010).